Dissertation

Ultrafast Optical Phenomena in Magneto-Plasmonic Crystals and Magnetically Ordered Materials

Martin Pohl

presented to the Faculty of Physics of the
Technische Universität Dortmund, Germany,
in partial fulfillment of the requirements
for the degree of

Doktor rer. nat.

technische universität
dortmund

Dortmund, February 2014

Contents

4.1 Ultrafast Electron Momentum Relaxation and Dephasing

5.1 Ultrafast Optically Induced Precession of the Magnetization

Motivation

Plasmonic excitations have already been used centuries ago for the staining of glass. Powders of metallic oxides or pure metals were added to the molten glass during the manufacturing. The metallic nanometer sized inclusions inherited so-called plasmon polaritons at their surface, to which incident light could couple at characteristic photon energies depending on the particle sizes of the metals. Unknowingly exploiting this selective absorption, artists produced colorful church windows and glass objects, some of them dating back to Roman times.

Surface plasmon polaritons (SPPs) are collective oscillations of a conductor's surface electrons at the interface to a dielectric. Although metals are of no special interest for modern optics or nanophotonics, the interaction of SPPs with the electromagnetic field of light at a metal's surface can reveal unique and fascinating phenomena, which make these quasi-particles important tools in a variety of research and application fields. Unlike for nano-particles, the coupling of light to SPPs in bulk materials requires special techniques using attenuated total reflection (ATR), near-field spectroscopy or sub-wavelength periodic structures. Hence, a high scientific interest in the field did not occur until the beginning of the 21th century when increasingly powerful tools for electromagnetic simulations triggered the improvement of expertise and techniques in the fabrication and characterization of nanoscale structures.

One of the most intriguing properties of SPPs is their ability to concentrate electromagnetic fields to dimensions deeply below the diffraction limit imposed by Gaussian optics.[1] As a consequence, the electric field density of light coupled to an SPP at the metal's surface can be strongly enhanced, thereby increasing linear and non-linear light-matter interactions. For example, second harmonic generation (SHG) in bulk noble metals is usually symmetry forbidden due to their centro-symmetric crystal structure. Nahata et al. [2003] exploited the fact that this symmetry is broken at the surface and used a sub-wavelength periodic structure at the surface of a 300 nm thin silver film to optically excite SPP modes. The surface waves could propagate to the other side of the film through a hole in the center of the structure thereby creating an optical emission at the second harmonic of the incident light due to their strongly localized electric fields. That way, the transmitted SHG intensity could be enhanced by four orders of magnitude with respect to the unstructured aperture geometry. By means of this SPP field enhancement effect, already high harmonics up to the 17th order could be generated from bow tie-shaped gold plasmon antennas [Kim et al., 2008].[2] Similarly, in so-called surface enhanced Raman scattering (SERS) experiments, the scattering cross section from molecules adsorbed onto metal nanoparticles has been shown to increase by 14 orders of magnitude due to SPP excitations, so that chemical structures of materials can

---

[1] The Gaussian diffraction limit restricts light to be focused by conventional optics below spot sizes of $\lambda/2$, where λ is the wavelength of light.

[2] However, due to apparent inconsistencies and a lack of reproducibility, the role of plasmonics in the microscopic origin of HHG in this work has been questioned lately [Raschke, 2013].

be resolved even at the single molecule level [Kneipp, 2007]. Furthermore, SPPs are used in modern solar cells in order to compensate one of the major drawbacks of thin-film designs, namely the low photon absorption probability. Therefore, metal nanoparticles or sub-wavelength gratings are implemented into the films or at their backside, respectively, to trap the electric field of light in the film plane via SPP excitations [Atwater and Polman, 2010]. In a bulk design based on silicon microwires embedded into a transparent polymer matrix, aluminum nanoparticles are used to efficiently increase the absorption probability, while only consuming 1 % of the active material with respect to conventional silicon based solar cells [Zhu and Cui, 2010].

Another aspect about plasmonic nanostructures is their ability to alter the density of states and spontaneous emission rate of nearby emitters of radiation via a change in the electromagnetic environment (Purcell effect). This property has been exploited especially for plasmon-enhanced light emitting diodes (LED) by Okamoto et al. [2004], who placed a silver metal film on top of an InGaN/GaN quantum well (QW) structure, which increased the integrated photoluminescence (PL) emitted by this QW by a factor of 17 with respect to the uncoated emitter.

The above examples illustrate the usefulness and corresponding high interest in surface plasmon polaritons. Plasmonic confinement of optical energy to nanometer dimensions together with terrahertz optical control seems to be a promising combination for bypassing fundamental limits in current silicon-based microchip technology. The need for faster circuit speed and higher packing density has led to an aggressive downscaling of the metal electrical interconnects. The latter serve as the transport routes of integrated circuits (ICs), whose characteristic node sizes currently amount to 22 nm [Ingerly et al., 2012]. The downscaling leads to increased current densities and simultaneously a lack of heat transport capability and reduced distance between adjacent lines, which increases the interconnects' resistance R and capacitance C, respectively. This hampers the charge/discharge delay time $\tau \propto RC$, which threatens to annihilate the advantages of scaling with respect to device speed in the near future [Chen et al., 2005].

All-optical circuits based on dielectric components could in principle overcome these problems but cannot be readily scaled due to the fundamental optical diffraction limit. Plasmonic components, on the other hand, do not suffer this dimension mismatch and could be easily implemented on electronic microchips or act as a bridge between low-loss dielectrics and ultra-compact electronics. Even all-optical plasmonic chip designs are imaginable, although problems with mode confinement have been identified while downscaling plasmonic waveguides to sub-wavelength dimensions, which quenches the realistic propagation length in metal-insulator-metal (MIM) waveguides to around 10 μm [Zia et al., 2006]. Some of the required elements for these all-optical plasmonic circuits have already been demonstrated, e.g., ultra-compact, low-power, plasmon enhanced detectors with picosecond response times [Ishi et al., 2005] and even sub-wavelength on-chip laser sources [Hill et al., 2009; Noginov et al., 2009; Oulton et al., 2009]. Also optical modulators have been realized, e.g., by Fluegel et al. [2007]; MacDonald et al. [2009]; Temnov et al. [2010], which will be discussed in more detail in chapter 3. The main challenge in optical modulators, however, is to combine high modulation speed with a design that allows for on-chip applications, which, to the best of our knowledge, has not been realized up to now. Possible solutions to this problem will be addressed in chapter 3 of this thesis.

Apart from plasmonic structures, there is a multitude of materials capable of contributing to technological progress in modern data processing. Especially with respect to device speed, the material class of Mott insulators has evoked significant interest in the community lately. Here, the insulating character cannot be understood in the semiclassical picture, where the distinction between metals, insulators and semiconductors is made with respect to the filling of their highest occupied electronic band. While the latter is completely filled for insulators, it is only partially filled for metals, which allows for a movement of the electrons through the crystal via charge fluctuations and therefore electronic conduction. However, this model completely neglects interactions within the electron system. In fact, there are many transition-metal oxides with a partially filled d-band, such as NiO or La_2CuO_4, which fulfill the above requirements for metals, yet they are rather good insulators. The electron motion in these materials is strongly suppressed by on-site Coulomb forces [Imada et al., 1998; Sachdev, 2003]. Substances exhibiting this type of insulating behavior are called Mott insulators.

In La_2CuO_4 for example, the highest energy band is formed by Cu $3d$ orbitals. This band, having two spin states, is only half filled since there is only one of two possible electrons per unit cell available. Here, in contrast to the delocalized conduction electrons in a conducting metal, the electrons are localized at distinct lattice sites within the ion lattice in order to minimize the Coulomb repulsion. An exchange, i.e., a motion of electrons requires an intermediate state, in which one electron temporarily moves to a site already occupied by a second electron. In this intermediate state, the unit cell holds two of two possible electrons at the same lattice site, which is only allowed for opposite spin states due to the Pauli principle. Even with antiferromagnetic spin alignment, an exchange would require a high amount of energy input due to the Coulomb repulsion, which is highly unlikely. Consequently, despite its partially filled conduction band, La_2CuO_4 is an insulator.

While in their insulating phase, Mott insulators exhibit unusual optical properties since their spin, charge and orbital degrees of freedom are strongly correlated due to the unique interaction processes of the electron system [Imada et al., 1998]. Common interest in Mott insulators is further fueled by the manifold of physical phenomena that have been demonstrated in these materials, such as high critical temperature superconductivity in cuprates, colossal magnetoresistance in manganites and simultaneous coexistence of several order parameters in multiferroics [Eerenstein et al., 2006; Fiebig, 2005].

While there are many theoretical and experimental studies of the electronic structure, electron and hole transport phenomena, magnetic ordering and optical properties of Mott insulating transition-metal oxides (see, e.g., Imada et al. [1998]; Kastner et al. [1998]; Salamon and Jaime [2001]), it remains a challenging task to describe and understand the physics behind the interaction of these strongly correlated systems with ultrashort optical pulses. Theoretical predictions for the ultrafast light-matter interaction with Mott insulators include a strong enhancement of non-linear optical effects via the nonlinear optical susceptibility [Zhang, 2001] or ultrafast electron dynamics on the order of 10-100 fs and less [Gómez-Abal et al., 2004; Takahashi et al., 2004]. The latter prediction makes Mott insulators an interesting material class for ultrafast all-optical applications.[3] Especially, their usefulness as femtosecond optical switches and modulators will be the subject of chapter 4.

---

[3] In this work, the term “ultrafast” refers to time spans in the pico- or femtosecond regime. Optically induced phenomena occurring on these timescales are potentially interesting for all-optical device applications since their operating speed could reach at least terrahertz frequencies and so surpass conventional electronics.

The physics of ultrafast light-matter interactions not only has the prospect of improving today's data processing and on-chip technologies but also becomes increasingly interesting for modern data storage. With the exception of new technologies based on semiconductor materials, such as “Flash” memories, modern hard disk drives (HDD) still rely to a large amount on magnetic storage, i.e., the orientation of magnetic domains inside a ferromagnetic recording medium. These domains represent the basic unit of information and their orientation is switched by magnetic field pulses, which are created by electric currents [Chappert et al., 2007]. However, reducing the domain sizes in order to increase the storage density imposes problems with respect to thermal stability of the data. In compensation, higher anisotropy constants of the magnetic materials are required, which increase the necessary power of the writing field. Techniques, such as heat assisted magnetic recording (HAMR), promise possible solutions by local heating and subsequent cooling of the domains before and after the magnetic switching, respectively, but are intrinsically slow due to the thermal processes involved. In this respect, there have been strong efforts in the past to find ways to create magnetic field pulses and control the magnetization non-thermally, e.g., by optical means. Here, femtosecond pulsed lasers provide a powerful tool to excite magnetic materials on timescales much faster than the fundamental quantities, such as the spin-lattice relaxation time and the spin precession period.

The interest in this field of research intensified when Beaurepaire et al. [1996] reported on the sub-picosecond demagnetization of nickel by femtosecond laser pulses and thereby demonstrated the possibility of ultrafast optical manipulation of magnetization. However, the demagnetization was attributed to a considerable amount of absorption connected with a rapid increase of the electron temperature and the subsequent destruction of the magnetization. In a similar experiment, the increased electron temperature resulted in a change of the material's anisotropy field, which induced transient changes to the effective magnetic field. The magnetization then started to precess about the new equilibrium direction as was examined, e.g., by Ju et al. [2000]; van Kampen et al. [2002]. The drawback in these thermal approaches is the low repetition frequency due to the cooling time of the system, which imposes a limit for the applicability in magnetic devices. Genuine non-thermal possibilities to optically control the magnetization will be discussed in chapter 5 for magnetic iron garnets.

In this thesis, ultrafast light-matter interactions of femtosecond laser pulses with magneto-plasmonic crystals and magnetically ordered systems are examined. The aim is to gain fundamental knowledge for the optical control of the material's magneto-optical properties for all-optical applications. Here, it is differentiated between the optical control of surface plasmon polaritons and optical control over the material's magnetic order. Finally, these two branches are combined with the aim to enhance magneto-optical effects in the ultrafast regime. The structure of this work is as follows: Chapter 1 starts by reviewing the theoretical background for the subsequent chapters and by providing the mathematical derivations and equations, which are of importance in the ensuing discussions.

Chapter 2 continues with a description of the experimental methods applied. The most important of these is the femtosecond time-resolved pump-probe technique. In this technique, an intense “pump” beam induces a perturbation in a material system, which changes the optical properties due to the light-matter interaction. This in turn indirectly influences the properties, such as intensity and/or polarization, of a second "probe" beam, which scans the sample response in time via a variable time delay with respect to the pump beam. Hence, effectively, light is controlled by light. The laser pulses used in this setup have a duration on the order of 20 fs, which provides a high temporal resolution of the observed signals. The technique will turn out to be well suited for the presented ultrafast, all-optical studies.

In chapter 3 plasmon enhanced light-matter interactions are discussed with a view to modulators and switches for on-chip technologies. Two approaches are presented by means of so-called magneto-plasmonic crystals (MPCs). These hybrid metal-dielectric structures, which are specifically designed to support SPP modes, consist of a noble metal layer on top of a magnetic dielectric. The first approach exploits the magnetic character of the dielectric as a means to control the optical properties of the MPC via an interaction of the film magnetization with the SPP, which in this case is referred to as magneto-plasmon. The second approach concentrates on the manipulation of the MPC's optical properties by efficient SPP mediated light absorption into the noble metal, which influences the dielectric function of the metal on a femtosecond time scale. Due to the combination of MPCs with the possibility of femtosecond laser excitation, both approaches will point out ways to realize room-temperature, ultra-compact modulators with ultrafast response times.

In chapter 4 ultrafast dynamics are addressed in the manganite $YMnO_3$, which is a Mott insulator. The main objective of the chapter is to elucidate the physical mechanisms behind the ultrafast electronic processes induced by optical excitation. In accordance with the theory mentioned above, these dynamics will be shown to occur on timescales as fast as 10 fs due to the strong intrinsic electron-electron interactions. The physical origin is connected to a coherent electron momentum relaxation between degenerate sub-levels of the material's excited state. Two different effects will be discussed, which are triggered by circularly and linearly polarized light, respectively. The fact that these processes are temperature independent will identify $YMnO_3$ as a potential candidate for ultrafast optical switches and modulators operating at room-temperature.

In chapter 5, non-thermal ways for the ultrafast optical control of magnetization are investigated in magnetic iron garnets. In this material, experiments can be performed in the transparent regime, i.e., there is no absorption of light and thus only negligible heating of the sample (see, e.g., Kimel et al. [2005]). The experiments mainly focus on the inverse Faraday effect (IFE). The latter effectively induces a spin flip of the ground state electrons and thereby influences the magnetization. Depending on the polarization, the incident light changes the spontaneous magnetization or the anisotropy field of the crystal. Both effects result in a precession of the magnetization with periods on the order of 200 ps. The obtained knowledge is then applied to MPC structures in order to enhance the operation speed of the magneto-plasmonic approach presented in chapter 3. The optically induced effects are quasi-instantaneous, i.e., the time-scale of the interaction is only limited by the duration of the incident laser pulses. Hence, the presented results can be used to realize ultrafast magnetic switching in modern data storage technologies.

Chapter 1

Theoretical Background

This chapter provides the theoretical background for the discussion of experimental results in the ensuing chapters. Section 1.1 starts with an overview on surface plasmon polaritons (SPPs). The concept of SPPs and their fundamental properties will be first derived from Maxwell's equations. Then we will discuss the excitation of these surface waves on gratings with sub-wavelength periods for the case of a gold/garnet interface. The "empty lattice"-approximation is introduced as a model for the calculation of the SPP dispersion and estimation of the resonance condition for the coupling with light. The characteristic shape of the resonances in the spectra of transmitted and reflected light will be analyzed before we finally discuss the influence of magnetized media on the SPP properties and derive the corresponding form of the resonance condition.

Section 1.2 tends to the theory of the Mott insulator $YMnO_3$. The symmetry and selection rules originating from the crystal structure of $YMnO_3$ will be derived, which yields important insights for optically allowed transitions. Subsequently, the qualitative form of the dielectric permittivity tensor can be discussed with respect to the eigenmodes of the system and the concept of complex rotation will be explained. We then present a model for the interaction of circularly and linearly polarized light with $YMnO_3$ in the framework of optical alignment and optical orientation including a discussion of the eigenstates of the system and their relaxation mechanisms. The microscopic picture for the understanding of the interactions requires the density matrix formalism, the concept of which will be sketched briefly in order to provide a starting point for later approximations.

Finally, in section 1.3, we review the theory of the inverse Faraday effect (IFE), which represents the main mechanism for the non-thermal control of magnetization utilized in this work. The effect is explained from a thermodynamic point of view as well as discussed in a phenomenological picture. The interaction of the magnetization with the magnetic field is governed by the Landau-Lifshitz-Gilbert equation, which will be derived subsequently.

1.1 Surface Plasmon Polaritons

1.1.1 Fundamental Properties

Maxwell's equations show that a metal's electron plasma can be excited to perform coherent (longitudinal) oscillations known as plasmons. The characteristic frequency at which these oscillations occur is called the plasma frequency $\omega_p = ne^2/(\epsilon_0 m)$, where n is the electron density and ϵ_0 is the electric permittivity. For $\omega < \omega_p$ metals are mostly reflective with reflectivities $R \approx 1$. The optical excitation in this frequency range causes intraband transitions in the conduction band but the corresponding polarization wave cancels the incident wave in forward direction due to destructive interference, i.e., the propagation of electromagnetic waves is prohibited. Instead, electric fields decay rapidly within a skin depth δ. Only for $\omega > \omega_p$ do metals support electromagnetic modes and the optical response increasingly deviates from that of a free electron gas but instead obtains dielectric character. Since the electron density is usually high in metals, ω_p is typically in the visible to near ultraviolet wavelength range, which accounts for their high reflectivity known from everyday experience.

Yet, there exists one special type of plasma oscillation supported at frequencies below ω_p, which is only allowed when confined within a distance δ to the metal's surface. These surface plasmons or surface plasmon polaritons (SPPs) still have to fulfill Maxwell's equations

$$\operatorname{rot} \boldsymbol{H}_i = \epsilon_i \frac{1}{c}\frac{\partial}{\partial t}\boldsymbol{E}_i \tag{1.1}$$

$$\operatorname{rot} \boldsymbol{E}_i = -\frac{1}{c}\frac{\partial}{\partial t}\boldsymbol{H}_i \tag{1.2}$$

$$\operatorname{div} \epsilon_i \boldsymbol{E}_i = 0 \tag{1.3}$$

$$\operatorname{div} \boldsymbol{H}_i = 0 \tag{1.4}$$

at both sides of the interface ($i = (d, m)$, see figure 1.1). Restricting wave propagation in the x-direction with the z-axis normal to the surface, the fields in the two adjacent materials are taken to be

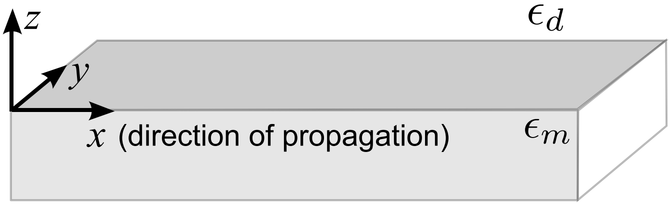

Figure 1.1: Schematic illustration of the surface plasmon propagation geometry along the surface of a metal with dielectric function ϵ_m adjacent to a material with dielectric constant ϵ_d.

$$\boldsymbol{E}_i = \begin{pmatrix} E_{x,i} \\ 0 \\ E_{z,i} \end{pmatrix} \exp i(k_{x,i}x \pm k_{z,i}z - \omega t) \tag{1.5}$$

$$\boldsymbol{H}_i = \begin{pmatrix} 0 \\ H_{y,i} \\ 0 \end{pmatrix} \exp i(k_{x,i}x \pm k_{z,i}z - \omega t) \tag{1.6}$$

with + (−) for $z > 0$ ($z < 0$), which corresponds to a TM-polarized mode. In general, it can be shown that for propagating modes confined to the interface of two adjacent materials, an ansatz with TE-polarized fields runs into inconsistencies with the continuity relations [Maier, 2007]

$$E_{x,m} = E_{x,d} \tag{1.7}$$

$$H_{y,m} = H_{y,d} \tag{1.8}$$

$$\epsilon_m E_{z,m} = \epsilon_d E_{z,d}, \tag{1.9}$$

i.e., surface plasmons are necessarily TM-polarized. From these relations it follows directly that $k_x = k_{x,m} = k_{x,d}$ is continuous across the interface. Moreover, when inserting the ansatz 1.5 and 1.6 into equations 1.1-1.4 and using equations 1.7-1.9, one obtains the relation (see Raether [1988])

$$k_x^2 + k_{z,i}^2 = \epsilon_i \left(\frac{\omega}{c}\right)^2 \tag{1.10}$$

as well as the system of equations

$$0 = H_{y,m} - H_{y,d} \tag{1.11}$$

$$0 = \frac{k_{z,m}}{\epsilon_m} H_{y,m} + \frac{k_{z,d}}{\epsilon_d} H_{y,d}. \tag{1.12}$$

This system of equations gives only a non-trivial solution if its determinant vanishes, which yields

$$\frac{k_{z,m}}{\epsilon_m} + \frac{k_{z,d}}{\epsilon_d} = 0. \tag{1.13}$$

Combining equations 1.10 and 1.13 we finally arrive at the important intrinsic equation, which contains the dispersion relation for surface plasmons

$$k_x = \frac{\omega}{c}\sqrt{\frac{\epsilon_m \epsilon_d}{\epsilon_m + \epsilon_d}}. \tag{1.14}$$

In general, all the dielectric constants as well as k_x are complex quantities. However, for the following discussion, absorption will be neglected for simplicity and all quantities considered real. It can be shown that for frequencies below ω_p, where the metallic character prevails, the real part of the metal's dielectric function, ϵ_m, is negative. For a propagating electromagnetic wave, the wavevector k_x is required to be real and positive, which according to equation 1.14 is only possible for $\epsilon_d > 0$ and further $|\epsilon_m| > \epsilon_d$, i.e., ϵ_d must be attributed to a dielectric. Now if these conditions are met, then $k_x > \frac{\omega}{c}$ and a closer examination of equation 1.10 reveals that for both materials $k_{z,i}$ has to be purely imaginary. Consequently, the electric fields decay in z-direction as $\exp(-|k_{z,i}|z)$ with their maximum at $z = 0$, i.e., the described electromagnetic wave is truly confined to the surface within the skin depths characteristic for the materials.

With δ_m typically on the order of 10 nm and δ_d usually amounting to a few hundred nanometers [Raether, 1988], SPPs are confined to volumes well below the optical diffraction limit. A sketch of the electric field distribution is given in figure 1.2. Obviously, the SPP is accompanied by a mixed transverse and longitudinal electric field with the magnetic field vector pointing in the y-direction.

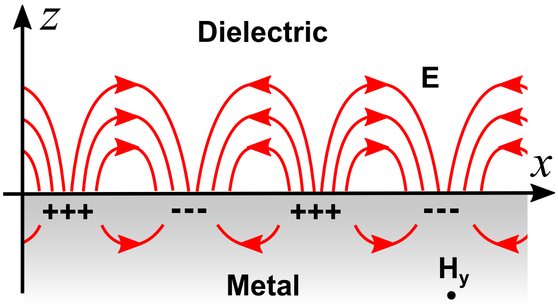

Figure 1.2: Schematic illustration of the electric field distribution induced by the charge density oscillations (+/−-symbols) of an SPP propagating in x-direction along the interface between a metal and a dielectric. H_y is the magnetic field in y-direction. (schematically adapted from Barnes et al. [2003])

1.1.2 Optical Excitation and Empty Lattice Approximation

The evaluation of equation 1.14 requires the knowledge of the two dielectric functions ϵ_m and ϵ_d. While ϵ_d in most cases can be considered to be only a slowly varying function of the frequency ω, which is approximately constant for most of the frequency ranges under consideration, this is usually not the case for metals (see discussion in section 1.1.1).

The choice of metal, which is the subject of the examinations described in this thesis, is the noble metal gold. The main reason for this choice is the large propagation length $L_i = (2k_x'')^{-1}$ for SPPs traveling along its interface. The imaginary part of the wavevector k_x'' depends linearly on the imaginary part of the metal's dielectric function ϵ_m''. In the near-infrared optical region, the absorption and thus ϵ_m'' is negligible so that this propagation length can be on the order of $100\,\mu$m. Although silver is even preferable in this respect, the surface is not inert to sulfidation, which spoils the reproducibility of experimental results.[1]

The dielectric function of gold is in first approximation very similar to that of the free electron plasma (see, e.g., Maier [2007]). However, its fully occupied 5d-orbitals lie so close to the Fermi energy that their influence on the optical response of the metal is significant. Moreover, these d-bands are so localized that they feel the strong core potential and consequently represent a highly polarized environment, which enters ϵ_m as a background contribution to the total polarization $\boldsymbol{P} = \epsilon_0(\epsilon_m - 1)\boldsymbol{E}$. For optical spectroscopy in the visible and near-infrared region, the relevant transitions occur around the L-point of the face-centered cubic (fcc) crystal structure of gold. Here, interband d-band to Fermi surface (p-band) transitions can be optically excited above photon energies of 2.4 eV (see solid arrow in figure 1.3), which has to be taken into account in the dielectric function. Hence, the free electron plasma expression has to be extended by the summand $\chi_{ib}' + i\chi_{ib}''$ considering the sum of all interband contributions. Here, χ_{ib}' and χ_{ib}'' are the real and imaginary part of the interband susceptibility. This interband term is in general frequency dependent. However, restricting the analyzed photon energy range to values below the d-band to Fermi surface transition, we can substitute this expression by the constant term $\epsilon_\infty - 1$ instead, which only accounts for the background

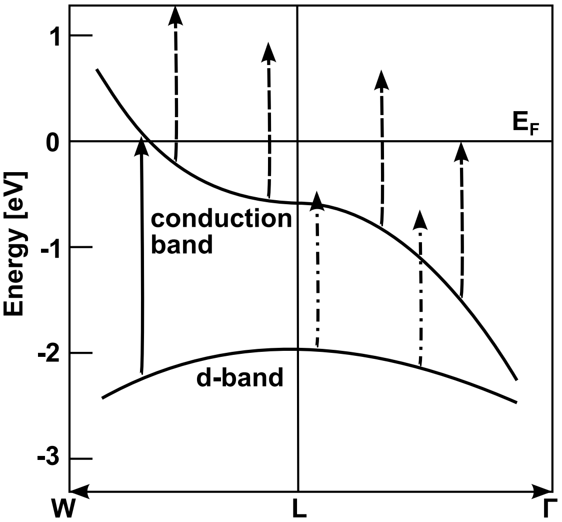

Figure 1.3: Schematic illustration of the band structure of gold around the L-point of the fcc crystal structure of gold. The sketch is a detail of a non-relativistic augmented-plane-wave (APW) calculation originally performed by Christensen and Seraphin [1971]. The solid arrow The dashed and dotted-dashed arrows represent optically excited intra- and interband transitions, respectively, with a photon energy of 1.55 eV while the solid arrow stands for d-band to Fermi-surface transitions setting in above 2.4 eV.

---

[1] Silver is not affected by oxygen but reacts with hydrogen sulfide, H_2S, which is always present in the air to a small amount. The product of this chemical reaction is silver sulfide, Ag_2S, which gives the silver surface a black color [Riedel and Janiak, 2011].

polarization originating from the d-bands, so that ϵ_m takes the form

$$\epsilon_m(\omega) = \epsilon_\infty - \frac{\omega_p^2}{\omega^2 + i\gamma\omega}, \tag{1.15}$$

where γ is the electron scattering rate and ω_p is the plasma frequency.

With equations 1.14 and 1.15 a realistic calculation of the dispersion relation for a surface plasmon propagating along the metal surface can be performed. The results of such a calculation for the SPP at the gold/air interface are represented by the red dashed line in figure 1.4 for $\omega_p = 1.34 \cdot 10^{16}\,\mathrm{Hz}$, $\epsilon_\infty = 7.9$ and $\gamma = 11.3 \cdot 10^{13}\,\mathrm{Hz}$. The edge of the shaded area is the calculated dispersion of light in vacuum with wavevector $k_0 = \omega/c$. At all points, the SPP dispersion lies to the right of this light line, which is a consequence of the SPP's bound nature. The resulting wavevector mismatch prevents the direct excitation of surface plasmons by light. Techniques to excite SPP modes therefore use, e.g., a prism, which is either directly positioned on top of a thin metal film [Kretschmann and Raether, 1968] or with an air gap in between [Otto, 1968] to optically excite an evanescent wave at the metal's interface via attenuated total reflection (ATR). This wave has a larger momentum with respect to light traveling in air due to the optically thicker prism material and is subsequently able to fulfill the SPP resonance condition at the metal/air interface, where it couples to a surface plasmon mode. Apart from the aforementioned prism coupling methods, sub-wavelength periodic structures, e.g., gratings at either of the two adjacent materials' surfaces can be used to provide the missing momentum, which is more preferable for eventual nanoplasmonic applications.[3]

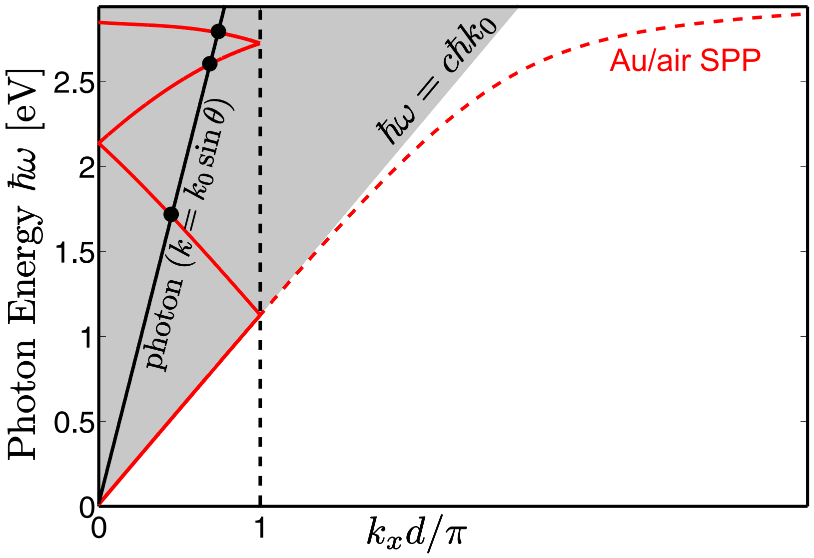

Figure 1.4: Calculated SPP dispersion on a smooth gold surface (red dashed line) and on a sub-wavelength grating with grating constant d in the empty lattice approximation (red solid line). The shaded area represents the points accessible for SPP excitation with light, which is incident under an angle θ and has an in-plane momentum $k_x = k_0 \sin\theta$ (black solid line). The dashed vertical line visualizes the edge of the 1.BZ. At the intersections (full circles) of the folded SPP and photon dispersions, SPP excitation with light is possible.[2]

---

[2] As mentioned in the text, interband corrections to this calculation are to be expected for energies above 2.4 eV.

[3] ...although there are also near-field methods to overcome the wavevector mismatch. In plasmon enhanced near-field scanning optical microscopy (NSOM) experiments, a metal coated fiber tip is used

The periodicity of the grating restricts the plasmon wavevector to $k_x = \pi/d$ within the first Brillouin zone (1.BZ), where d is the grating constant and the structure is periodic in the direction of SPP propagation (the x-direction). At the edge of the 1.BZ, the SPP dispersion is folded back into the shaded area (see red solid line in figure 1.4). This area represents the points of the dispersion that are accessible to photons incident under an angle θ with respect to the surface normal. Consequently, the dispersion of these photons has intersections with the folded SPP dispersion, at which optical surface plasmon excitation is allowed and phase-matching occurs whenever

$$k_{\mathrm{SPP}} \pm m\frac{2\pi}{d} = k_{\mathrm{photon}} \sin\theta, \tag{1.16}$$

where m is an integer number. These excitations are also referred to as surface plasmon polaritons (SPP) since they are a mixture of an electromagnetic and a polarization wave (see, e.g., figure 1.2) [Raether, 1988]. At central photon energies around 1.55 eV, which is well below the surface plasmon energy of $\hbar\omega_{sp} = 3.61\,\mathrm{eV}$ in gold,[4] the deviation of the SPP dispersion with respect to that of light is almost negligible. In other words, in our case the SPP has mainly photon character and consequently can be regarded as light guided along the metal surface.

The calculations were performed under the condition that the grating is periodic (in this case $d = 550\,\mathrm{nm}$) but with slits that are infinitesimal thin so that the dispersion relation 1.14 can be used, which was derived for a smooth gold surface. This is called the empty lattice approximation. Moreover, it is only valid for grating periods significantly smaller than the SPP wavelength since otherwise the plasmon would not “feel” the periodicity of the grating. In reality, the finite slit widths can lead to the formation of standing plasmon waves and band gaps at the edges of the 1.BZ similar to the ones formed by electronic standing waves in a crystal lattice. However, at all other points of the BZ, the empty lattice approach provides an excellent approximation, which can be used to design the investigated structures in order to provide resonances at suitable energies and light incidence angles.

It should be noted that, contrary to uniform films, the optical properties of perforated metals can inherit other eigenmodes and anomalies, such as Rayleigh anomalies or Fabry-Perot resonances, which show as transmission/reflection dips or peaks in the respective spectra as well [Marquier et al., 2005; Porto et al., 1999]. While Rayleigh anomalies are related to electromagnetic field singularities when one of the diffracted orders becomes tangential to the grating surface, Fabry-Perot resonances are the result of constructive interference inside the grating slits. Both phenomena are determined by the grating parameters, i.e., by the grating period and the slit depth and width, respectively.

1.1.3 Fano Resonances and Damping Mechanisms

As described by Fano [1961], whenever two states of different “configuration” but identical energy are mixed by different excitation paths, interference can occur due to the superposition principle of quantum mechanics. A vivid and extensively investigated

---

to excite surface plasmons at the tip apex, where the radius is too small to guide the fiber modes. The tip SPPs couple to the SPPs on a sample surface similar to the Kretschmann method via tunneling [Bouhelier et al., 2003]. In order to suppress the background and improve the signal-to-noise ratio of near-field scanning approaches, Zhang et al. [2013] used a silver coated scanning probe with an implemented grating, which couples free space light adiabatically into propagating SPP modes at the probe tip. The collected near-field signal, in contrast to the background, is strongly modulated due to an up-and-down tapping motion of the scanning probe at the sample surface with a constant “tap”-frequency.

[4] $\omega_{sp} = \omega_p/\sqrt{1+\epsilon_d}$, with plasma frequency $\omega_p = 13.4 \cdot 10^{15}$ Hz and $\epsilon_d = 4.97$.

example is that of the excitation of auto-ionizing discrete atomic energy levels interfering with direct transitions to the continuum giving rise to characteristic asymmetric resonances in the excitation spectra (see, e.g., Miroshnichenko et al. [2010]). The auto-ionizing transition is established, e.g., by a two-electron Auger effect if the incident photon energy is higher than the first ionization energy of the atom. Yet, across the resonance energy the phase of the electron wave function acquires a phase shift of π with respect to the continuously excited electron leading to constructive and destructive interference, respectively.

In plasmonics, Fano resonances usually appear in optical transmission and reflection spectra when excitations of SPPs are involved. While light can obviously be transmitted and reflected "directly" (i.e., forward and backward scattering into a continuum of states), the discrete scattering channel happens via SPP excitation, which is a resonant process, and subsequent re-radiation into the continuum at the same optical frequencies. Consequently, the measured light intensity I has a resonant contribution, I_r, and a non-resonant one, I_{nr}, i.e.,

$$I = I_r + I_{nr}, \tag{1.17}$$

Depending on their ratio, the interference and the asymmetry of the resonances is more or less pronounced with a shape showing a minimum as well as a maximum instead of the usual dip or peak. Equally, the intensity ratio determines the position of the resonance in between these two extrema. Quantitatively, Fano features observed in optical spectra can be described by

$$I = \sum_{i=1} A_i (1 + E_i Q_i)^2 / (1 + E_i^2) + D, \tag{1.18}$$

where $E_i = (\omega - \omega_i)/(\Gamma_i/2)$ and $D = D_0 + D_{\text{lin}}\omega$. A_i, ω_i and Γ_i are the amplitude, position and width of the ith resonance. Q_i is a phenomenological shape parameter taking into account the degree of asymmetry described earlier. All remaining weak spectral features, which can be considered slowly varying functions of the photon frequency ω, are covered by the background parameter D if necessary.

An example of spectra containing Fano resonances is provided in figure 1.5. These spectra were measured with white light incident under an angle $\theta = 10°$ on a 120 nm thick sub-wavelength gold grating of period $d \approx 500$ nm on top of a dielectric garnet film with permittivity $\epsilon_d = 4.5$, which is transparent for the investigated range of photon energies. The surface plasmons with energies 1.77 eV and 1.87 eV excited at the interface lead to an enhanced transmission through the otherwise non-transparent gold layer of 5.5 % and 3.8 %, respectively. In reflection, the Fano features show up as a significant loss of light intensity. The solid lines represent fits to the spectra with equation 1.18. In both cases the ratio I_{nr}/I_r is either very large or very small, so the degree of asymmetry in each of the resonances is rather small with $Q \ll 1$. The fits correspond well to the experimental data although in transmission, the signal is superposed by weak Fabry-Perot oscillations, which originate from interfering reflections inside the 5 μm thick dielectric layer. In reflection, this interference is suppressed since the dielectric is located at the backside of the gold film. The resonance positions are in good agreement with empty lattice calculations of the respective SPP energies at the given angle of incidence (not shown here). Remarkably, the absorption reaches values of 67 % and 86 % at the SPP energies

---

[5] Since there are no higher refraction orders present apart from the zero order refraction for the angles of incidence in the measured energy region, the absorption has been calculated as $A = 1 - R - T$.

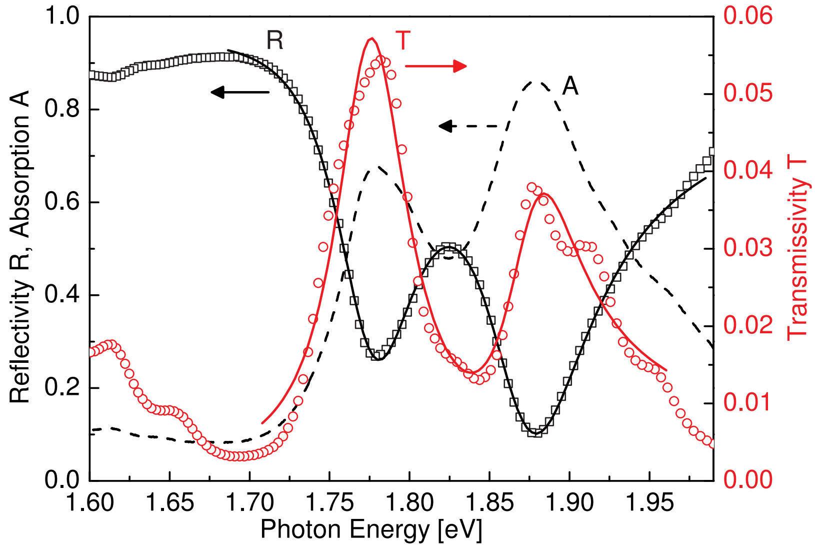

Figure 1.5: Fano resonances in the reflectivity (empty squares) and transmissivity (empty circles) spectra originating from SPP excitations at the interface of a gold grating and a transparent dielectric garnet film ($\epsilon_d = 4.5$, $d \approx 500\,\text{nm}$) under an angle of incidence $\theta = 10°$. Solid lines represent fits with equation 1.18 to the two resonances at 1.77 eV and 1.87 eV. Also shown is the absorption A (dashed line) in the given frequency range.[5]

even though the reflectivity coefficient of gold is close to 1 for photon energies below 2 eV. This demonstrates the role of SPPs for enhancing light matter interactions by means of effective concentration of light energy into the material.[6]

The energy coupled to a surface plasmon mode is damped by two major mechanisms, i.e., radiation and internal damping, respectively. The former usually occurs in layer systems with non-identical interfaces, e.g., air/metal and metal/dielectric with $\epsilon_d > 1$. If the thickness of the metal layer is comparable to the skin depth δ_m, SPPs generated at the air/metal interface may tunnel to the metal/dielectric interface, where the wavevector mismatch with respect to the light dispersion can be overcome due to the higher refraction index of the dielectric. Consequently, the SPPs will couple to the light field and are re-radiated from the respective surface. More importantly, in the common case of the transparent regime, i.e., with photon energies lower than any electronic transition in the dielectric, an internal absorption occurs in the metal, whose strength is determined by the imaginary part of the SPP's wavevector $k_x''(\omega)$. Since the central photon energy of the utilized laser source (see section 2.1) is well below the interband transition energy in gold, the SPP energy dissipates into the electron system of the metal via intraband transitions in the conduction band close to the Fermi level (see dashed arrows in figure 1.3). The subsequent relaxation processes are frequently described by the two-temperature model (TTM). The TTM and its extension, the non-thermal electron model (NEM) will be described in section 3.2.2.

1.1.4 Gyrotropic Media and Non-Reciprocity

The presence of a magnetization in a medium imposes certain symmetry properties to the corresponding dielectric permittivity tensor $\hat{\epsilon} = \hat{\epsilon}' + i\hat{\epsilon}''$, reducing it to the single axis

---

[6] In this case, the high absorption originates from internal damping in the metal's electron system, i.e., intraband transitions in the conduction band and subsequent interband transitions from the d-band to the conduction band.

one. In isotropic crystals, a linear relation between the dielectric displacement vector $\boldsymbol{D}$ and the electric field vector $\boldsymbol{E}$ can be derived from these symmetry considerations, reading [Landau et al., 1995]

$$D_i = \epsilon'_{ik} E_k + i(\boldsymbol{E} \times \boldsymbol{g})_i, \tag{1.19}$$

where $\boldsymbol{g}$ is the gyration vector, which is connected to the optical activity vector $\boldsymbol{G}$ by

$$G_i = -\frac{1}{\det \hat{\epsilon}} \epsilon'_{ik} g_k. \tag{1.20}$$

The form of ϵ_{ik} can be taken directly from equation 1.19 to be[7]

$$\hat{\epsilon} = \begin{pmatrix} \epsilon_d & 0 & ig_y \\ 0 & \epsilon_d & -ig_x \\ -ig_y & ig_x & \epsilon_d \end{pmatrix}, \tag{1.21}$$

where ϵ_d is the dielectric function of the isotropic non-magnetized dielectric film. Materials, which obey equation 1.19 are said to be gyrotropic. They form an important material class not only in plasmonics but in general for magneto-optics, since phenomena related to magnetic circular birefringence or magnetic circular dichroism (MCD) are closely connected to the gyration. Hence, a similar form of the tensor 1.21 will be of importance in chapter 4 as well. In the case of isotropy $\boldsymbol{g} = a\boldsymbol{M}$ depends linearly on the magnetization. In equation 1.21, $\boldsymbol{M}$ has been assumed to be oriented in the plane of the magnetized medium, i.e., the xy-plane.

Near the surface of a medium, the localized charges lead to a constant electric field $\boldsymbol{E}$ pointing in the direction of the surface normal vector $\boldsymbol{N}$, which breaks the spatial inversion symmetry of the system. Additionally, an in-plane magnetization breaks the time inversion symmetry for surface waves propagating perpendicular to $\boldsymbol{M}$. In this geometry, surface waves travel either parallel or anti-parallel to a toroidal moment $\boldsymbol{T}$ arising from the nonzero vector product $\boldsymbol{M} \times \boldsymbol{E}$ near the surface, i.e., $\boldsymbol{T} \propto \boldsymbol{M} \times \boldsymbol{E}$. As a consequence, the wavevector of a TM polarized SPP mode changes, when its direction of propagation is reversed with respect to $\boldsymbol{M}$, which is referred to as non-reciprocity [Kalish et al., 2007].

A quantitative expression for this non-reciprocity can be found by a similar treatment of the Maxwell equations as sketched in section 1.1.1, which now includes a magnetization that is restricted in the y-direction and the metal (m) is adjacent to a gyrotropic dielectric (d) on the one and to air (0) on the other interface, respectively. Keeping to the geometry depicted in figure 1.1 and taking into account the respective boundary conditions, this leads to a dispersion law reading [Belotelov et al., 2009]

$$0 = \eta_m \left(\eta_0 + \eta_d - g_y \frac{\kappa}{\epsilon_d^2} \right) + \left[\eta_0 (\eta_d - g_y \frac{\kappa}{\epsilon_d^2}) + \eta_m^2 \right] \tanh(\gamma_m d), \tag{1.22}$$

where $\eta_i = \gamma_i / \epsilon_i$, $\gamma_{0,m} = \sqrt{\kappa^2 - \epsilon_{0,m} k_0^2}$, $\gamma_d = \sqrt{\kappa^2 - \epsilon_d k_0^2 + k_0^2 g^2 / \epsilon_d}$ and $k_0 = \omega / c$. κ and γ_i are the longitudinal and lateral wavevectors in the medium i of the plasmon wave propagating in x-direction with magnetic field $H_y \exp(i\kappa x + \gamma_i z)$ $(i = (m, d, 0))$. Expression 1.22 only holds for $g \ll \epsilon_d$ and can be further simplified if the metal film thickness

---

[7] Since the electric dipole response at optical frequencies is very weak, the magnetic permeability μ is taken to be unity [Landau et al., 1995].

d is large enough to apply $\gamma_m d \to \infty$. Both conditions are valid in the investigated samples so that one can write

$$\kappa = k_{\mathrm{SPP}} = \kappa_0(1 + \alpha g_y), \tag{1.23}$$

with $\kappa_0 = k_0[\epsilon_m\epsilon_d/(\epsilon_m + \epsilon_d)]^{1/2}$ and $\alpha = (-\epsilon_m\epsilon_d)^{-1/2}(1 - \epsilon_d^2/\epsilon_m^2)^{-1}$. It is exactly the described nonreciprocal geometry, in which the transverse magneto-optical Kerr effect (TMOKE) is observed. In section 3.1.2, it will be shown that the inclusion of surface plasmon waves will enhance the TMOKE by roughly an order of magnitude due to the non-reciprocity effect.

1.2 Optical Anisotropy in YMnO$_3$

1.2.1 Group-Theoretical Considerations

The non-centro-symmetric hexagonal crystal structure of YMnO$_3$ can be seen in figure 1.6a and 1.6b with a view perpendicular and parallel to the 6-fold symmetric c-axis, respectively. The crystal consists of non-connected layers of Y^{3+} and Mn^{3+} ions, where the latter are coordinated by three in-plane and two apical O^{2-} ions in a trigonal bipyramid. These bipyramids are corner-linked via the in-plane O^{2-} ions as shown in figure 1.6b. The apical oxygen ions form close-packed planes separated by the yttrium ions.

The crystal structure belongs to the point group C$_{6v}$. Its character table is shown in table 1.1. From a group theoretical point of view, the unperturbed Hamiltonian for this system is invariant under all symmetry operations of the C$_{6v}$ group, which include rotations of 180°, 120° and 60° about the symmetry c-axis (C$_2$, 2C$_3$ and 2C$_6$, respectively) as well as reflections in planes containing the c-axis and in planes vertical to the c-axis (σ_d and σ_v, respectively).

C$_{6v}$ (6*mm*)	E	C$_2$	2C$_3$	2C$_6$	3σ_d	3σ_v
Γ_1	1	1	1	1	1	1
Γ_2	1	1	1	1	-1	-1
Γ_3	1	-1	1	-1	-1	1
Γ_4	1	-1	1	-1	1	-1
Γ_5	2	-2	-1	1	0	0
Γ_6	2	2	-1	-1	0	0

Table 1.1: Character table for the point group C$_{6v}$. The first column gives the irreducible representations, while the first row lists the symmetry operations of the crystal. The numbers represent the characters, i.e., the traces of the representation matrices, which describe the transformation properties of an operator or a state under the different symmetry operations of the group (see, e.g., Tinkham [2003]).

For optical experiments, it is important to consider the impact of a perturbation of this system by incident electromagnetic radiation. Here, the electric dipole operator $\hat{\mu} = e\hat{r}$ represents the most important contribution to this perturbation since the oscillator strengths of higher order electric and magnetic dipole transitions are significantly weaker. The electric dipole operator transforms as a polar vector (V), i.e., like the coordinates (x, y, z). In group theory, these transformation or symmetry properties are described by so-called representations, which are a set of matrices or their traces, which unambiguously describe the behavior of a vector or an operator under the symmetry operations of the point group. Eventually, these matrices can be decomposed and reduced in their dimensionality (see, e.g., the block-matrix form of $\Gamma^V(C)$ in equation 1.24 below). If this is not the case, the representation is called irreducible. The symmetry of $\hat{\mu}$

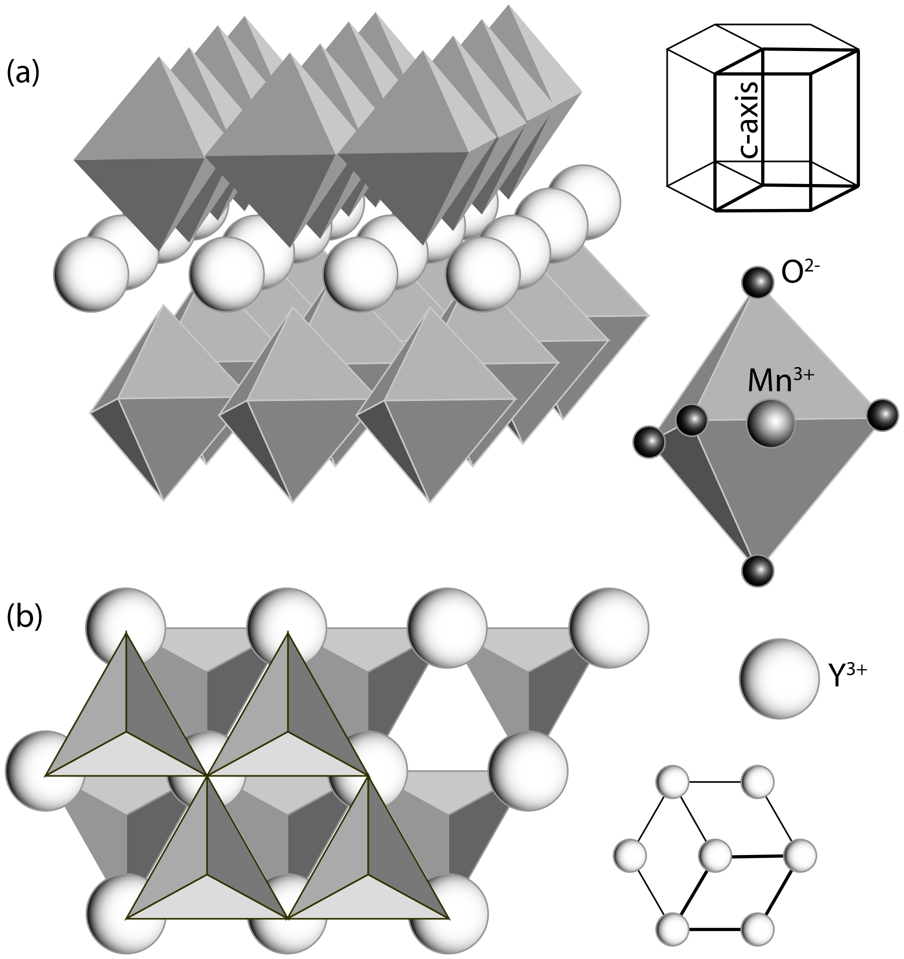

Figure 1.6: Crystal structure of hexagonal YMnO$_3$ with a view (a) perpendicular and (b) parallel to the high symmetry c-axis (schematically adapted from Aken et al. [2001]). Also shown is a close-up of one of the trigonal bipyramids, whose corners are occupied by O^{2-} ions with an Mn^{3+} ion in its center.

can be expressed via the irreducible representations by writing down a set of (reducible) representation matrices and examining their characters:

$$\Gamma^V(C) = \begin{pmatrix} \cos(\varphi) & -\sin(\varphi) & 0 \\ \sin(\varphi) & \cos(\varphi) & 0 \\ 0 & 0 & 1 \end{pmatrix} \qquad \Gamma^V(\sigma_d) = \begin{pmatrix} -1 & 0 & 0 \\ 0 & 1 & 0 \\ 0 & 0 & 1 \end{pmatrix}$$

$$\Gamma^V(\sigma_v) = \begin{pmatrix} 1 & 0 & 0 \\ 0 & 1 & 0 \\ 0 & 0 & -1 \end{pmatrix} \qquad \Gamma^V(E) = \begin{pmatrix} 1 & 0 & 0 \\ 0 & 1 & 0 \\ 0 & 0 & 1 \end{pmatrix}, \qquad (1.24)$$

where C denotes the rotations through φ about the z-axis. Since the characters of this reducible representation, which are listed in table 1.2, can be decomposed into the sum of the characters of the irreducible ones in a unique way (see, e.g., Tinkham [2003]), we can write $\Gamma^V = \Gamma_1 + \Gamma_5$ just by looking at the character table 1.1. It is important to note that z, which is the direction of the high symmetry axis (c-axis), belongs to Γ_1, the identical representation, since it is invariant under any group operation. (x, y) on the other hand, transform as Γ_5. Hence, the selection rules for electronic transitions induced by radiation polarized in the xy-plane are determined by Γ_5.

C_{6v} ($6mm$)	E	C_2	$2C_3$	$2C_6$	$3\sigma_d$	$3\sigma_v$
Γ^V	3	-1	0	2	1	1

Table 1.2: The reducible representation Γ^V of the electric dipole operator $\hat{\mu}$ in the C_{6v} group.

Just as the unperturbed Hamiltonian, the ground state of the system is invariant under all group operations and hence transforms as Γ_1. In order to know, between which states electric dipole transitions are allowed, we need the selection rules. Since the system's eigenfunctions belonging to different representations are orthogonal, the product of the perturbation Hamiltonian $\hat{V}$ with the final state φ must contain the representation of the initial state Ψ for the scalar product $(\Psi, \hat{V}\varphi)$ to be non-zero ($\hat{V}_{ij} = -\hat{\mu}_{ij}E_j$ and $\boldsymbol{E}$ is the electric field of the incident radiation). If the initial state is to be the ground state and the radiation is polarized in the xy-plane, the only allowed transition is to a state of Γ_5 symmetry since only then can the product $\hat{V}\varphi$ be decomposed to contain the ground state representation:

$$\Gamma_{\hat{V}} \times \Gamma_{\varphi} = \Gamma_5 \times \Gamma_5 = \Gamma_6 + \underline{\Gamma_1} + \Gamma_2. \tag{1.25}$$

Here, the first and second terms are (reducible) direct product representations, whose character is simply the product of the characters of the component representations [Tinkham, 2003]. Γ_5 is a (irreducible) two-dimensional representation. Hence, the Γ_5 state is doubly degenerate and commonly labeled $|x, y\rangle$ due to its transformation properties. It can be easily seen from a multiplication table of C_{6v} or from a decomposition of the direct product of Γ_5 with the remaining representations (similar to equation 1.25) that neither of them contain Γ_1 and transitions to these states are therefore not allowed from the ground state. Similarly, it can be found that electric dipole transitions are not allowed for light polarized along the z-direction (the direction of the hexagonal c-axis).

The ground state of $YMnO_3$, i.e., the top of the valence band is formed by the oxygen $2p$ states. These states are strongly hybridized with manganese $3d_{xz}/3d_{yz}$ and $3d_{xy}/3d_{x^2-y^2}$ states, where the subscripts represent the different transformation properties of the respective wave functions. Despite the hybridization, the oxygen $2p$ states dominate the density of states near the Fermi level and hence the ground state [Choi et al., 2008a]. A hint to an electric dipole transition was found by Kalashnikova and Pisarev [2003], who performed polarized ellipsometry measurements on rare earth manganites. They observed a strong, nearly 100 % polarized optical absorption around 1.6 eV for light polarized in the xy-plane. As discussed before, the characteristic polarization sensitivity and the high oscillator strength of this transition strongly point to its electric dipole nature, which can only occur between states of different angular momentum. Therefore, in the case of $YMnO_3$, it has been suggested that the transition takes place between the hybridized $O^{2-}(2p)$-$Mn^{3+}(3d)$ and the $Mn^{3+}(3d_{3z^2-r^2})$ states, which have Γ_5 symmetry. This model is supported by recent first principle calculations and experimental studies of hexagonal manganites [Choi et al., 2008a,b; Moskvin and Pisarev, 2010]. Hence, in the following, the 1.6 eV transition will be treated as the charge-transfer electric dipole transition from the $O^{2-}(2p)$-$Mn^{3+}(3d)$ ground state to the doubly degenerate $Mn(3d)$ states. Since the central photon energy of our laser pulses (1.55 eV) is very close to this resonance, it is the described charge-transfer transition that will determine the physics behind the experiments discussed in chapter 4.

1.2.2 The Dielectric Permittivity Tensor

According to the group theoretical discussion of section 1.2.1, electric dipole transitions are symmetry forbidden for light polarized along the hexagonal c-axis ($\equiv z$-axis). Consequently, in our experiments we excite the sample with the light wavevector k at small angles with respect to the z-axis, i.e., $E_z \approx 0$. In this case, the photo-induced changes of the complex dielectric permittivity tensor of hexagonal YMnO3 can be written as [Kahn et al., 1969; Pershan, 1967]

$$\hat{\epsilon} = \begin{pmatrix} \epsilon_\perp + \epsilon_2 & i\epsilon_1 & 0 \\ -i\epsilon_1 & \epsilon_\perp - \epsilon_2 & 0 \\ 0 & 0 & \epsilon_\| \end{pmatrix}, \tag{1.26}$$

The eigenvalues λ of this tensor can be found by writing $\det(\hat{\epsilon} - \lambda\hat{E}) = 0$. We find

$$(\lambda^2 - 2\epsilon_\perp\lambda + (\epsilon_\perp^2 - \epsilon_2^2 - \epsilon_1^2))(\epsilon_\| - \lambda) = 0. \tag{1.27}$$

The most obvious of the three solutions is $\lambda_z = \epsilon_\|$ for light polarized along z. For light polarized in the xy-plane, the two remaining solutions are

$$\lambda_\pm = \epsilon_\perp \pm \sqrt{\epsilon_1^2 + \epsilon_2^2}. \tag{1.28}$$

With these eigenvalues we find the relation between the x and y components of the eigenvectors (a second relation can be obtained describing the same solution)

$$x = \frac{i\epsilon_1}{\pm(\epsilon_1^2 + \epsilon_2^2)^{1/2} - \epsilon_2} y. \tag{1.29}$$

A close examination of this expression reveals the nature of the tensor elements in equation 1.26. Setting $\epsilon_2 = 0$ in equation 1.29 yields an eigenvector that is circularly polarized in the xy-plane, where the $+$ and $-$ signs determine right or left-handed orientation. Consequently, the magneto-optical effects induced by circularly polarized light are determined by ϵ_1. On the other hand, if we set $\epsilon_1 = 0$, we have to distinguish between the $+$ and the $-$ sign. In the one case the ratio $x/y = 0$ and the light is linearly polarized in the y-direction. In the other case, $\lim_{\epsilon_1 \to 0} x/y = \infty$[8] and the light is linearly polarized in the x-direction. Hence, the optically induced effects originating from linearly polarized light are determined by ϵ_2.

In pump-probe experiments, the pump beam induces the changes of the optical properties described by the tensor 1.26. Dependent on the polarization of the pump electric field, the incident probe light experiences a different effective refractive index, e.g., $n_{\text{eff}}^2 = \epsilon_\perp + \epsilon_1$ for right circularly polarized pump light. The incident and reflected probe polarizations $\boldsymbol{E}_i$ and $\boldsymbol{E}_r$, respectively, can always be expressed or decomposed via the normal modes described above. That way, the changes imposed on $\boldsymbol{E}_r$ can be obtained via the Fresnel equations, where the refractive indices are substituted by the eigenvalues corresponding to the respective normal modes. Once $\boldsymbol{E}_r$ is found, the rotation and ellipticity angle of the polarization ellipse (in a general case, the incident light is elliptically polarized) θ and Ψ, respectively, are calculated via [Zvezdin and Kotov, 1997]

$$\begin{aligned} \tan 2\theta &= \frac{2\Re(E_{r,y}/E_{r,x})}{1 - |E_{r,y}/E_{r,x}|^2} \\ \sin 2\Psi &= \frac{2\Im(E_{r,y}/E_{r,x})}{1 + |E_{r,y}/E_{r,x}|^2}. \end{aligned} \tag{1.30}$$

---

[8] This can be verified easily by applying l'Hospital's rule, since the numerator and the denominator tend to the same boundary value in this case.

Substituting the electric field components in equation 1.30 by the expressions obtained via the Fresnel equations, the rotation and ellipticity experienced by the probe beam can be written as the real and imaginary part of one complex quantity $\Theta = \theta + i\Psi$ depending only on the different components of the permittivity tensor. For the generalized case of elliptically polarized pump excitation and a linearly polarized probe beam, this quantity reads

$$\theta + i\Psi = -\frac{i\epsilon_1 + \epsilon_2 \sin(\alpha)}{\sqrt{\epsilon_\perp}(\epsilon_\perp - 1)}, \tag{1.31}$$

where α is the angle between the main axis of the pump ellipse and the probe polarization axis [Kahn et al., 1969]. Θ will be referred to as the “complex rotation” in the remainder of this text.

1.2.3 Photo-Induced Linear and Circular Optical Anisotropy

The effects, originating from ϵ_1 or ϵ_2, are both related to optical perturbations of the electronic angular momentum distribution. In either case, the optically induced anisotropy originates from the contributions ϵ_1 and ϵ_2 to the eigenvalues of the permittivity tensor, resulting in a difference $\lambda_+ - \lambda_-$ in equation 1.28 and thus also in the eigenstates. The magnitude of the corresponding optical and magneto-optical phenomena depends on whether resonant or off-resonant conditions are met in the experiment.

In case of circularly polarized pump excitation, the angular momentum ± 1 of the absorbed light is transferred to the medium creating a non-equilibrium electron distribution with nonzero net angular momentum. The circular eigenstates of the perturbed system can be written as linear combinations of the $|x\rangle$ and $|y\rangle$ states described in section 1.2.1 and consequently have the same transformation properties. These so-called circular excitons read

$$|+\rangle = \frac{1}{\sqrt{2}}(|x\rangle + i\,|y\rangle) \tag{1.32}$$

$$|-\rangle = \frac{1}{\sqrt{2}}(|x\rangle - i\,|y\rangle), \tag{1.33}$$

where the states $|\pm\rangle$ are characterized by the z projection J_z of the total angular momentum in $\pm$ direction along the quantization (z-) axis, respectively, as illustrated in figure 1.7b. The non-zero electric dipole elements have the same value as in the case of linear excitons $|x, y\rangle$, i.e.,

$$\langle g|\,\hat{\mu}_x\,|x\rangle = \langle g|\,\hat{\mu}_y\,|y\rangle = \langle g|\,\hat{\mu}^+\,|+\rangle = \langle g|\,\hat{\mu}^-\,|-\rangle = \mu, \tag{1.34}$$

where $\hat{\mu}^\pm = 1/\sqrt{2}(\hat{\mu}_x \pm i\hat{\mu}_y)$. Due to the difference in the eigenvalues, the left and right circular components of a subsequent probe pulse will experience different refractive indices, i.e., different phase velocities and absorptions, giving rise to circular birefringence and dichroism, respectively.

In the picture of the electric dipole approximation, the electric field of light acts on the electron motion (Δl) and not on the spin (Δm). Consequently, the angular momentum of circularly polarized light is transferred to the orbital momentum of the electron. However, the electron spin can be oriented via the spin-orbit interaction creating a non-equilibrium spin polarization. The spin breaks the symmetry in the orientations of the electronic orbital momenta, i.e., the system is able to distinguish between the senses of circular polarization due to the coupling. Although spin independent contributions to ϵ_1

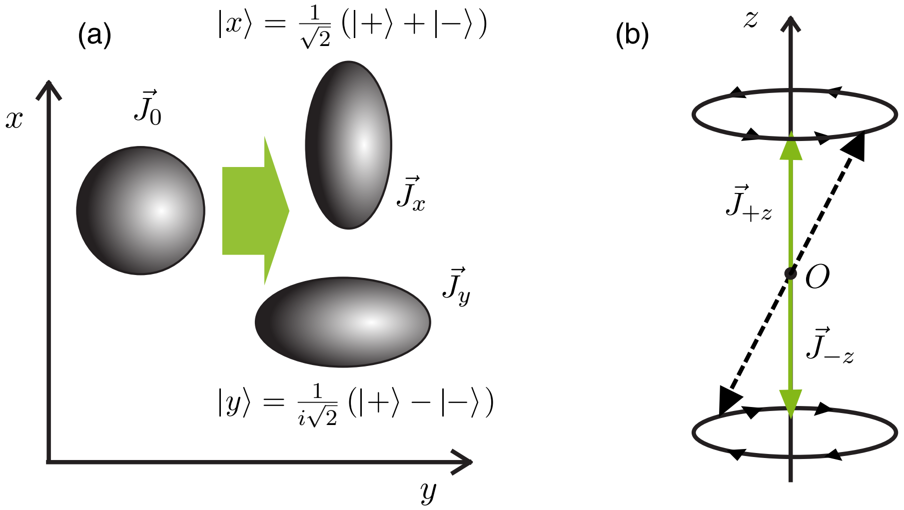

Figure 1.7: Schematical illustrations of the (a) optical alignment of the angular momentum distribution of an electronic s-orbital in the xy-plane due to linearly polarized excitation and (b) the optical orientation of angular momentum as characterized by the total angular momentum projection J_z due to circularly polarized excitation.

exist, effects originating from spin orbit interaction are orders of magnitude larger [Kahn et al., 1969]. Hence, ϵ_1 describes the magneto-optical effects and is related to phenomena such as optical orientation [Meier and Zakharchenya, 1984] and the inverse Faraday effect [Kirilyuk et al., 2010]. The effect will be referred to as circular optical anisotropy throughout the rest of the text. Especially, since the light wavevector is directed in the z direction, which is perpendicular to the sample surface, the spin polarization will be oriented in the z direction as well and the effects must be attributed to the complex polar Kerr effect (see figure 3.2a in section 3.1).

Since linearly polarized light carries zero net angular momentum, the optically induced anisotropy by a correspondingly polarized pump beam cannot be characterized by the total angular momentum projection J_z, which in this case is not a good quantum number, nor can the quantization axis be the z-axis. Instead, the quantization axis is identical to the polarization axis of the pump beam and the total electron momentum distribution will be elongated in the direction of its electric field vector, which breaks the axial symmetry and creates a linear angular momentum anisotropy in the xy-plane. This situation is illustrated in figure 1.7a for the optical alignment of an isotropic s-orbital. A subsequent linearly polarized probe pulse with a polarization axis forming an angle $\alpha \neq 0$ with the anisotropy axis will experience different refractive indices for its linear components, i.e., linear birefringence and dichroism. Hence, ϵ_2 describes the optically induced effects related to optical alignment [Meier and Zakharchenya, 1984], photo-selection [Michl and Thulstrup, 1995] and optical Kerr effect [Saleh and Teich, 2007]. In the following, the corresponding effects will be referred to as photo-induced linear optical anisotropy.

In the $|\pm\rangle$ basis, the linear eigenstates $|x, y\rangle$ are linear superpositions of the circular excitons, distinguished by a different phase with respect to each other:

$$\begin{aligned} |x\rangle &= \frac{1}{\sqrt{2}}(|+\rangle + |-\rangle) \\ |y\rangle &= \frac{1}{i\sqrt{2}}(|+\rangle - |-\rangle)\,. \end{aligned} \tag{1.35}$$

In this picture, during the relaxation of the linear optical anisotropy, it is the phase between the coherent superpositions of the circular $|+\rangle$ and $|-\rangle$ states that dephases with a characteristic coherence time τ_R. Consequently, to be precise we should denote the time constants for the relaxations of the circular and linear anisotropies as T_1 and T_2, respectively, since the former can be understood as a population relaxation and the latter as a dephasing process. However, as we shall see later, the time constant determining the coherent electronic processes is the same for both anisotropies since the dominating contribution to the relaxation of the respective coherent superpositions of the excited states originates from the strong on-site Coulomb interactions of the Mott insulator in either case.

1.2.4 Density Matrix Formalism

Finding the dielectric function ϵ or alternatively the dielectric susceptibility χ of a material system gives complete knowledge about its optical properties. Both quantities are closely connected to a macroscopic polarization $P(t)$. In order to calculate $P(t)$, one should approach the problem on a quantum mechanical basis, especially when studying ultrafast light-matter interactions with the material's electron system. For a quantum mechanical system that is known to be in state s, the expectation value for the polarization and, in fact, any observable quantity A of that system is given by

$$\langle A\rangle = \langle s|\,\hat{A}\,|s\rangle\,, \tag{1.36}$$

where $|s\rangle$ denotes the wave function of state s and $\hat{A}$ is the corresponding Hermitian operator to the respective observable (see, e.g., Boyd [2008]). $|s\rangle$ is obtained by the well known time dependent Schrödinger equation

$$i\hbar\frac{\partial}{\partial t}\,|s\rangle = \hat{H}\,|s\rangle\,, \tag{1.37}$$

with the system's Hamilton operator $\hat{H}$. Since the eigenfunctions $|n\rangle$ to the eigenvalues E_n of the unperturbed Hamiltonian $\hat{H}_0$ form a complete set of basis functions, $|s\rangle$ can be expressed as

$$|s\rangle = \sum_n C_n^s(t)\,|n\rangle\,, \tag{1.38}$$

where the expansion coefficients C_n^s give the time dependent probability amplitudes[9] that the state s is identical to the eigenstate n. Substituting equation 1.38 into equation 1.36 yields the expectation value of the observable A in terms of the probability amplitudes C_n^s

$$\langle A\rangle = \sum_{mn} C_m^{s*} C_n^s A_{mn}, \tag{1.39}$$

where A_{mn} is the matrix element of the quantum mechanical operator $\hat{A}$ between the unperturbed eigenstates of the system

$$A_{mn} = \langle m|\,\hat{A}\,|n\rangle\,. \tag{1.40}$$

---

[9] Probability amplitudes, not probabilities. The latter would be the square of the absolute values of the amplitudes.

However, due to collisions and interactions of the atoms of a realistic physical system, one cannot know for a certainty that the system is in a particular state s but instead can only give certain probabilities $p(s)$. In that case, equation 1.39 has to be averaged not only over the eigenstates $|n\rangle$ but also over all possible states s weighted with the respective probabilities $p(s)$, which will be denoted by the overbar:

$$\overline{\langle A\rangle} = \sum_s p(s) \sum_{nm} C_m^{s*} C_n^s A_{mn}. \tag{1.41}$$

This expression can be simplified by defining the density matrix $\hat{\rho}$ as

$$\rho_{nm} = \sum_s p(s) C_m^{s*} C_n^s = \overline{C_m^{s*} C_n^s}. \tag{1.42}$$

While the diagonal elements of the density matrix ρ_{nn} give the probability that the system is in eigenstate n, the non-diagonal elements are only different from zero if the system is in a coherent superposition of the eigenstates n and m. Hence, these elements are related to the coherence of the system and are in certain circumstances proportional to the electric dipole moment. Using equation 1.42, we can rewrite equation 1.41 in order to express the expectation value of the observable A in terms of the trace of the product of $\hat{A}$ with the density matrix:

$$\overline{\langle A\rangle} = \sum_{nm} \rho_{nm} A_{mn} = \mathrm{tr}(\hat{\rho}\hat{A}). \tag{1.43}$$

Once the density matrix is known, the expectation value of any observable quantity can be calculated. $\dot{\hat{\rho}}$ is obtained by direct time differentiation of equation 1.42, where the time evolution of the probability densities C_n^s are evaluated by means of the Schrödinger equation, which yields

$$\begin{aligned}
\dot{\rho}_{nm} &= \sum_s \frac{dp(s)}{dt} C_m^{s*} C_n^s + \sum_s p(s) \left(C_m^{s*} \frac{dC_n^s}{dt} + \frac{dC_m^{s*}}{dt} C_n^s \right) \\
&\approx \frac{-i}{\hbar} [\hat{H}, \hat{\rho}]_{nm},
\end{aligned} \tag{1.44}$$

where $[..., ...]$ denotes a quantum mechanical commutator and $dp(s)/dt$ has been assumed to be negligible. However, since collisions and interactions within the system under consideration can change its state, the last assumption is not necessarily valid. This problem is considered by adding phenomenological damping terms $\hat{R}$ to equation 1.44 including (additional) population decay and dephasing terms, respectively, due to dissipation:

$$i\hbar\dot{\rho}_{nm} = [\hat{H}, \hat{\rho}]_{nm} + \hat{R}. \tag{1.45}$$

The system of ordinary differential equations 1.45, whose solution leads to the density matrix, is usually referred to as the Liouville-von Neumann equation [Meier et al., 2007].

As an example, for a three-level system with a non-degenerate ground state $|g\rangle$ and a doubly degenerate excited state $|x, y\rangle$ perturbed by femtosecond optical pulses in a pump-probe experiment (see figure 4.1b), equation 1.45 gives in the rotating wave approximation:

$$\begin{aligned}
\dot{\sigma}_{xg} &= \sigma_{xg} \left[i\Delta - \frac{1}{t_2} \right] - i\frac{\Omega_R}{2} e^{-t^2/\sigma^2} (1 - 2\rho_{xx} - \rho_{yy}) \\
\dot{\rho}_{xx} &= -\frac{i}{2} \left(\Omega_R \sigma_{xg} - \Omega_R \sigma_{xg}^* \right) e^{-t^2/\sigma^2} + \frac{\rho_{yy} - \rho_{xx}}{\tau_R} - \frac{\rho_{xx}}{t_1} \\
\dot{\rho}_{yy} &= \frac{\rho_{xx} - \rho_{yy}}{\tau_R} - \frac{\rho_{yy}}{t_1}.
\end{aligned} \tag{1.46}$$

Here, the σ are connected to the non-diagonal elements of $\hat{\rho}$ and the Hamiltonian $\hat{H} = \hat{H}_0 + \hat{V}$ has been assumed to include only the electric dipole perturbation $\hat{V}_{ij} = -\hat{\mu}_{ij}\widetilde{E}_j(t)$ with the electric field $\widetilde{\boldsymbol{E}}$ polarized in the x-direction ($\hat{\mu} = e\hat{x}$ and $\mu := \mu_{xg} = \mu_{gx}$). The latter is real and has a Gaussian envelope $E(t) = E_0 \exp(-t^2/\sigma^2)$ with $t_D = \sqrt{2\ln 2}\sigma$. Accordingly, the Rabi frequency is defined by $\hbar\Omega_R = 2\mu E_0$. $\Delta = \omega - \omega_0$ is the detuning of the optical frequency from the resonance, t_1 is the population relaxation time, t_2 is the dipole dephasing time and τ_R is the relaxation time between levels $|x\rangle$ and $|y\rangle$. This set of coupled differential equations can be easily solved numerically for arbitrary pulse durations t_D. However, due to the simple form of the Hamilton operator, this approach does not include any kind of electron-electron interactions. The solution of the Liouville-van Neumann equation with the full Hamiltonian of a complex strongly correlated system such as YMnO$_3$ is beyond the scope of this thesis. In order to model experimental data, approximations are required, which will be introduced in section 4.1.2.

1.3 Non-Thermal Optical Control of Magnetization

1.3.1 The Inverse Faraday Effect

Upon propagation through a magnetic material, linearly polarized light may experience a rotation of its plane of polarization. The rotation angle is proportional to the projection of the material's spontaneous magnetization onto the direction of light propagation. This effect is known as the Faraday effect [Hecht and Zajac, 2003]. But also the inverse form of this effect is known, namely that light with a rotating electric field vector, e.g., circularly polarized light, can induce a magnetization inside the medium, which must not necessarily be magnetic at all. This is usually referred to as the inverse Faraday effect (IFE).

The IFE has been described quantitatively by Pershan [1963] from a thermodynamic consideration of a non-absorbing material in a DC or AC magnetic field H interacting with an electromagnetic wave $E(\omega)$. Under steady-state conditions, i.e., in thermodynamic equilibrium, the free energy F of this isothermal system reaches a minimum ($dF = 0$). Hence, the free energy is well suited as a thermodynamic potential, from which all remaining state variables, such as the polarization P and the magnetization M, can be derived from first derivatives of F with respect to the potential's natural variables:

$$\begin{aligned} P(\omega) &= -\partial F/\partial E^*(\omega) \\ M(0) &= -\partial F/\partial H(0). \end{aligned} \tag{1.47}$$

For our purposes, it is sufficient to consider only a static magnetic field $H(0)$ instead of the more general formulation.

For light propagating in the z-direction, materials exhibiting the inverse Faraday effect have a free energy of the form

$$F = -2\mathrm{Re}(\chi_{ijk} E_i^* E_j H_k), \tag{1.48}$$

where, χ is the dielectric susceptibility tensor and according to the Einstein summation convention, repeated indices have to be summed over. χ is determined by the symmetry of the crystal. If the material is non-magnetic, it is invariant under time-inversion and the elements of the dielectric susceptibility are purely imaginary. In this case, the light induced magnetization can be derived by means of equation 1.47 to be

$$M_z(0) = 2\chi^*_{ijk}[E_i E^*_j]. \tag{1.49}$$

The magnetization is only real if either one or the other component of the electric field is imaginary, as is the case for circularly polarized light. Obviously, the direction of magnetization will be opposite for left- and right-circularly polarized excitation. For linearly polarized light, on the other hand, $M_z(0) = 0$.

Iron garnets are highly transmissive for near-infrared radiation so that the above description is well applicable. The only restriction for the validity of equation 1.49 is time-inversion symmetry of the system. However, the IFE can be shown to be present also in cubic or isotropic materials, which lack time-inversion symmetry due to a spontaneous magnetization [Pershan, 1963].

With respect to ultrafast applications, it is interesting to consider the IFE for photo-excitation with laser pulses, which are much shorter than the thermalization times of the system, e.g., pulses with femtosecond temporal duration. Obviously, the assumption of thermodynamic equilibrium, which has been made above, fails in this situation. Nevertheless, the IFE also exists under these conditions (see, e.g., Hansteen et al. [2006]).

Since the IFE occurs in the transparent regime, all the light induced transitions are virtual. Therefore, it is not necessary to know the exact electronic transitions induced by photo-excitation nor special knowledge of the ground state of the material. Instead, one can understand the IFE within a phenomenological picture, which considers virtual transitions from an arbitrary ground state $|g\rangle$ (see, e.g., Kirilyuk et al. [2010]). The circularly polarized light selectively addresses spins with either up- or down-orientation depending on the nearest optically allowed excited state $|e\rangle$ and induces virtual transitions, thereby mixing the wave functions of the two states, i.e., the electron wave function will be a linear superposition of $|g\rangle$ and $|e\rangle$. If $|g\rangle$ is a singlet state with zero orbital momentum ($S = 0$), the virtual transition will transfer orbital momentum of $|e\rangle$ to the excited electron. The presence of a non-zero orbital momentum increases the probability of a spin-flip due to spin-orbit interaction, which can occur on timescales as fast as 20 fs depending on the strength of the coupling [Kahn et al., 1969]. Since there is no absorption in the transparent regime, the spin-flip occurs effectively in the ground state. The energy difference of the ground state electron before and after the spin-flip equals the energy of a magnon, i.e., the precession of the magnetic moment around an equilibrium direction, which is initiated in the medium due to the optical excitation and which propagates through it as a so-called spin-wave.

1.3.2 The Landau-Lifshitz-Gilbert Equation

For simplicity, only the intrinsic angular momentum of the electron, i.e., the electron spin $\boldsymbol{S}(t)$ shall be considered here at first. The precession of $\boldsymbol{S}(t)$ in an external magnetic field $\boldsymbol{B}$ is usually described quantitatively by the equation of motion for the expectation value of quantum mechanical operators [Cohen-Tannoudji, 1999]

$$\frac{d}{dt}\langle \boldsymbol{S}\rangle(t) = \langle[\boldsymbol{S}, \boldsymbol{H}_{SB}(t)]\rangle, \tag{1.50}$$

where $\boldsymbol{H}_{SB}(t) = -\gamma_S \boldsymbol{S}\boldsymbol{B}(t)$ is the Zeeman term of the Hamiltonian of the system, $\gamma_S = g_S\mu_B/\hbar$, g_S is the gyromagnetic ratio of the spin and μ_B is the Bohr magneton.

Inside the medium, the magnetic field reads

$$\boldsymbol{B}(t) = \mu_0(\boldsymbol{H}_{\text{eff}}(t) + \boldsymbol{M}(t)), \tag{1.51}$$

where μ_0 is the vacuum permeability and $\boldsymbol{M}(t)$ is the magnetic moment per unit volume or magnetization.[10] $\boldsymbol{H}_{\text{eff}}(t)$ is the effective magnetic field, which combines all field contributions to $\boldsymbol{B}$ inside the medium [Hansteen et al., 2006]

$$\boldsymbol{H}_{\text{eff}}(t) = \boldsymbol{H}_{\text{a}}(t) + \boldsymbol{H}_{\text{ext}} + \boldsymbol{H}_{\text{dem}}, \tag{1.52}$$

where $\boldsymbol{H}_{\text{a}}(t)$ is the anisotropy field, which depends on the crystal structure and symmetry and determines the magnetic anisotropy of the material, i.e., the direction of the spontaneous magnetization. $\boldsymbol{H}_{\text{ext}}$ is the externally applied field and $\boldsymbol{H}_{\text{dem}}$ is the demagnetization field. The latter originates from a divergence in the magnetization $\nabla\boldsymbol{M} = -\nabla\boldsymbol{H}_{\text{dem}}$ of the sample at its surface since $\nabla\boldsymbol{B} = 0$ [Blundell, 2001].

The electron spin is connected to a magnetic moment $\boldsymbol{\mu_S}(t) = \gamma_S\boldsymbol{S}(t)$. Substituting this and $\boldsymbol{H}_{SB}(t)$ into equation 1.50 and using the angular momentum commutation relations, one can rewrite the commutator to arrive at the following expression for the optically induced spin dynamics, which is commonly referred to as the Landau-Lifshitz-Gilbert equation:

$$\frac{d}{dt}\langle\boldsymbol{\mu_S}\rangle(t) = \gamma_S\langle\boldsymbol{\mu_S}\rangle(t) \times \boldsymbol{B}(t). \tag{1.53}$$

Equation 1.53 states that the magnetic moment $\boldsymbol{\mu_S}$ of the electron spin will precess around the effective magnetic field $\boldsymbol{H}_{\text{eff}}(t)$, which is itself time dependent. In equilibrium, $\boldsymbol{\mu_S}$ is parallel to $\boldsymbol{H}_{\text{eff}}$. In general, there is not only the spin part of the magnetic moment but also the orbital part $\boldsymbol{\mu_L}$ originating from the movement of the electrons around the nuclei. It can be shown that equation 1.53 is valid for an arbitrary magnetic moment so that $\boldsymbol{\mu_S}$ can be substituted for by the total magnetic moment $\boldsymbol{\mu} = \boldsymbol{\mu_L} + \boldsymbol{\mu_S}$ or (normalized to the unit volume) by the magnetization $\boldsymbol{M}$:

$$\frac{d}{dt}\langle\boldsymbol{M}\rangle(t) = \gamma\langle\boldsymbol{M}\rangle(t) \times \boldsymbol{B}(t), \tag{1.54}$$

where now $\gamma = g\mu_B/\hbar$ and $g = g_S + g_L$. Consequently, we will talk about a precession of the magnetization instead of only considering the spin precession in the remainder of the text.

In our experiments, only $\boldsymbol{H}_{\text{a}}$ and/or $\boldsymbol{M}$ are modified by the optical excitation and experience ultrafast changes. The other components of $\boldsymbol{H}_{\text{eff}}$ can be considered constant in time. Since the induced optical perturbations are in the optical or near-infrared frequency range, they exclusively act on the material's electron system, whose equilibration can occur on sub-picosecond time scales (as will be shown, e.g., in chapters 3 and 4) and therefore holds potential for ultrafast all-optical applications.

---

[10] Note that the microscopic magnetic moment corresponding to $\boldsymbol{M}$ is the sum of the orbital and spin parts $\mu = \mu_L + \mu_S$.

Chapter 2

Experimental Methods

There are several common experimental approaches to monitor ultrafast light-matter interactions in semiconductors and metals, such as four-wave-mixing (FWM) spectroscopy, time-resolved photoluminescence spectroscopy (TRPL) or interferometric techniques. One of the best known methods, which is also exploited in this work, is the degenerate pump-probe spectroscopy, where a train of excitation (pump) pulses induces a change in the optical properties of a sample, which is then subsequently tested by a second train of less intensive (probe) pulses of equal wavelength by means of, e.g., changes in the reflectivity, transmissivity or polarization of the probe light. A temporal resolution is established by continuous variation of the arrival time of the probe pulses at the sample with respect to the corresponding pump pulses. The difference in the arrival times is the so-called pump-probe delay time. The time resolution is only limited by the duration of the pulses, respectively the width of the cross-correlation function. Since the development of femtosecond lasers, linear and nonlinear processes considerably faster than the electron-phonon relaxation time or even electron-electron scattering times can be investigated, the former being typically on the order of 1 ps [Sun et al., 1994]. Moreover, femtosecond lasers have proved to be of crucial importance for new approaches to implement coherent control of electronic states in matter [Kirilyuk et al., 2010; Ramsay, 2010; Zhang et al., 2011], from which a variety of research fields could profit, among these information processing, optoelectronics [Kamiya, 1999], spintronics [Žutić et al., 2004], biology and medicine [Sibbett et al., 2012]. After excitation of a semiconductor or metal with a femtosecond laser pulse, the electron system is in a non-thermal state, which cannot be described by a well defined electron distribution function. Only after the femtosecond excitation, this electronic state thermalizes, e.g., via the lattice. Femtosecond pump-probe spectroscopy therefore provides an excellent tool for the observation of ultrafast carrier/spin relaxation and dephasing mechanisms while the physics of non-thermal electron systems potentially holds interesting and new optical phenomena.

In this chapter, the main features of the experimental femtosecond setup will be described (section 2.1). These can be roughly divided into four parts, covering the laser system and pulse shaping (section 2.1.2), signal modulation and frequency sensitive detection (section 2.1.3), pulse polarization and focusing (section 2.1.4), and finally signal detection schemes (section 2.1.5). Further, a white light setup will be explained in section 2.2, which is used for broadband sample characterization and spectrally resolved, time-integrated magneto-optical measurements.

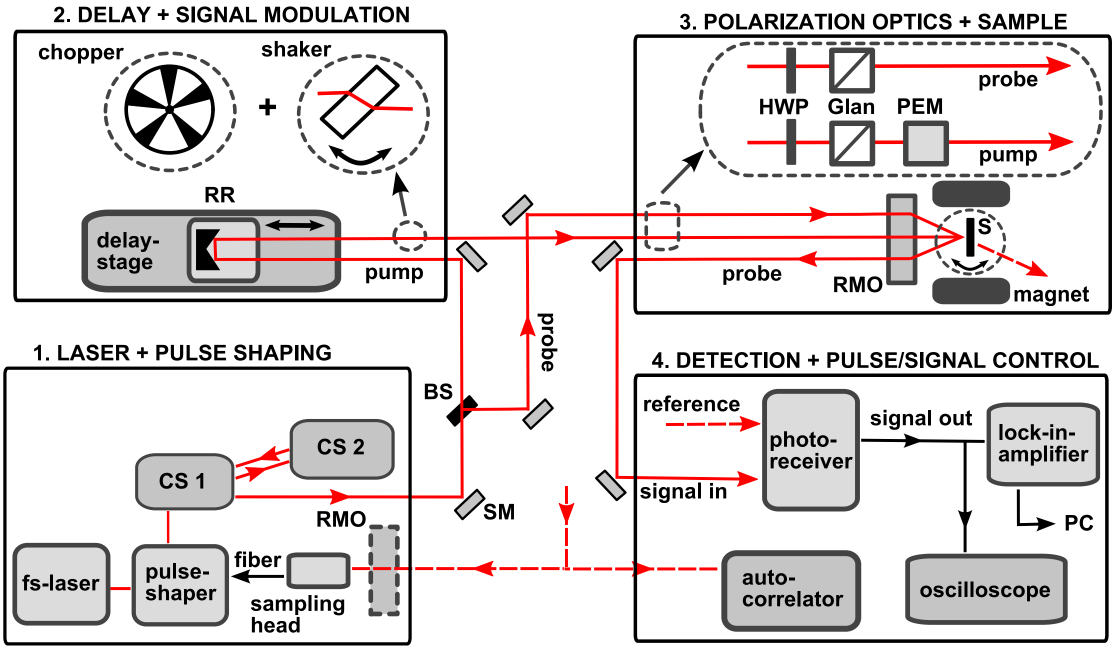

Figure 2.1: Schematic illustration of the experimental femtosecond pump-probe setup. RMO: Reflective microscope objective. CS: Compressor stage. SM: Silver mirror. BS: Beam splitter. RR: Retro-reflector. HWP: Half-wave plate. Glan: Glan-Thompson prism. PEM: Photo-elastic modulator. S: Sample.

2.1 Femtosecond Pump-Probe Technique

Figure 2.1 gives the schematic overview of the experimental setup. While the principle design will be given here, the reader is referred to the subsequent sections for details.

Pulses of several hundreds of femtoseconds are provided by a broadband ultrafast titanium sapphire (TiSa) oscillator at a repetition frequency around 80 MHz. The spectral widths of the pulses were typically in the range between 60 and 90 nm with a center wavelength around 800 nm. After passing through the shaper and compressor unit, which modify the pulse shape and phase, a 90:10 beam splitter divides the laser beam into pump and probe beams. The former is redirected to the delay line, which consists of a retro-reflector positioned on a linear translation stage with an accuracy better than $1\,\mu\mathrm{m} \equiv 6.67\,\mathrm{fs}$. The length of the delay line gives a maximum temporal delay between each pump and probe pulse of 1 ns.

Wave retarders and Glan-Thompson prisms set the polarization appropriate to the respective experiment and the beams are focused onto the sample, which is positioned on a rotation holder between two coils of an electromagnet oriented in Voigt geometry. Here, due to the pulse shaping units, standard temporal pulse widths are close to 20 fs. The maximum available magnetic field is $B = 400\,\mathrm{mT}$. Optionally, the sample can be mounted into a liquid helium flow cryostat in order to perform experiments at cryogenic temperatures but at zero magnetic field. In figure 2.1 the setup is shown for reflection geometry, meaning that the reflected probe beam is redirected into the detection channel but it is straightforward to use the setup in transmission geometry as well as indicated by the dashed arrow behind the sample.

In either case, the beam is focused onto the signal diode of a balanced photoreceiver, which works as a differential amplifier. Its reference input can either be a part of the initial laser beam or one polarization component of the probe beam. In both cases, the differential amplifier cancels noise signals that are common to both channels, e.g., laser-intensity noise or pump scattered light, reducing experimental noise levels to the usual electronic shot noise.

The difference signal is passed to an oscilloscope for monitoring and to the main detector unit, a lock-in amplifier, which processes the output. It is read out and controlled via computer. Further, the pump beam can be outcoupled and passed to an auto-correlator unit in order to control temporal width and shape of the pulses incident on the sample.

2.1.1 The Optical Response in Pump-Probe Experiments

In order to process and understand time-resolved pump-probe signals appropriately, one in principle has to derive a microscopic expression for the respective density matrix elements by means of solving the Liouville-von Neumann equation 1.45 with the Hamiltonian of the system under consideration. However, a phenomenological expression can be obtained much easier using linear response theory. In terms of this approach, the time dependent response $R(t)$ of the system depends on all previous values of the so-called input function, i.e., the perturbation of this system, which in our case is proportional to the Gaussian intensity of the excitation (pp) pulse $I_{pp}(t)$, i.e.,

$$R(t) \approx \int_{-\infty}^{t} r(t-x) I_{pp}(x) dx, \tag{2.1}$$

where $r(t)$ is the impulse response function, which gives the characteristic response of the system for a Dirac-delta function input $\delta(x)$. In a femtosecond pump-probe experiment, the ultrafast signal $S(\tau)$ at a specific time (delay) τ measured by the (slow) photodiode is a convolution of the response $R(t)$ with a gate function (or window function, see Saleh and Teich [2007]), which corresponds to the intensity of the test (pr) pulse $I_{pr}(t)$, which again has a Gaussian profile. The integration limits correspond to the temporal extend of the window function, i.e., the probe pulse, over which the photodetector integrates. Since the detected intensity is zero at all other times, the integration limits can be set to infinity without loss of generality:

$$S(\tau) = \int_{-\infty}^{\infty} I_{pr}(\tau - t) R(t) dt. \tag{2.2}$$

Substituting equation 2.1 for $R(t)$ yields

$$\begin{aligned} S(\tau) &= \int_{-\infty}^{\infty} I_{pr}(\tau - t) \left(\int_{-\infty}^{t} r(t-x) I_{pp}(x) dx \right) dt \\ &= \int_{-\infty}^{\infty} I_{pr}(\tau - t) \left(\int_{-\infty}^{t} I_{pp}(t-x) r(x) dx \right) dt \\ &= \int_{-\infty}^{t} r(x) \left(\int_{-\infty}^{\infty} I_{pp}(t-x) I_{pr}(\tau - t) dt \right) dx \\ &= \int_{-\infty}^{\tau} r(x) \left(\int_{-\infty}^{\infty} I_{pp}((\tau - x) - y) I_{pr}(y) dy \right) dx, \end{aligned} \tag{2.3}$$

where the order of integration has been changed in between and the substitution $y := \tau - t$ has been applied in the last step. The expression in brackets in equation 2.3 is a convolution of two Gaussians, which corresponds to the cross-correlation $G(\tau - x)$ of pump and probe pulses. Assuming $I_{pp}(\nu)$ and $I_{pr}(\nu)$ to be the Fourier transforms of $I_{pp}(t)$ and $I_{pr}(t)$, the following expression holds (product rule):

$$G(\tau - x) = (I_{pp} * I_{pr})(t) = \mathcal{F}\{I_{pp}(\nu) \cdot I_{pr}(\nu)\}. \tag{2.4}$$

The inverse Fourier transform will again have a Gaussian shape with FWHM of $\sqrt{2}\tau_D$ for identical pump and probe pulses.

The studied system may not only have one simple impulse response but $r(t)$ must rather be written as $r(t) = \sum_i r_i(t)$. In this case, we find that the signal is also a sum with the summands being convolutions of the pump-probe cross-correlation with the different components $r_i(t)$ of the system response

$$\begin{aligned} S(\tau) &= \int_{-\infty}^{\tau} r(x) G(\tau - x) dx \\ &= G * \sum_i r_i = \sum_i (G * r_i). \end{aligned} \tag{2.5}$$

Most frequently, the instantaneous response function is taken to be either instantaneous, i.e, a Dirac-delta function or a single exponential with a specific relaxation time. Performing the respective convolution in the former case is straightforward and results in a signal contribution

$$S_\delta(t) \propto \exp -(t/\sigma)^2, \tag{2.6}$$

where $\tau_D = \sqrt{2 \ln 2}\sigma$. For a single exponential with relaxation time τ_j, the convolution is more difficult and hence will be sketched in more detail in the following. According to equation 2.5, the respective signal contribution can be written as[1] ($G(t) = \exp(-t^2/\sigma^2)$)

$$\begin{aligned} S_j(t) &= \int_{-\infty}^{t} \exp\left(-\frac{t - t'}{\tau_j}\right) \exp\left(-\frac{t'^2}{\sigma^2}\right) dt' \\ &= e^{-t/\tau_j} \int_{-\infty}^{t} \exp -\left(\frac{t'^2}{\sigma^2} - \frac{t'}{\tau_j}\right) dt' \\ &= e^{-t/\tau_j} \int_{-\infty}^{t} \exp -\left(a^2 t'^2 + 2abt' + b^2 - b^2\right) dt'. \end{aligned}$$

In the last step, the substitutions $a := 1/\sigma$ and $b := -\sigma/(2\tau_j)$ have been inserted. This can be simplified to

$$S_j(t) = e^{-t/\tau_j} \int_{-\infty}^{t} \exp\left(-(at' + b)^2 + b^2\right) dt'.$$

Performing another substitution $z := at' + b$, we arrive at

$$\begin{aligned} S_j(t) &= \sigma \exp\left(\frac{\sigma^2}{4\tau_j^2} - \frac{t}{\tau_j}\right) \int_{-\infty}^{at+b} e^{-z^2} dz \\ &= \sigma \exp\left(\frac{\sigma^2}{4\tau_j^2} - \frac{t}{\tau_j}\right) \left[\int_{-\infty}^{\infty} e^{-z^2} dz - \int_{at+b}^{\infty} e^{-z^2} dz\right]. \end{aligned}$$

---

[1] The time delay τ from equation 2.5 is now changed to t so it is not confused with the relaxation time τ_j.

The integral $\int_0^\infty \exp(-z^2)dz = \sqrt{\pi}/2$ is a popular example of complex analysis to be solved with the residue theorem. With this identity it can be seen that the integral on the left hand side gives $2\sqrt{\pi}/2 = \pi$ since the integrand is an even function. The integral on the right hand side can be separated as well into a part going from 0 to ∞ and one from 0 to $(at + b)$. The latter is per definition identical to the Gaussian error function $\mathrm{erf}(x) = 2/\sqrt{\pi} \int_0^x \exp(-z^2)dz$, which brings us to the final result

$$\begin{aligned} S_j(t) &= \sigma \exp\left(\frac{\sigma^2}{4\tau_j^2} - \frac{t}{\tau_j}\right) \left[2\frac{\sqrt{\pi}}{2} - (\frac{\sqrt{\pi}}{2} - \frac{\sqrt{\pi}}{2}\mathrm{erf}(at + b))\right] \\ &= \sigma\frac{\sqrt{\pi}}{2} \exp\left(\frac{\sigma^2}{4\tau_j^2} - \frac{t}{\tau_j}\right) \left[1 + \mathrm{erf}\left(\frac{t}{\sigma} - \frac{\sigma}{2\tau_j}\right)\right]. \end{aligned} \tag{2.7}$$

For relaxation times τ_j much longer than the experimentally accessible time range t, this expression simplifies to

$$S_j(t) = \sigma\frac{\sqrt{\pi}}{2} \left[1 + \mathrm{erf}\left(\frac{t}{\sigma}\right)\right]. \tag{2.8}$$

2.1.2 Compression and Phase Shaping of Broadband Laser Pulses

The electric field of an EM wave can be written in the time domain as $U(t) = A(t)\exp(i\omega_0 t)$, with the complex envelope $A(t)$ and central frequency $\omega_0 = 2\pi\nu_0$. For ultrashort pulses, the corresponding spectral intensity $S(\nu) = |\int U(t)\exp(-i2\pi\nu t)dt|^2$ is a broad function in the frequency domain. The pulses travel with a group velocity $v = 1/(d\beta/d\omega)$, which itself is frequency dependent, since the propagation constant reads $\beta = \omega n(\omega)/c_0$ (n: refractive index, c_0: vacuum speed of light). Consequently, when traversing a dispersive medium, such as polarizers, lenses or any other kind of optical elements, different frequency components will experience different retardations of the spectral phase $d\varphi(\omega)$. Hence, each spectral component undergoes different temporal delays and the pulses spread in time. Higher (lower) frequency components arrive earlier than lower (higher) frequency components, which is referred to as anomalous (normal) group velocity dispersion (GVD). In this case, their instantaneous angular frequency $\omega_i = \omega_0 + d\varphi/dt$ is not a constant but becomes a function of time and the pulse is said to be chirped (see, e.g., Saleh and Teich [2007] and figure 2.2). Since most elements in the setup cause a normal dispersion, a compressor stage is used to provide a fixed anomalous (or negative) GVD in order to cancel most of the linear chirp, which is yet to come from the subsequent dispersive materials (see figure 2.1). This negative GVD is mainly determined by the distance between the prisms on the one hand and the amount of prism glass in the beam path during one roundtrip on the other hand. Effectively, this results in a wavelength dependent optical path length corresponding to anomalous dispersion.

The pulse shaper, which holds the key technology of the femtosecond setup, is able to correct the remaining spectral phase distortions by means of an iterative algorithm, the multi-photon intrapulse interference phase scan (MIIPS) method [Xu et al., 2006]. Inside the shaper, the beam is dispersed and passed onto the 128 pixels of a (nematic) spatial light modulator (SLM) array. The pixels are liquid crystals, which provide an electrically tunable index of refraction along their extraordinary axis. Both, phase and amplitude of the spectral components of the laser pulses can be modified independently in a reflective design. This design is realized by successively positioning one polarizer, two SLMs and a reflective mirror, where the optical axes of the SLMs are aligned at 90° with respect to each other and at 45° with respect to the polarizer.

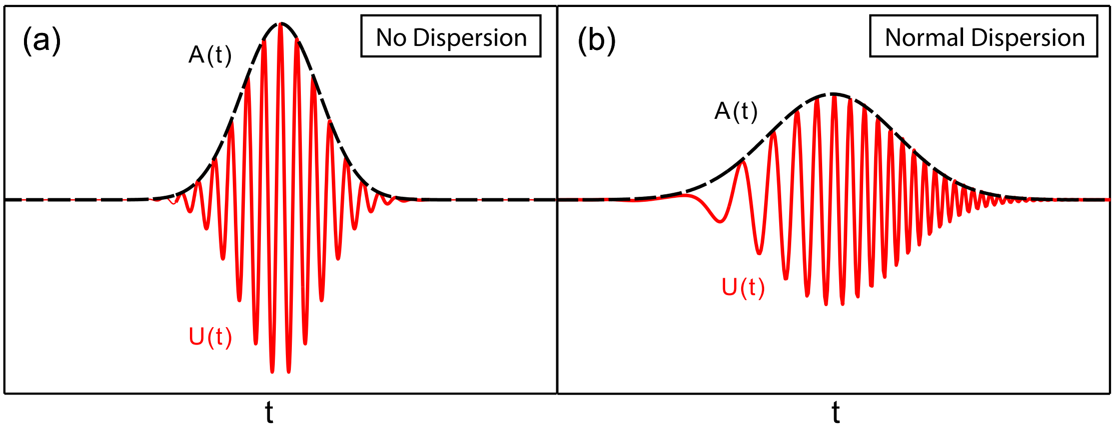

Figure 2.2: Computed Gaussian envelope function $A(t)$ (dashed line) and real part of the complex wave function $U(t)$ (solid line) in the time domain for (a) an unchirped laser pulse and (b) an up-chirped pulse (increasing instantaneous frequency) as resulting from normal dispersion. The low frequency components of the chirped pulse arrive earlier in time than the high frequency ones and it broadens in time at the cost of peak intensity with respect to the unchirped one.

The MIIPS method exploits the influence of the pulse's spectral phase on the second-harmonic intensity $S^{(2)}(2\omega)$ generated in a thin nonlinear crystal inside the sampling head (see figure 2.1). The light is outcoupled before the sample but after the last dispersive element in the setup and redirected to the sampling head, which produces a feedback for the pulse shaper by analyzing the incident pulses as will be explained in the following. At the position of the nonlinear crystal, the phase is composed of the unknown initial phase of the pulse $\phi(\omega)$ and a known phase $f(\omega)$ superimposed by the pulse shaper, so that $\varphi(\omega) = \phi(\omega) + f(\omega)$. $S^{(2)}(2\omega)$ is most importantly determined by an integral of a complex exponent of phase $\varphi(\omega+\Omega) + \varphi(\omega-\Omega)$ over all detunings Ω contributing to the SHG process. This term can be expanded into a Taylor series around ω:

$$\varphi(\omega+\Omega) + \varphi(\omega-\Omega) = 2\varphi(\omega) + \frac{d^2\varphi(\omega)}{d\omega^2}\Omega^2 + \ ... \ + \frac{2}{(2n)!}\frac{d^{2n}\varphi(\omega)}{d\omega^{2n}}\Omega^{2n}. \tag{2.9}$$

Neglecting higher order terms, this expression becomes independent of the integration variable Ω if $\varphi'' := d^2\varphi(\omega)/d\omega^2 = 0$ so that $S^{(2)}(2\omega)$ has a local maximum at ω due to elimination of the oscillatory component of the integrand. Since this implies $\phi''(\omega) = -f''(\omega)$, the unknown second order pulse phase $\phi''(\omega)$ can be compensated by systematically changing the superimposed phase $f''(\omega)$ so that $S^{(2)}(2\omega)$ is maximized. In this case,

$$f(\omega) = -\int\left(\int \phi''(\omega)d\omega\right)d\omega \tag{2.10}$$

gives the desired phase to be superimposed by the pulse shaper in order to achieve a transform limited (TL) pulse, i.e., with minimum possible pulse duration.

2.1.3 Frequency Sensitive Detection of Modulated Signals

Typically, changes of the optical properties of materials in pump-probe experiments are on the order of 10^{-2} or smaller. Moreover, these signals $s(t)$ are hidden among a multitude of contributions from various sources of noise $r(t)$ present in the laboratory.

The signal plus noise $f(t) = s(t) + r(t)$ can be decomposed into its frequency components as

$$f(t) = \frac{1}{\sqrt{2\pi}} \int_{-\infty}^{\infty} a(\omega) e^{-i\omega t + \varphi(\omega)} d\omega, \tag{2.11}$$

where the Fourier coefficients $a(\omega)$ can be retrieved via an inverse Fourier transformation. The idea of lock-in amplifier detection is to modulate the signal by, e.g., periodically chopping the pump light intensity (chopper, see figure 2.1) or its state of polarization (PEM) in order to have $s(t) = a_s \exp(i\omega_s t + \varphi_s)$ with the modulation frequency ω_s. Now, from all the frequencies of $f(t)$, we only need to consider ω_s and the corresponding Fourier amplitude $a(\omega_s)$ of equation 2.11. The latter can be obtained by multiplying $f(t)$ by an AC reference $s_{\mathrm{ref}}(t) = \exp(i\omega_s t - \varphi_s)$ of equal frequency and phase as the modulated signal and subsequent integration over time:

$$a(\omega_s) = \frac{1}{\sqrt{2\pi}} \int_{-\infty}^{\infty} f(t) e^{-i\omega_s t - \varphi_s} d\omega. \tag{2.12}$$

The multiplication is performed by the lock-in's phase sensitive detector (PSD) and the time integration is established by a low-pass filter, the integration time being determined by its cut-off frequency. Only if the reference frequency equals the signal frequency does the PSD output have a DC component, which gives an amplitude proportional to the signal amplitude a_s after integration. Additionally, the signal is multiplied by a reference of phase $\varphi_s + \pi/2$, resulting in a pure AC PSD output, which will be eliminated by the low-pass. Both outputs, referred to as X and Y channels, are used to determine the correct signal phase.

In summary, the modulation of the signal allows to filter a narrow range of frequencies around ω_s out of all the frequency components of $f(t)$ by means of a lock-in amplifier. Hence, all contributions of noise to the signal at frequencies different than ω_s are eliminated. That way, the sensitivity of the setup can reach 10^{-6} depending on certain experimental parameters and on ω_s.[2]

2.1.4 Excitation Polarization and Focusing

Wave retarders and Glan-Thompson prisms are used to align the beam polarizations for polarization sensitive measurements. Moreover, a photo-elastic modulator (PEM) can be applied for polarization modulation instead of intensity modulation by a chopper. Its two modes of operation are outlined in figure 2.3. The operation is based on a fused silica bar that is forced to vibrate at its resonance frequency of $f = 50\,\mathrm{kHz}$. The strain provided by a piezoelectric transducer induces an oscillating birefringence along the deformation axis of the crystal. Aligned at an angle of 45° with respect to the polarization of the laser, the PEM acts as a wave retarder with a dynamically variable phase retardation. The device is usually operated at retardations of $\lambda/4$ and $\lambda/2$ but can be operated in between as well. It should be mentioned that both, linear and circular signals, are present at their characteristic frequencies at all times. Only the strength of the corresponding modulation, and thus the signal strength, will be reversed when switching from $1f$ to $2f$ modulation or vice versa. Especially at retardations in between the two main modes, both, circularly and linearly induced signals, can be measured simultaneously at frequencies of $1f$ and $2f$, respectively, with approximately equal modulation strengths. This technique will become important in chapter 4.

---

[2] Most sources of noise in the laboratory are in the low frequency regime around $\omega_r \approx 10 - 100\,\mathrm{Hz}$. The efficiency of noise filtering by the lock-in detection increases with the difference $|\omega_s - \omega_r|$.

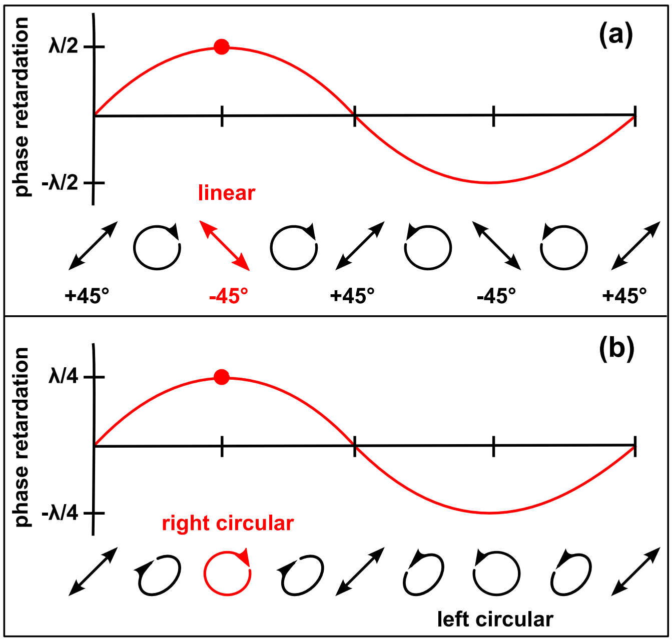

Figure 2.3: The two main modes of operation of the photo-elastic modulator. (a) The amplitude of phase retardation is $\lambda/2$ and the light polarization is modulated between two perpendicular states of linear polarization at a frequency of twice the resonance frequency ($2f$). (b) The retardation amplitude is only $\lambda/4$ and the light is modulated between left and right circularly polarized states. The periods of light modulation and crystal deformation are identical so the modulation frequency here equals the resonance frequency ($1f$).

After setting the light polarization, a 15x microscope objective is used to focus pump and probe beams to spots close to 15 μm and 10 μm, respectively. The larger pump spot provides an approximately homogeneous excitation area on the sample, which is subsequently tested by the probe beam. If the excitation area is inhomogeneous, fluctuations in the probe spot will lead to undesired fluctuations in the signal strength, i.e., signal noise. Since an objective usually contains a lot of glass, the corresponding chirp would be hard to compensate by the pulse shaper. Moreover, the use of glass lenses results in a "spatial" chirp, i.e., the amount of glass in the propagation direction of the beam depends on the perpendicular distance from the center of the lens. Both effects would destroy the previously formed pulse shape in the time as well as the spectral domain. Consequently, we make use of a reflective microscope objective (RMO), whose operation is based on two opposing spherical aluminum coated mirrors instead of lenses, which enables imaging with zero chromatic and negligible coma, spherical, and astigmatic aberrations.

Although the 80 MHz laser system provides excellent signal averaging due to the high pulse repetition rate, this goes at the cost of pulse energy, which is typically on the order of 1 nJ. Focusing to the mentioned micrometer sized laser spots gives a maximum pump fluence of 300 μJ/cm^2, increases spatial resolution, and enables investigations of nanoscale structures, whose dimensions are typically below 100 μm.

2.1.5 Signal Detection Techniques

Independent of the type of excitation, there are three different kinds of detection geometries used during the experiments. The most straightforward one is the measurement of the differential reflectivity or transmissivity. As mentioned earlier, in this case, the intensity on the signal input of the photoreceiver is balanced by an outcoupled portion of the laser beam before the beam splitter in order to cancel laser intensity noise. The other two methods are sensitive to rotations of the plane of polarization and the angle of ellipticity of an initially linearly polarized probe beam.

For detection of rotations, the probe beam coming from the sample is split into its polarization components via a Glan-Thompson prism. Each component is incident on one of the two inputs of the photoreceiver. A half-wave plate in front of the prism is used to balance the two intensities. Any rotation of the polarization plane by an angle α will now be translated into a rotation by 2α with respect to the fast axis of the half-wave plate. The rotation leads to an increase of the incident intensity on one of the detector diodes, which results in a lock-in amplified signal proportional to α.[3] On the other hand, optically induced changes of, e.g., the reflectivity or the ellipticity contribute equally to both channels and cancel each other.

Ellipticity measurements are similar to those for rotation. Only an additional quarter-wave plate is placed in front of the half-wave plate aligned with it's fast axis parallel to the incident unperturbed probe beam. Any rotation of the polarization plane will result in a fraction of the polarization along the slow axis of the quarter-wave plate giving circularly polarized light, which enters both channels equally and cancels out. Only an elliptically polarized probe pulse will be translated into linearly polarized light, which is rotated with respect to the balanced configuration of the half-wave plate. This rotation will contribute to only one of the two channels of the photoreceiver (as before) giving a lock-in amplified signal proportional to the ellipticity angle.[4]

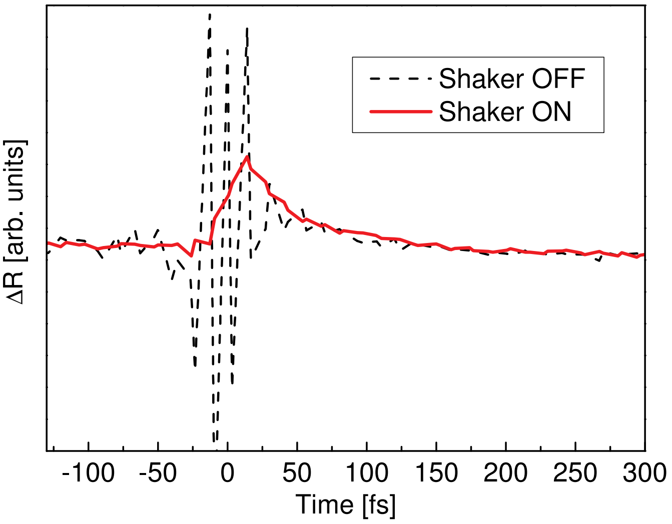

Figure 2.4: Exemplary demonstration of the effect of coherent artifact suppression by a galvanometer driven shaker. Shown is the differential reflectivity ΔR from a rough gold surface with (solid line) and without (dashed line) shaker operation. Although strong interference is observable within time scales of the pulses' cross-correlation, the shaker reveals a fast relaxation dynamic, which was previously inaccessible.

Unfortunately, in one-color experiments as described here, it is inevitable to have scattered light of the pump beam in the detection channel. Especially at short delays comparable to the pump-probe autocorrelation width, this leads to undesired interference fringes, referred to as "coherent artifact", which can mask the real signals. However, these interferences can be washed out by a rotating galvanometer driven glass plate placed at an angle θ in the pump beam path. The plate can be positioned with an angle resolution of $15\,\mu$rad in the range of $\pm 12.5^\circ$ and operated at frequencies up to 1 kHz due to closed-loop electronic positioning. The glass is highly transparent and optically homogeneous with a refractive index of $n = 1.525 \pm 0.001$. Upon propagation through the plate, the pump beam experiences a phase shift $\Delta\phi$ with respect to the probe beam due to the increased optical path length. This phase shift depends on the tilt θ as well

---

[3] Note that the lock-in amplifier measures a value, which corresponds to the amplitude, not the peak-to-peak value, of the modulated signal. While the peak-to-peak value would represent the rotation by 2α, the amplitude is proportional to the desired optically induced rotation angle α (in radians when normalized to the time averaged optical power incident on the detector).

[4] For the definition of the "ellipticity angle" see, e.g., Saleh and Teich [2007].

as the rotation amplitude $\pm\Delta\theta$ via

$$\Delta\phi(\theta,\Delta\theta) \approx \frac{2\pi}{\lambda_0} d \frac{n-1}{2n}((\theta+\Delta\theta)^2 - (\theta-\Delta\theta)^2), \tag{2.13}$$

where d is the thickness of the plate and λ_0 is the vacuum wavelength of light. The phase shift corresponds to a temporal delay τ via

$$\Delta\phi = k_0 L = \frac{2\pi}{\lambda_0}\frac{c_0}{n}\tau, \tag{2.14}$$

where c_0 is the vacuum speed of light and $\tau = \tau_0 \sin(\omega_\mathrm{m} t)$ with the modulation frequency ω_m. If the maximum optical path difference L_{max} between pump and probe beam, caused by this modulation, equals a multiple integer m of the center wavelength of the laser, i.e. $L_{max} = m\lambda_c$, the time averaged interference signal will be zero and the integration by the lock-in amplifier only passes the real signal intensity coming from the sample.

An example of the effect of the device's operation, which in the following will be referred to as "shaker", on the short time behavior of the differential reflectivity from a thin gold film with rough surface is demonstrated in figure 2.4. Its modulation frequency must be significantly different from the lock-in frequency and the maximum temporal delay must not exceed the pulse duration in order to maintain the temporal resolution of the setup.

2.2 White Light Spectroscopy

Apart from the time-resolved femtosecond setup, a white light setup with high spectral resolution is used for room-temperature broadband sample characterization and time-integrated investigations of magneto-optical effects, in particular the transverse magneto-optical Kerr effect (TMOKE). A schematic illustration of this setup is given in figure 2.5.

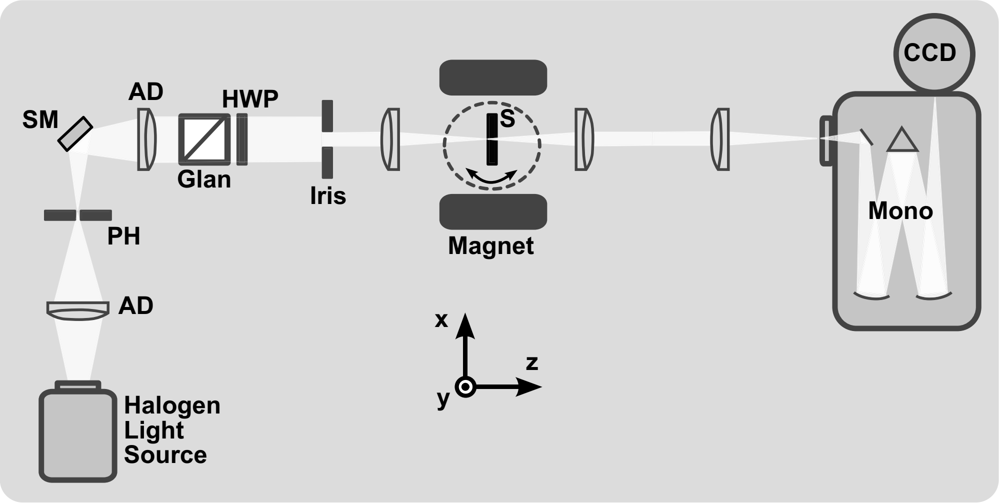

Figure 2.5: Schematic illustration of the experimental white light setup in transmission geometry. AD: Achromatic doublet lens. PH: Pinhole. SM: Silver mirror. HWP: Half-wave plate. Glan: Glan-Thompson prism. Iris: Iris diaphragm. S: Sample. Mono: Monochromator. CCD: Charge-coupled device.

An intensity tunable halogen lamp serves as the light source in these experiments providing near blackbody radiation with high stability better than 0.1 %. Achromatic doublet (AD) lenses are used to focus and collect light in different places within the setup in order to minimize chromatic abberations. The lamp's glow wire is imaged onto a 100 μm pinhole, which selects a homogeneous area of illumination in order to provide a near point type source of light for the subsequent optics. The emission from the pinhole is collimated by an achromatic doublet with focal length of $f_1 = 150$ mm or alternatively with $f_1 = 300$ mm. A Glan-Thompson prism in combination with a half-wave plate determines the excitation polarization. The light is focused onto the sample by another achromatic doublet with focal length $f_2 \leq f_1$ in order to achieve spot sizes between 50 μm and 300 μm depending on the dimensions of the structures under investigation. The sample is mounted on a rotation holder for angle resolved measurements. Rotation is possible in the xz- as well as the yz-plane. The diaphragm in front of the focusing lens limits the maximum angle of the incident light cone to below 1°, which determines the angular resolution of the setup. A water-cooled electro-magnet delivers magnetic fields up to 700 mT depending on the distance between its ferrites. The field direction can be switched in positive and negative direction on the x-axis. Both, magnet and monochromator operation, are implemented and controlled via software.

The setup can be used in transmission or reflection geometry. In either case, the light is collimated and focused onto the entrance slit of a single monochromator (linear dispersion 6.5 nm/mm at $\lambda = 500$ nm) after the sample and detected with a liquid nitrogen cooled charge -coupled device (CCD) camera. The overall spectral resolution of the setup is below 0.5 nm.

Chapter 3

Magneto-Plasmons and Ultrafast Plasmonics

SPPs are surface modes at the interface between a conductor and a dielectric. The electrons of the conductor perform coherent oscillations, which couple to the electromagnetic field of light under certain conditions (see section 1.1). The concept of SPPs has not been invented until the beginning of the 20th century. Wood [1902] discovered that the spectrum of white light reflected from a metallic diffraction grating shows sharp resonances for certain photon energies depending on the angle of incidence and the polarization. The resonances vanished at normal incidence and required a light polarization perpendicular to the ruling of the grating. Later, Fano [1961] delivered the theoretical description for these resonances after analyzing energy loss spectra of inelastic scattering of electrons by helium. He observed asymmetrically shaped resonances (Fano resonances, see section 1.1.3) and concluded that they originate from interference effects between two energetically degenerate electronic states. Both of these states are continuum states, only one transition channel is direct while the other channel involves resonant excitation to a discrete intermediate state.[1] Above the resonance energy, the resonantly excited electron wave function experiences a phase shift of π so that it is out of phase with the non-resonantly excited electron wave function, which leads to destructive quantum interference [Miroshnichenko et al., 2010]. The connection of the Wood anomalies with the excitation of surface plasmon modes was first established by Ritchie et al. [1968] who performed extensive polarization and angle dependent measurements of the intensity of white light diffracted from gold and aluminum gratings. The mathematical description of these surface waves had already been delivered by Sommerfeld [1899] when he investigated the propagation and damping of radio waves along wires of copper and platinum.

As mentioned before, SPPs can be utilized to enhance light-matter interactions and concentrate optical energy to nanometer volumes. In this chapter, we present experimental results of plasmonic enhancement with a view to possible application of the acquired knowledge for the fabrication of nanometer sized, ultrafast light modulators. Modulators represent a type of element, which is essential for signal processing and transfer, while the possibilities of optical control are versatile. One of the most recognized approaches is a plasmonic device with a 200 fs response time developed by MacDonald et al. [2009], who modulated the intensity of a signal beam, which was coupled and decoupled to a 5 μm aluminum/fused silica plasmonic waveguide via sub-wavelength gratings. The modulation strength of 7.5 % could be acomplished via a second control pulse incident on the

---

[1] in this case the (2s2p)^{1}P autoionized transition of helium, see Madden and Codling [1963]

waveguide between the two coupling gratings with relatively high pulse fluences around $10\,\mathrm{mJ/cm^2}$. The device's response time is claimed to be limited only by the momentum and energy relaxation time of electrons excited via interband transitions, which transiently change the metal's optical properties. Another approach turns to the realization of wavelength shifters exploiting the interaction of plasmons and longitudinal-optical (LO) phonons in a two-dimensional electron gas (2DEG) of a GaAs quantum well (QW) (see Pacifici [2007] and references therein).[2] Wavelength shifts occur via Raman scattering from the coupled plasmon-phonon modes, whose energy is proportional to the carrier density in the QW. The design utilizes a charge carrier separation to eliminate recombination losses and enable high densities, while the latter is determined by the intensity of a relatively weak optical control beam. Shifts in the optical frequency of 0.7 THz could be achieved at 160 K. An example of magneto-optical control of the light modulation has been provided by Temnov et al. [2010] in a hybrid metal-ferromagnet-metal multilayer sample in a slit-groove microinterferometric experiment. Here, the plasmon wavevector of a surface-magneto-plasmon traveling from a groove at the metal-ferromagnet interface to an outcoupling slit depends on the magnetization direction inside the magnetic layer. The light scattered by the plasmon at the slit interferes with directly transmitted light, resulting in interference fringes with respect to the slit-groove distance. Depending on the field of an external magnet, the interference fringes are phase-shifted, resulting in a nonzero difference signal, if the magnetization is reversed. That way, intensity modulations of 1 % at comparatively low magnetic fields of 20 mT could be obtained.

However, of the previous examples, only the approach of Fluegel et al. [2007] is a true nanometer, on-chip capable device, lacking modulation speed, while the situation is reversed in the rest of the examples. Combining high modulation speed with nanometer scale device dimensions and power-efficiency at preferably room-temperature remains a challenging subject until today. In this chapter, two different plasmon enhanced mechanisms will be presented as an attempt to fulfill these requirements. Section 3.1 focuses on the transverse magneto-optical Kerr effect (TMOKE). Basic theoretical aspects and experimental results obtained with magneto-plasmonic heterostructures will be explained and discussed. It will be shown that, in combination with femtosecond magnetization control, this effect promises to be a diverse tool for all-optical ultrafast intensity modulation. Subsequently, section 3.2 presents a different approach, which exploits transient SPP-induced changes in the optical properties of noble metals.

3.1 The Transverse Magneto-Optical Kerr Effect

It is well known that a magnetized medium can alter the properties of light passing through it, such as its amplitude, phase and polarization [Inoue et al., 2009; Zvezdin and Kotov, 1997]. Yet, only recently it could be shown that these magneto-optical (MO) processes can be controlled optically on sub-nanosecond time scales (see, e.g, Kirilyuk et al. [2010] and references therein), which is a promising prospect for modern optical devices and underlines the importance of MO effects in this field.

In this section, we concentrate on the transverse type of the magneto-optical Kerr effects, which allows the investigation of a medium's magnetic properties and is nowadays used in magnetic data storage [Mansuripur, 1998; Zvezdin and Kotov, 1997]. It will be demonstrated that magneto-optical effects, in particular the transverse magneto-optical Kerr effect (TMOKE), can be significantly enhanced by SPP excitations in magneto-

---

[2] In a 2DEG the collective plasma oscillations can be optically excited perpendicular to the quantization axis [Burstein et al., 1980].

plasmonic crystals (section 3.1.3) [Belotelov et al., 2011; Pohl et al., 2013a]. Temnov [2012] et al. have already shown that SPPs can be controlled by magnetic fields. On the other hand, SPPs have the ability to enhance MO effects [Akimov et al., 2012; Armelles et al., 2013; Belotelov et al., 2007; Chin et al., 2013; Ctistis et al., 2009; Khanikaev et al., 2010]. Consequently, the combination of both seems mutually beneficial.

Comparable attempts in plasmonic enhancement of MO effects have been performed with smooth ferromagnetic metal films [Bonod et al., 2004; Burke et al., 1986; Ferguson et al., 1977; Hickernell and Sarid, 1987; Newman et al., 2004; Olney and Romagnoli, 1987], smooth or perforated noble-metal/ferromagnetic-metal multilayers [Armelles et al., 2009; Clavero et al., 2010; Ferreiro Vila et al., 2008; González-Díaz et al., 2007; Temnov et al., 2010], cobalt and iron gratings [Buchin et al., 2009; Newman et al., 2008], metal/semiconductor films [Aers and Boardman, 1978], and noble metals in high magnetic fields [Strelniker and Bergman, 2008]. The limitations of these approaches will be discussed in section 3.1.1. MPC structures will be shown to combine their strengths instead while bypassing their disadvantages.

Furthermore, we investigate the dependence of the TMOKE strength on the amount of bismuth substitution and optical activity, respectively (section 3.1.4). The influence and behavior of the signals at the symmetry points of the 1.BZ and close to intersecting SPP dispersions will be analyzed in detail (section 3.1.5). Finally, data measured in reflection and transmission will be compared (section 3.1.6).

3.1.1 Magneto-Plasmonic Crystals

Dynamic control of a material's optical properties is one of the key challenges towards all-optical device applications. One of the possibilities to add a new means of control is the use of magnetic materials and the exploitation of magneto-optical (MO) effects such as the Faraday and Kerr effect. Especially, if the plane of incidence and the magnetic field vector are perpendicular, the intensity of light may be altered by the transverse magneto-optical Kerr effect (TMOKE), which will be elucidated further in section 3.1.2.

Ferromagnetic metals, such as nickel, iron or cobalt inherit a relatively strong magneto-optical response. However, the common MO effects are still only on the order of 10^{-3} and less in smooth films of these materials [Krinchik and Artem'ev, 1968; Zvezdin and Kotov, 1997], which limits their usefulness with respect to the desired modulation strength in device applications. Additionally, they have a rather large optical absorption in the visible and near infrared regime [Foiles, 1985; Ordal et al., 1983]. So instead of exploiting electronic resonances, it has been demonstrated that artificially designed geometrical resonances can instead provide an enhancement, e.g., in nanostructured metamaterials and photonic crystals containing ferromagnetic metals [Belotelov and Zvezdin, 2005; Inoue et al., 1999; Sarychev and Shalaev, 2007]. Alternative materials such as semiconductors or noble metals have shown to be inappropriate in this respect, since one would have to apply magnetic fields of several tesla in order to achieve comparable MO effects.

Magneto-plasmonic crystals (MPCs) follow the idea of nanostructuring and represent an approach that tries to combine the advantages of both classes of materials, i.e., ferromagnets and noble metals, while bypassing their disadvantages. The general design of an MPC is described in figure 3.1. A noble metal grating with sub-wavelength period d and thickness h_m on the order of the skin depth δ_m is deposited on a magnetic dielectric with thickness $h_d \gg h_m$. The non-magnetic substrate is transparent for the available range of optical frequencies and is chosen to minimize the crystal lattice mismatch with respect to the magnetic layer. SPP resonances can be excited at the metal/dielectric interface providing both, low optical losses and SPP enhanced extraordinary transmis-

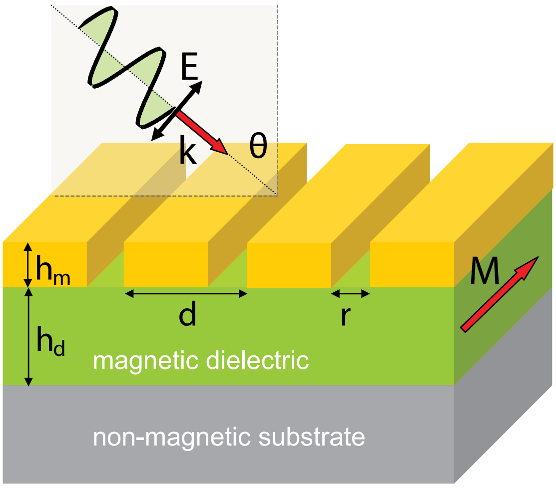

Figure 3.1: A sketch of the general design of a magneto-plasmonic heterostructure. d is the grating period, r is the slit width, h_m and h_d are the thicknesses of the metal and the dielectric, respectively. Also shown is p-polarized light incident under an angle θ, while the magnetization $\boldsymbol{M}$ is oriented perpendicular to the plane of incidence.

sion (EOT), i.e., a flux of photons per unit area transmitted through the slits of the grating that is larger than the incident flux per unit area [Genet and Ebbesen, 2007]. The magnetic material is chosen to be a dielectric instead of a metal, which further reduces absorption in the visible and near-infrared. The SPPs feel the influence of the magnetization within a distance δ_d inside the dielectric. Hence, with respect to SPP control via the magnetization, the dielectric need not be thicker than δ_d. The interplay between SPPs and controllable magnetization will be shown to significantly increase the modulation strength of the optical properties of the MPC. On the other hand, the large magneto-optical response of the dielectric promises ultrafast optical control of the magnetization, e.g., by the inverse Faraday effect. The SPPs in this context are referred to as magneto-plasmons. Their theoretical treatment is the subject of section 3.1.2.

3.1.2 Basic Properties and Plasmonic Enhancement

Upon reflection of light from the surface of a magnetized medium, three kinds of magneto-optical Kerr effects may be observed depending on the orientation of the magnetization with respect to the plane of incidence. While the polar and longitudinal effects (see figure 3.2a and 3.2b) only influence the state of polarization, i.e., rotation of the plane of polarization and degree of ellipticity, it is the transverse magneto-optical Kerr effect (TMOKE) that alters the intensity of the p-polarized component of the reflected light. In the latter case, the light penetrates the medium within the skin depth δ, where it

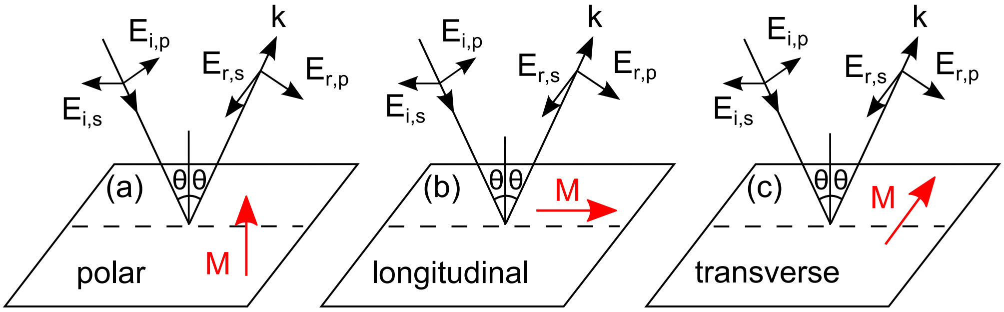

Figure 3.2: Polar (a), longitudinal (b) and transverse (c) reflection geometries for the magneto-optical Kerr effects. The subscripts “i” and “r” stand for the incident and reflected light with its p- and s-polarized components of the electric field E. The dashed line symbolizes the in-plane projection of the plane of incidence. (schematically adapted from Zvezdin and Kotov [1997])

senses the influence of the magnetization as a term proportional to M^2 in the refractive index $n_\perp$, while the refractive index $n_\parallel$ parallel to M is not affected. The modified refractive index influences the reflectivity coefficient via the Fresnel equations. When reversing the direction of light or that of the magnetization, which is the same from symmetry considerations, the boundary condition (equation 1.9) for the z-component of the dielectric displacement $D_\perp$ is different due to the asymmetric form of the dielectric tensor 1.21. In this case, the Fresnel equations, respectively the reflectivity coefficient is different as well with respect to the previous geometry leading to the non-reciprocity of the TMOKE.

Moreover, the TMOKE is odd in magnetization. Hence, it is most commonly exploited for measurements of the magnetic domains at the surface of magnetic samples. With the MPC described in section 3.1.1 it is possible to measure the TMOKE in transmission as well, which is another advantage in comparison to smooth ferromagnetic metals. Since it will be shown that the effect arises purely from light-matter interactions at the metal/magnetic dielectric interface, it will still be referred to as Kerr effect in order to distinguish it from the Faraday effect, which is a bulk related phenomenon. Consequently, the effect is characterized for reflectivity R and transmissivity T by the parameter $\delta_{R,T}$, which is defined as

$$\delta_{R,T}(E, M) = \frac{I_{R,T}(E, +\boldsymbol{M}) - I_{R,T}(E, -\boldsymbol{M})}{I_{R,T}(E, 0)} = \frac{\Delta I_{R,T}(E, M)}{I_{R,T}(E, 0)} \tag{3.1}$$

and depends on the photon energy $E = \hbar\omega$ as well as the in-plane component of the sample magnetization $\boldsymbol{M}$, which can be controlled, e.g., by an external magnetic field $\boldsymbol{B}$ in Voigt geometry.[2]

For our experiments, we use MPC samples consisting of a perforated gold layer (small optical losses for $\lambda > 650\,\mathrm{nm}$) on top of a ferromagnetic bismuth iron garnet (BIG) film (large magneto-optical response, as measured by the Faraday rotation). The parameters of the two samples used in the experiments are listed in table 3.1. In both samples, the magnetic films have been grown by liquid phase epitaxy on a gadolinium gallium garnet $Gd_3Ga_5O_{12}$ (GGG) substrate. Their magnetic anisotropy has been determined by Faraday and Kerr rotation measurements showing a significantly smaller saturation magnetic field for the Faraday geometry.[2] Consequently, the easy axis of the magnetic anisotropy is oriented perpendicular to the sample surface. The noble metal layers have been deposited using a thermal evaporation process and the grating lines have been drawn by electron-beam lithography using a fixed beam moving stage technique. The samples' geometrical parameters have been determined by atomic force microscopy.

For bismuth substituted iron garnets, the magneto-optical figure of merit, i.e., the ratio of the specific Faraday rotation to the optical absorption, is highest in the wavelength between 650 to 850 nm (1.459 to 1.907 eV). In order to design the sample parameters in a way that the SPP resonances are included in this range, the transmission and TMOKE spectra have been modeled beforehand on the basis of the rigorous coupled waves analysis (RCWA) technique extended to the case of gyrotropic materials [Li, 2003; Moharam

---

[2] The sample normal is assumed to be parallel to the light wavevector k and perpendicular to the direction of the external magnetic field.

[3] Here, $(YGdSmCa)_{2.6}$, e.g., means that there is an equal distribution of the ions Y^{3+}, Gd^{3+}, Sm^{3+} and Ca^{3+} present in the whole crystal, which occupy on average 2.6 of the three octahedrally oxygen coordinated lattice sites of each unit cell of the garnet compound. Since details of the crystal structure of rare earth substituted iron garnets are not of special importance in this chapter, the reader is referred to section 5.1.1 in this respect.

Sample	Chemical Composition	ϵ g	Geometrical Parameters [nm]	Faraday Rotation at 633 nm [°/μm]
1	$Bi_{0.4}(YGdSmCa)_{2.6}(FeGeSe)_5O_{12}$	$\epsilon = 4.98 + 0.005i$ $g = 0.0017$	$d = 595$ $r = 110$ $h_m = 120$ $h_d = 2500$	0.46
2	$(BiSmTm)_3(FeGa)_5O_{12}$	$\epsilon = 5.18 + 0.013i$ $g = 0.0051$	$d = 505$ $r = 85$ $h_m = 100$ $h_d = 5095$	~ 1

Table 3.1: Overview of the chemical composition and magnetic properties of the magnetic films including grating and geometrical parameters of the gold layer.[3] d is the grating period, r is the slit width, h_m and h_d are the thicknesses of the gold grating and the magnetic film, respectively. The diagonal (ϵ_d) and non-diagonal (gyration g) elements of the permittivity tensor 1.21 are given at a photon energy of 1.55 eV.

et al., 1995].[4] Modeling in combination with our experimental data has also been used to determine the dielectric constant and the gyration of the magnetic films.

For these MPC structures, an enhancement of Faraday and Kerr effects has been predicted theoretically near the Wood anomalies by Belotelov et al. [2007, 2009]. A very similar magneto-plasmonic crystal structure with a gold hole array on BIG has been analyzed by Wurtz et al. [2008] in the geometry of the polar Kerr effect. Although the influence of SPP excitations on the control of transmitted light could be verified, an enhancement of the MO effects by surface plasmon interaction could not be observed.

For the transverse MO Kerr effect, the SPP enhancement originates from a magnetization dependent shift of the Fano resonance frequency. According to equation 1.23, this resonance shifts to higher (lower) values for positive (negative) g_y with the sign of the latter depending on the orientation of $\boldsymbol{M}$ in the respective coordinate system. The larger the shift, the higher will be $\Delta I_{R,T}$ in equation 3.1. Consequently, for angles of light incidence close to 0°, which corresponds to low k values and a high slope of the SPP dispersion, the TMOKE is expected to have its highest angular sensitivity (see figure 1.4). In fact, to first order in the magnetization and for photon energies in the vicinity of an SPP resonance, $\delta_{R,T}$ is approximately linearly dependent on the slope of the latter as well as the field induced energy shift ΔE, i.e.,

$$\delta_{R,T}(E, M) = \frac{\Delta I_{R,T}(E, M)}{I_{R,T}(E, 0)} \approx \frac{\partial I_{R,T}}{\partial E} \frac{\Delta E}{I_{R,T}(E, 0)}, \tag{3.2}$$

where $\Delta E = E(+\boldsymbol{M}) - E(-\boldsymbol{M}) = a \cdot M$ and a is a proportionality constant. The corresponding spectral intensity close to a Fano feature has already been mentioned to have a non-resonant and resonant contribution (see equation 1.17). While the former is only weakly dependent on the photon energy and can be taken constant, the latter may in all generality be described by a normalized energy dependent function $S_{R,T}(E)$ and an amplitude $I_{0,(R,T)}$ to be $I_{r,(R,T)}(E) = I_{0,(R,T)} S_{R,T}(E)$. Substituting this into equation 3.2 yields

$$\delta_{R,T}(E, M) = \frac{a I_0 M (\partial S(E)/\partial E)}{I_{nr} + I_0 S(E)}. \tag{3.3}$$

---

[4] The theoretical modeling has been performed by V. I. Belotelov from the Moscow State University, Russia.

In the absence of SPP resonances, the spectra in reflection or transmission are usually featureless and flat with $\partial I_{R,T}/\partial E \to 0$ in equation 3.2 (even for ferromagnetic metals as mentioned in section 3.1.1). On the contrary, close to the SPP features, $\partial S(E)/\partial E$ can take rather large values leading to an SPP assisted increase of the TMOKE.

For the structure shown in figure 3.1, SPPs can propagate along both surfaces of the metal film exhibiting two types of Fano resonances, one for the Au/BIG interface and one for the Au/air interface. However, since only one surface is adjacent to the magnetic film, it has to be expected that the TMOKE enhancement will be significantly different for these two modes and contributions to the TMOKE should come predominantly from the Au/BIG plasmon. Furthermore, it should be possible to distinguish the different features of the transmission/reflection spectra originating from the metal grating, such as Rayleigh, Fabry-Perot and SPP resonances, by means of the TMOKE spectra, since only the SPP features are sensitive to the magnetic properties of the dielectric film.

3.1.3 TMOKE Enhancement in Transmission

The easy axis of the MPC's magnetic layer, i.e., the orientation of the magnetization $\boldsymbol{M}$ in the absence of an external magnetic field, is perpendicular to the sample surface but can be oriented in the sample plane by means of an electro-magnet. The intrinsic transverse magnetic (TM) polarization of surface plasmons and the requirement of the TMOKE geometry allow for two possible orientations of magnetization and light excitation of the MPC sample, one for p-polarized light and one for s-polarized light, which are illustrated in figures 3.3a and 3.3b, respectively. Figure 3.3c shows a detail of the gold grating of sample 1 obtained by scanning electron microscopy (SEM). The slits are clearly visible as dark, narrow horizontal lines. For a TM polarized surface wave, the electric field vector $\boldsymbol{E}$ of the incident light must have a non-vanishing component in the SPP propagation direction as predefined by the grating vector $\boldsymbol{\Lambda}$, i.e., $\boldsymbol{E} \cdot \boldsymbol{\Lambda} \neq 0$. Although this is the case in the geometry of figure 3.3b, here, $\boldsymbol{k} \cdot \boldsymbol{\Lambda} = 0$ so that only plasmons with $k_{\mathrm{SPP}} = 0$ can be excited (see equation 1.16). Further, the TMOKE geometry requires a magnetization perpendicular to the plane of light incidence. Finally, due to its microscopic origin discussed before, the TMOKE only occurs in p-polarized light. Since for symmetry reasons p-polarization is not defined for light normally incident on the sample, the direction of the light wavevector $\boldsymbol{k}$ must not coincide with the sample normal $\boldsymbol{N}$, which means $\boldsymbol{k} \times \boldsymbol{N} \neq 0$.

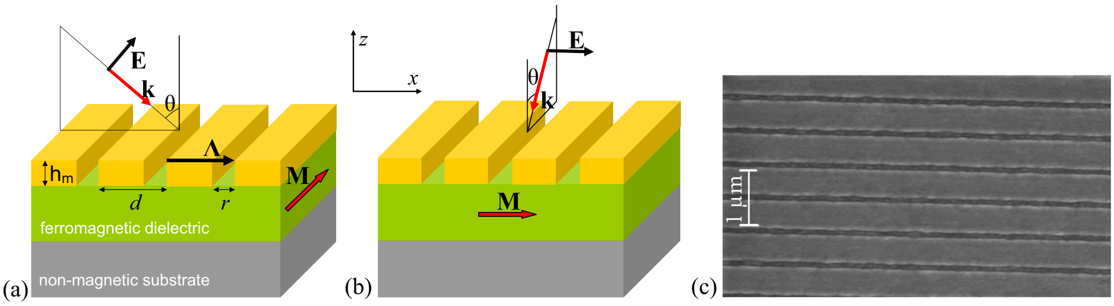

Figure 3.3: Illustration of the two possible experimental configurations for excitation of SPPs by light under the constraint of the TMOKE geometry for (a) p-polarized light and (b) s-polarized light (Λ is the grating vector) (c) Scanning electron microscopy image of the gold grating of sample 1 [Belotelov et al., 2011].

For the geometry given in figure 3.3a, the measured zero-order transmission spectra of sample 1 are shown as a contour plot in figure 3.4a for angles of incidence up to 18°.

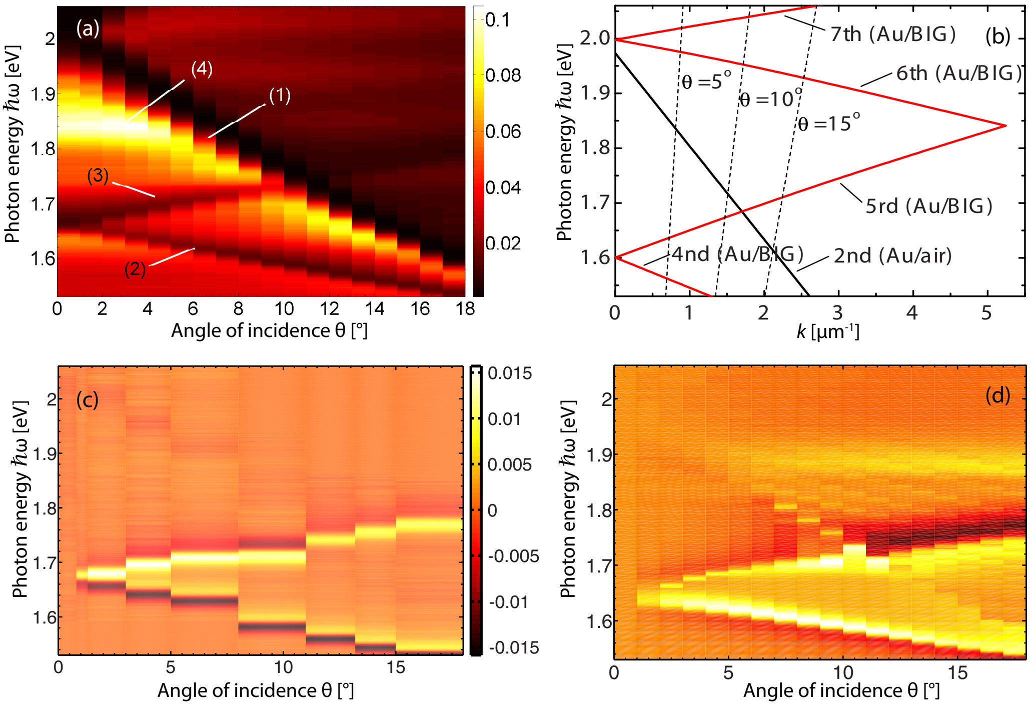

Figure 3.4: Comparison between theory and experimental data on the transmission and TMOKE spectra of sample 1 measured at an in-plane magnetic field strength of $B = 200\,\mathrm{mT}$ in the configuration of figure 3.3a: (a) Zero-order transmission up to angles of light incidence of 18° showing different features (1) to (4) (see text for details); (b) Empty lattice calculation of the SPP dispersion of the Au/air (black) and Au/BIG (red) surface plasmon in the 1.BZ. The dashed lines are the dispersions of free-space photons for different angles of incidence θ; (c) Measured TMOKE spectra corresponding to figure 3.4a; (d) RCWA simulation of the TMOKE spectra [Belotelov et al., 2011].

The theoretically calculated SPP dispersion, as seen in figure 3.3b for the 1.BZ, helps to attribute the different transmission features to the Au/air and Au/BIG plasmon, respectively. Consequently, the pronounced Fano resonance (1) must be attributed to the Wood anomaly of the second band SPP at the Au/air interface ($m = 1$ in equation 1.16). On the other hand, the Fano resonances (2) and (3) correspond to the fourth and fifth band SPP at the Au/BIG interface ($m = \pm 2$ in equation 1.16). The prominent transmission peak (4) coincides well with the calculated collective Fabry-Perot cavity mode that builds up inside the grating slits (see Belotelov et al. [2012]).

The TMOKE data corresponding to the transmission spectra in figure 3.4a is given in figure 3.4c. The TMOKE is characterized by the parameter δ_T according to equation 3.1. In order to improve the sensitivity of the white light measurements, the spectra for opposite magnetic field directions have each been repeated up to 15 times in turn by means of an automated measurement routine. Subsequent averaging resulted in a sensitivity of $\sim 10^{-3}$. While most of the data map in figure 3.4c shows values well below this experimental sensitivity, pronounced peaks (red) and dips (blue) appear, where δ_T reaches values up to 1.5×10^{-2}. The positions of this TMOKE enhancement obviously follow the dispersion of the Au/BIG plasmon, while there is no enhancement for the Au/air SPP as expected and discussed before (see figures 3.4a and 3.4b). Compared to values of 2×10^{-4} to 8×10^{-4} as obtained from electromagnetic modeling for the same sample under non-resonant conditions (no excitation of SPPs), this corresponds to an enhancement factor of ~20-100. In case of an uncovered iron garnet film, theoretical simulations predict TMOKE values of only $\delta_T \approx 1 \times 10^{-5}$, which is a factor of 1000 smaller than the ones obtained experimentally with the MPC sample.[5]

The results are supported by a RCWA calculation of the TMOKE for the structure under investigation (figure 3.4d), where dispersion has been taken into account for both, the dielectric constant ϵ_d and the gyration g,[6] while the data for the gold permittivity has been adapted from Johnson and Christy [1972]. The simulation is in excellent agreement with the experimental data of figure 3.4c.[5]

Further information can be taken from single transmission and TMOKE spectra, i.e., vertical cross-sections of figures 3.4a and 3.4c, at selected angles of light incidence θ (see figure 3.5). Due to symmetry reasons, the TMOKE vanishes for normal incidence ($\theta = 0°$) as discussed before, while it amounts to values of $\sim 1\,\%$ already at a small angle of $\theta = 0.8°$ showing a pronounced dip and peak around a photon energy of 1.6 eV in agreement with the SPP dispersion of the Au/BIG plasmon in figure 3.4b (green and red curves, respectively, in figure 3.5a). Hence, already at small angles of incidence, the symmetry at the sample surface is broken and two SPP modes are excited at slightly different energies. Their resonance frequency is shifted upon reversal of the direction of magnetization according to equation 1.23 and as a consequence the TMOKE appears. The TMOKE seems to be sensitive to the excited magneto-plasmon modes, in contrast to the transmission spectrum, which does not change notably when going from normal

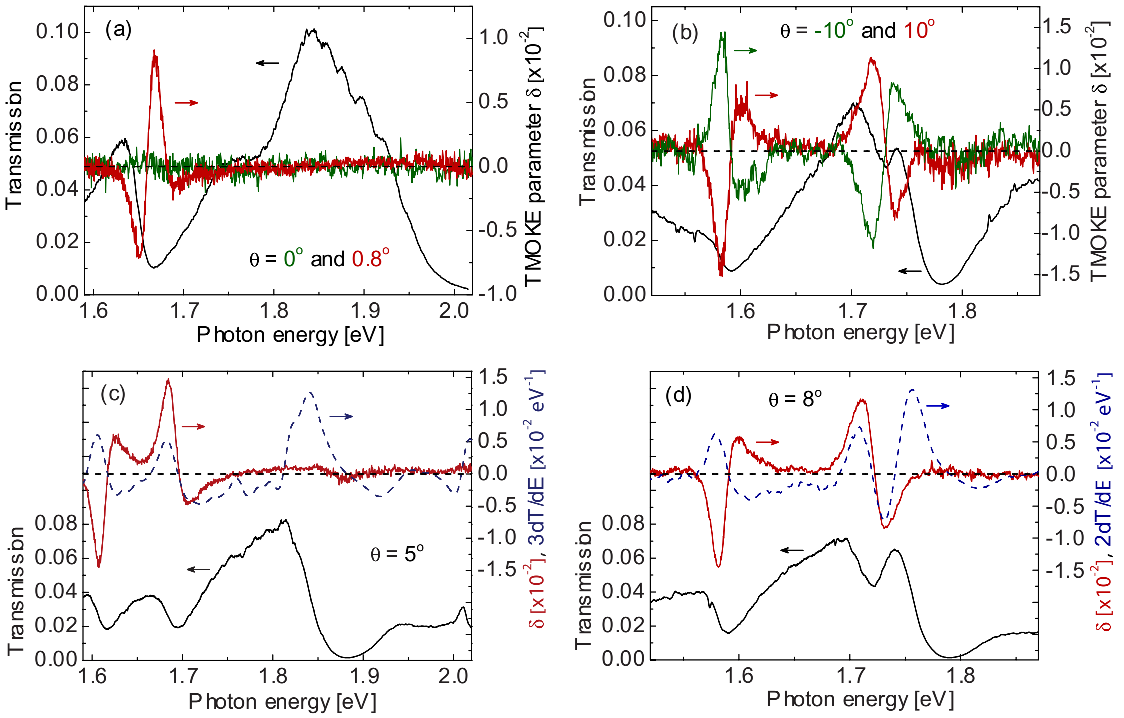

Figure 3.5: Transmission spectra (black), their derivatives dT/dE (dashed blue, multiplied by a factor in order to compare with δ_T) and the corresponding TMOKE parameters δ_T (red, green) at angles of light incidence of (a) 0° and 0.8°, (b) −10° and 10°, (c) 5° and (d) 8°. The spectra represent cross-sections of figures 3.4a and 3.4c. The magnetic field for these measurements was 200 mT [Belotelov et al., 2011].

---

[5] The theoretical modeling has been performed by V. I. Belotelov from the Moscow State University, Russia.

[6] e.g., at $\lambda = 650\,\mathrm{nm}$, $\epsilon_d = 5.12 + 0.018i$ and $g = (3.4 + 0.4i) \times 10^{-3}$, and at $\lambda = 750\,\mathrm{nm}$, $\epsilon_d = 5.07 + 0.005i$ and $g = (1.9 + 0.2i) \times 10^{-3}$.

to slightly oblique incidence. There are no TMOKE features for the other resonances in the transmission spectrum, i.e., the peak at $E = 1.84\,\mathrm{eV}$ and the dip at $E = 1.99\,\mathrm{eV}$. Obviously, the TMOKE shows a different sensitivity with respect to the excitation of different eigenmodes of the structure.

Increasing the angle of incidence, increases the energy separation of the two excited plasmon modes ($\theta = \pm 10^\circ$ in figure 3.5b). In this case, the modes are excited at the fourth and fifth branch of the Au/BIG plasmon dispersion (compare figure 3.4b). Since the branches have different slopes, the SPP group velocity $d\omega/dk$ is different and the two plasmons wave packages travel in opposite directions. Hence, not only appear two TMOKE features in the spectrum, each accompanying one of the modes, but their sign of δ_T is reversed with respect to each other. This is a consequence of the fact that the two modes travel in opposite directions with respect to the toroidal moment ($\boldsymbol{M} \times \boldsymbol{N}$). From symmetry considerations, it is identical to either switching the directions of the magnetic field or reversing the angle of light incidence from $\theta = +10^\circ$ to -10°. The latter is demonstrated in figure 3.5b. Since the directions of SPP propagation are now reversed, the TMOKE features appear at the same energies as before but with reversed sign. Thus, the observed effect is not an experimental artifact but on the contrary, it is odd in the magnetization, which is a well known characteristic of the TMOKE [Zvezdin and Kotov, 1997].

As explained in the context of equation 3.3, the parameter δ_T is proportional to the derivative dT/dE of the transmissivity T with respect to the photon energy E in the vicinity of the SPP resonances, since δ_T occurs mainly owing to the magnetization induced shift of the latter. This is visualized in figures 3.5c and 3.5d (blue dashed lines). It can be seen that the positions of the TMOKE peaks coincide well with the positions of the derivative's extrema. However, not every extremum of dT/dE is accompanied by a TMOKE feature as they are related to either SPP resonances at the Au/air interface or to cavity modes inside the slits. Moreover, one can observe that the resonance energy of the TMOKE features does not necessarily coincide with any maxima or minima of the transmission resonances, which can be explained by the Fano type shape of the latter (see section 1.1.3).

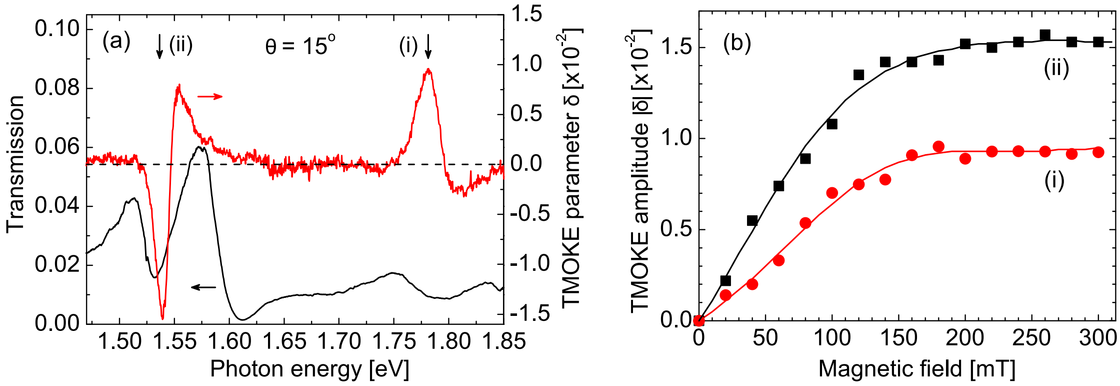

Figure 3.6: (a) Transmission (black) and TMOKE spectrum (red) at 15° angle of incidence showing two pronounced TMOKE features at 1.54 eV and 1.78 eV with labels (ii) and (i), respectively. (b) The magnetic field dependence of the amplitude $|\delta|$ of features (i) (red circles) and (ii) (black squares) up to field strengths of 300 mT [Belotelov et al., 2011].

Even if the Fano resonances in transmission are only weakly pronounced as, e.g., for peak (i) in figure 3.6a at 1.78 eV, the TMOKE still indicates their energy positions. The magnetic field dependence of the amplitude of the two peaks (i) and (ii) is shown in figure

3.6b for field strengths of the external in-plane magnetic field up to 300 mT. While the dependence is linear at small field strengths, saturation sets in for values above 160 mT. This corresponds well to the sample's effective uniaxial magnetic anisotropy field, which indicates that an application of an in-plane magnetic field of this strength leads to a near-complete in-plane orientation of the sample magnetization and thus to a saturation of the TMOKE.

Up to now, only the configuration of figure 3.3a has been discussed, i.e., the light was p-polarized and the magnetization $\boldsymbol{M}$ parallel to the grating slits. All other possible configurations obeying the condition that $\boldsymbol{M}$ is perpendicular to the plane of light incidence are listed in table 3.2. If the light was s-polarized in the geometry 3.3a, the orientation of the electric field would violate the TM-polarized character of the surface plasmons and hence no SPPs could be excited. Apart from that, it has already been mentioned that the TMOKE appears only for p-polarized light[7] so that this case is labeled both as "No-SPP" and "No-TMOKE" (see section 3.1.2). In the configuration of figure 3.3b, on the other hand, $\boldsymbol{M}$ is oriented perpendicular to the slits and the light is s-polarized. If, here, the light was p-polarized instead, the TMOKE would be allowed, but again no TM-polarized modes, e.g., SPPs could be excited. Consequently, this case is labeled "No-SPP" and "TMOKE".

	p-polarized	s-polarized
$\boldsymbol{M} \parallel$ slits	SPP, TMOKE	(1) No-SPP, No-TMOKE
$\boldsymbol{M} \perp$ slits	(3) No-SPP, TMOKE	(2) SPP, No-TMOKE

Table 3.2: Overview of the experimental configurations under the condition of perpendicular plane of incidence and sample magnetization $\boldsymbol{M}$. The cases are distinguished by the orientation of $\boldsymbol{M}$ with respect to the grating slits and by the type of linear polarization of the incident light. For allowed (forbidden) TMOKE and SPP excitation, the cases are labeled "TMOKE" ("No-TMOKE") and "SPP" ("No-SPP"), respectively.

Transmission and TMOKE spectra for the cases (1), (2) and (3) of table 3.2 are shown in figure 3.7. The cases (1) and (3) are characterized by the absence of SPP excitations. As a result both corresponding transmission curves T(1) and T(3) are flat and featureless. Although in case (3) the TMOKE is in general allowed, the measured δ_T values are well below our experimental sensitivity. This is not surprising since, as mentioned before, the theoretically predicted value for δ_T is on the order of 10^{-4}. On the other hand, SPPs can be excited in case (2), which results in a transmission spectrum T(2) showing pronounced peaks and overall increased intensity. However, despite SPP excitation, a TMOKE enhancement does not occur as seen in curve $\delta(2)$, since the effect is not allowed in this configuration.

3.1.4 Magnetic Field Dependence and Bismuth Substitution Level

Now that the enhancement of the TMOKE by SPP excitation could be verified, it is desirable to understand the dependence of its amplitude $|\delta|$ on the sample parameters. Therefore, we compared the magnetic field dependencies of particularly strong TMOKE features of samples with different bismuth content c_{Bi}. Apart from samples 1 and 2, a third sample with an even higher bismuth substitution and chemical composition

---

[7] ...if the magnetic permeability $\mu = 1$ and the form of the dielectric tensor $\hat{\epsilon}$ has the form 1.21...

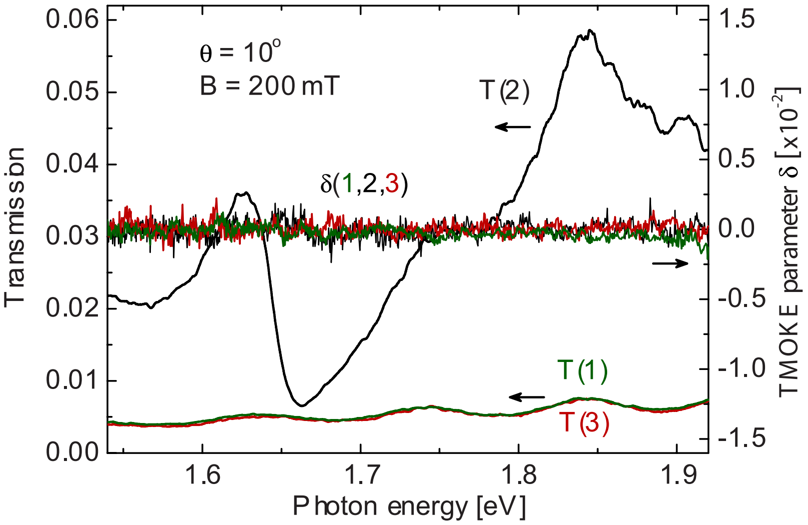

Figure 3.7: Experimental demonstration of the role of SPP excitation for the enhancement of the TMOKE. Shown are the transmission and TMOKE spectra for the cases (1), (2) and (3) of table 3.2 at 10° angle of incidence and a magnetic field of 200 mT. The transmission is uniformly flat (T(1) and T(3)) unless SPP excitation is allowed and Fano resonances appear in T(2). Yet, in either of the cases, without SPP excitation, the δ values are below the spectral resolution of the setup, which is in agreement with the theoretical prediction. [Belotelov et al., 2011].

$Bi_{1.8}Lu_{1.2}Fe_{3.6}Al_{1.4}O_{12}$ has been analyzed.[8] The data is shown in figure 3.8.

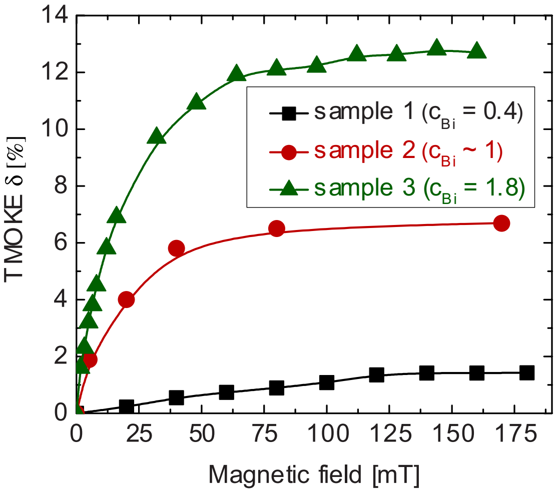

Figure 3.8: Magnetic field dependence of the TMOKE amplitude $|\delta_T|$ measured under oblique incidence for three samples with different bismuth content c_{Bi}. Shown are the peak values for one particularly strong feature of each sample. The saturation value increases with increasing c_{Bi}. Sample 3 (triangles) has the chemical composition $Bi_{1.8}Lu_{1.2}Fe_{3.6}Al_{1.4}O_{12}$. The data for sample 1 can be viewed in more detail as curve (ii) in figure 3.6b [Pohl et al., 2013a].

The TMOKE amplitudes of all three samples show a linear increase at low magnetic fields as the sample magnetization is turned away from the easy axis to the direction of the external magnetic field. This is followed by a saturation when the directions of external field and sample magnetization are identical. The same progression has already been observed in the context of figure 3.6. However, with increasing bismuth substitution level, the TMOKE saturation value increases from 1.5 % (sample 1, $c_{Bi} = 0.4$) to 13 % (sample 3, $c_{Bi} = 1.8$), which is about an order of magnitude.

The saturation magnetic fields, on the other hand, depend on the samples' magnetic

---

[8] The corresponding measurement for this sample has been performed by L. E. Kreilkamp from the Technische Universität Dortmund, Germany

anisotropies as well as their compositions and thicknesses. Samples 1 and 2 have a uniaxial magnetic anisotropy perpendicular to their surface, while the anisotropy of sample 3 forms only a small angle with its surface. The smallest saturation magnetic field is achieved for sample 2 with roughly 60 mT, which is most probably related to a slightly favorable chemical composition in this sample with respect to the energy necessary to shift its magnetization.

From equation 1.23 one can see that the difference in the wavevector Δk and thus the energy shift ΔE in equation 3.2 depends on the gyration g. Hence, it has to be concluded that the chemical composition, especially the amount of bismuth substitution, influences the sample's gyration, i.e., its optical activity. Consequently, materials with optimized chemical composition should be able to yield both, high TMOKE values and low saturation magnetic fields, which is highly desirable with respect to low-power all-optical control.

3.1.5 SPP-SPP Coupling and Spectral Tunability

The achieved signal amplitudes above 10 % should already be sufficiently high for commercial device applications, such as optical switches and modulators. However, owing to the two different plasmon modes that the MPC structure supports, there is further potential in the spectral regions where the Au/air and Au/BIG plasmon dispersions intersect and SPP-SPP coupling becomes possible.

In order to analyze this interaction, sample 2 has been characterized over a broad range of frequencies and angles within the 1.BZ. The measured spectra have been fitted with equation 1.18 to obtain the correct positions of the Fano resonances. The results are shown in figure 3.9a for transmission (empty circles) and reflection (full circles) measurements for the Au/BIG (red) and the Au/air (black) plasmon. The dashed lines are guides to the eye. Clearly, for incidence angles around 45°, the two plasmon dispersions intersect, which is accompanied by an anti-crossing behavior and a splitting of the dispersion branches. This energy splitting is characteristic for a strong coupling between the two plasmon modes.

The data is supported by a Drude model calculation in the empty-lattice approximation based on the sample's parameters given in table 3.1 (figure 3.9b). The theoretical dispersions are in good agreement with the experimental data except for the anti-crossing, since SPP-SPP interaction is not considered in this approximation. Exemplary single spectra (black) with the corresponding Fano fits (red) are shown for various angles of incidence in figures 3.9c, 3.9e and figure 3.9d in transmission and reflection, respectively.

Corresponding TMOKE spectra of sample 2 are given in figures 3.10a and 3.10b with the focus on the regions close to the symmetry point $k = 0$ and around the SPP-SPP intersection including the edge of the 1.BZ, respectively. The external field has been held constant at 170 mT, which is well above the saturation field. The angular shift of the features are visualized by the red (Au/BIG plasmon) and black (Au/air plasmon) dashed lines, which closely follow the experimentally obtained dispersion given in figure 3.9a.

At the high symmetry points at the center and edge of the 1.BZ, the TMOKE vanishes to zero. Here, two plasmons are excited simultaneously with equal energy but opposite wavevectors, i.e., opposite propagation directions. As has been shown earlier, the signs of the corresponding features are reversed for the two modes in this case (see figure 3.5b) and the TMOKE cancels to zero.

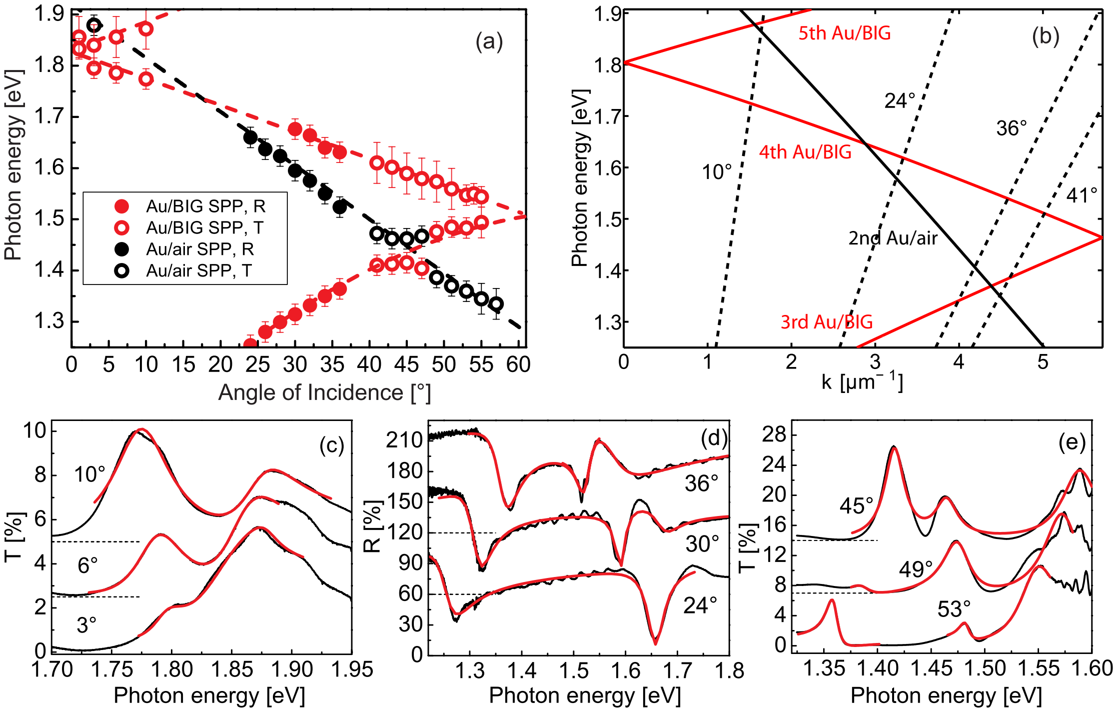

Figure 3.9: (a) Measured SPP dispersions for the Au/BIG (red) and Au/air (black) plasmon of sample 2. The data has been obtained by fitting the transmission features with equation 1.18. For angles around 45° and a photon energy of 1.39 eV the dispersions of the two plasmon modes reveal an anti-crossing behavior. (b) Empty-lattice calculation corresponding to figure 3.9a within the 1.BZ. The dashed lines are free-space photon dispersions for different angles of incidence. (c)-(e) Selected transmission and reflection spectra (black) with the respective Fano fits (red) corresponding to the data in figure 3.9a. The spectra are shifted for clarity. The dashed lines correspond to zero level [Pohl et al., 2013a].

Close to the crossing of the SPP dispersions at ∼ 45° (see figure 3.9a), features appear, which must be attributed to the Au/air plasmon according to their frequency shift. This is surprising, since only the Au/BIG magneto-plasmon is expected to contribute to the TMOKE signals, while the Au/air plasmon should be insensitive to the magnetic properties of the garnet layer. However, due to the finiteness of the gold layer (see h_m in table 3.1) and the subsequent SPP-SPP coupling, the eigenenergies of the two oscillating modes are coupled as well. This is explained within the framework of a coupled oscillator model, which gives the eigenfrequencies of the coupled modes as

$$\omega_\pm^2 = \frac{1}{2}(\omega_a^2 + \omega_d^2 \pm \sqrt{(\omega_a^2 - \omega_d^2)^2 + 4\eta_1\eta_2}). \tag{3.4}$$

Here, ω_d and ω_a are the eigenfrequencies of the uncoupled modes at the metal/magnetic dielectric and the metal/air interfaces, respectively. $\eta_{1,2}$ are the coupling coefficients, which are determined by the grating parameters, e.g., if the metal layer was significantly larger than the skin depths of both SPPs, $\eta_{1,2}$ would become negligible. Equally, if the difference of the two eigenfrequencies is sufficiently large, so that $(\omega_a^2 - \omega_d^2) \gg \sqrt{\eta_1\eta_2}$, the coupling coefficients are negligible as well and the two eigenfrequencies are independent of each other. Else, $\omega_\pm$ becomes dependent on both frequencies. Since ω_d depends on the magnetization according to equation 1.23, where $g \propto M$, also ω_a depends on M in this case and the TMOKE features are enhanced along both plasmon dispersions close to their intersection.

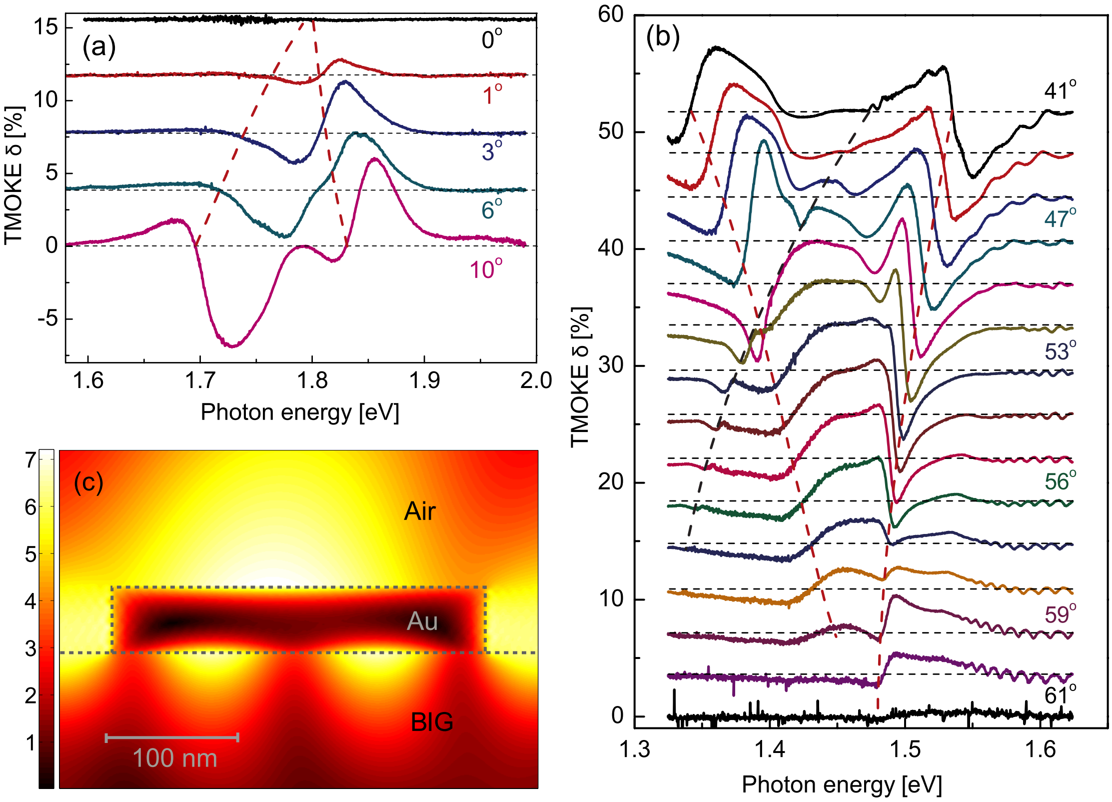

Figure 3.10: TMOKE spectra of sample 2 for angles of incidence (a) from 0° to 10° (close to $k = 0$) and (b) from 41° to 61° (i.e., at the edge of the 1.BZ, compare figures 3.9a and 3.9b). The dashed lines are guides to the eye representing the shift of the TMOKE features. At both edges of the 1.BZ, the TMOKE vanishes due to symmetry reasons. Else, the features follow closely the Au/BIG magneto-plasmon dispersion (red dashed lines). Yet, at the intersection of the Au/BIG and Au/air plasmons, TMOKE features appear that can be attributed to the Au/air plasmon as well (black dashed line). (c) The calculated near field spatial distributions of the square of the absolute value of the magnetic field $|H|^2$ at $\theta = 49°$ incidence angle and $E = 1.38\,\text{eV}$ [Pohl et al., 2013a].

The main enhancement is observed at 1.4 eV and 47° incidence, i.e, in the near vicinity of the anti-crossing, with a TMOKE amplitude of 8.5 %. Further, at angles close by (42°, 1.4 eV), the transmission exceeds values of 25 %. This is much higher than expected considering the ratio of the area with grating slits to the total illuminated area of the structure including light diffraction by sub-wavelength apertures (see, e.g., Genet et al. [2003]). This phenomenon is referred to as enhanced optical transmission (EOT). Due to the finite grating depth, the Au/air plasmon can tunnel from the front to the Au/BIG interface and is subsequently scattered in the foward direction contributing to the transmitted intensity (see Genet and Ebbesen [2007] and references therein).

Figure 3.10c shows a simulation of the near field distribution of the square of the modulus of the magnetic field $|H|^2$ in the vicinity of the metal layer at 1.38 eV and 49° incidence.[9] Obviously, there are two SPPs excited simultaneously at both interfaces of the gold in this region close to the anti-crossing, which supports the concept of surface plasmon interaction.

---

[9] … as obtained by a rigorous coupled wave analysis (RCWA), which has been performed by V. I. Belotelov from the Moscow State University, Russia.

3.1.6 Transmission Versus Reflection

It has been discussed earlier, that the Kerr effect is a surface rather than a bulk effect. In order to support this statement, we performed measurements of the TMOKE in reflection geometry as well. Figure 3.11 gives a comparison between transmission and reflection signals of sample 2 at angles of incidence of 31° and 33°.

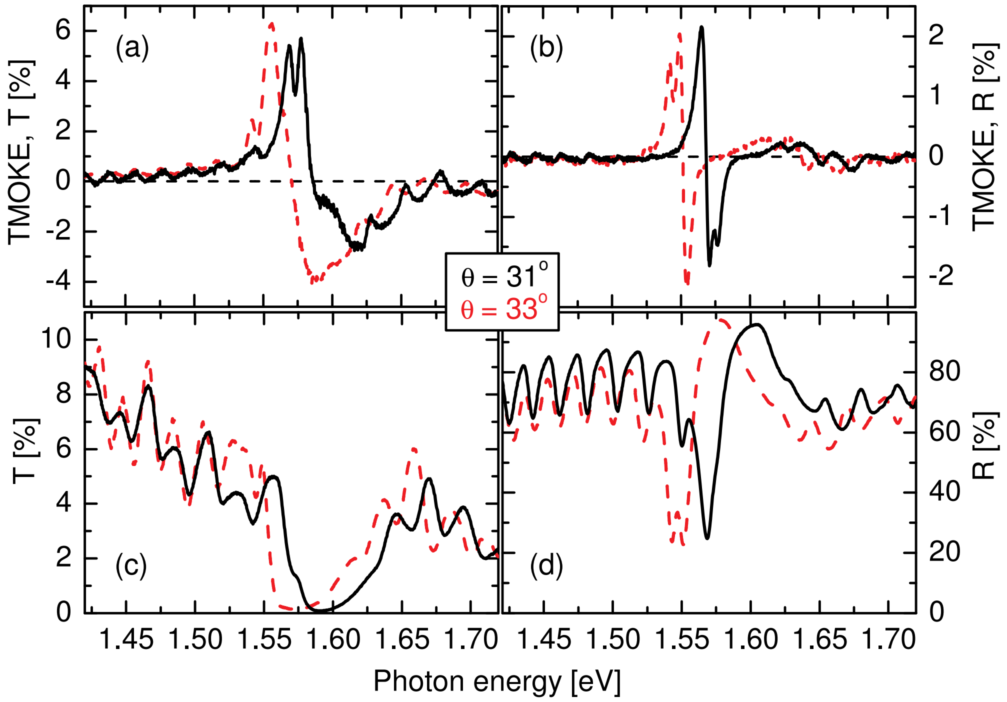

Figure 3.11: Comparison of the TMOKE signals of sample 2 (a) in transmission and (b) in reflection for the angles of incidence $\theta = 31°$ (solid) and $\theta = 33°$ (dashed) measured at $B = 170\,\mathrm{mT}$. The effect can be well observed in reflection geometry with similar signal shape and behavior. Yet, despite similar shapes, the reflection amplitudes are significantly smaller than the ones measured in transmission (see text for more details). The corresponding transmission and reflection spectra are shown in figures 3.11c and 3.11d, respectively [Pohl et al., 2013a].

The signals shift with the angle according to their dispersion. In reflection (figure 3.11b), as predicted, the features appear at the same photon energies with similar shapes and energy shift as in transmission. All signals are superposed by oscillations around 5.9 THz. Assuming Fabry-Perot (FP) resonances inside the magnetic film the frequency corresponds to a calculated film thickness around 4.9 μm, while the actual (measured) thickness is 5.095 μm (see table 3.1), which is close enough to support the assumption. The oscillations are however much smaller than the TMOKE values. In figure 3.11b, the oscillation amplitude, i.e., the interferometric visibility, is largely reduced due to a negligible amount of reflected light penetrating the bulk magnetic film. This unambiguously proves the Kerr effect to originate solely from the surface and with no or negligible contribution from the bulk medium.

Since the amount of non-resonantly scattered light I_{nr} is much smaller than the SPP mediated light I_r in transmission, one can see from equation 3.3 that in this case the I_0 cancel each other and the observed effect is independent on the amount of transmitted light but rather depends on the shift of the Fano resonances. On the other hand, I_{nr} cannot be omitted in reflection and since it enters in the denominator of equation 3.3, the corresponding signal amplitudes are reduced by a factor of three with respect to figure 3.11a. Moreover, the signal linewidth is reduced in reflection to 9 meV compared to 33 meV in transmission,[10] which must be attributed to the difference in the Fano shapes with respect to the transmission spectra (see figures 3.9c-3.9e).

3.2 Ultrafast Transient Phenomena in Gold Films

Recently, the interest in plasmonics has been accelerated by the prospect of nanometallic circuits for data processing [Brongersma and Shalaev, 2010; Schuller et al., 2010]. However, as discussed in this chapter's introduction, state-of-the-art microchip technology requires modulators with an active component, i.e., the manipulation of the optical properties must inherit some means of external ultrafast control or stimulus. One approach, which has also been elucidated in the first part of this chapter, is based on magneto-plasmonics. The speed of the modulation is limited by the dynamics of the magnetization inside the medium. Characteristic time constants, here, are in the nanosecond regime (see, e.g., [Hansteen et al., 2005]).

While the previous part of this chapter was concerned about the modification of the optical properties of an MPC sample by manipulation of the dielectric layer, here we will focus on the manipulation of the metal part of the sample. The optical properties of the metal layer of an MPC can be modified by intense laser pulses as well. The characteristic time scales, here, are determined by the interactions inside the electron system, which will be shown to relax significantly faster than 1 ps in thin gold films. With the advance of femtosecond lasers providing excitations with high peak pulse energies on timescales much shorter than the electron thermalization, the femtosecond optical response in the metal is consequently determined by a non-thermal electron distribution with possibly new and interesting properties. However, for most metals, the reflectivity in the visible and near-infrared optical range is close to 1 so that most of the light energy is not absorbed by the sample. Plasmonic nanostructures can immensely improve this situation by providing Fano resonances with absorptions as high as 80 % and more (see figure 1.5), which is another example of plasmon enhanced light matter interaction and moreover reduces the operational energy expense.

Similar investigations have been performed on aluminum and gold by MacDonald et al. [2009]; Rotenberg et al. [2009], respectively, with two-color pump-probe experiments. Here, the probe beam couples light into an SPP mode via a perforated metal or dielectric structure. The active component consists of an ultrashort pump beam perturbing the electron system of the metal close to its interband absorption peak (for gold, this is the d-band to Fermi surface transition in figure 1.3). Modulations in the differential reflectivity of up to 10 % could be observed with sub-picosecond dynamics by means of amplified pulse fluences of 50 mJ/cm^2. However, close to this interband transition, the absorption and the subsequent damping is rather high, which significantly decreases the propagation length of the excited SPPs and yields a huge disadvantage with respect to plasmon driven optical circuits.

In this section, it will be demonstrated that the dielectric function of the metal and hence the optical properties of the MPC can be efficiently modified far from any intrinsic electronic resonances of the material on a femtosecond timescale. Compared to the previously mentioned works, we observe modulation amplitudes for the differential transmission and reflection spectra roughly one order of magnitude smaller but with nearly 500 times less pump fluences. Moreover, from the spectral and temporal depen-

---

[10] Here, the linewidth is taken to be the distance in energy between the maximum and the minimum of the TMOKE signal.

dences of the measured dynamics, we can extract comprehensive information about the electron relaxation mechanisms in gold. Especially the influence of SPP presence on the relaxation times will be discussed.

3.2.1 The Role of SPPs

For the experiments, the pump-probe technique as described in section 2.1 has been applied. If not stated otherwise, the full width at half maximum (FWHM) of the pulse intensity for both, pump (pp) and probe (pr) beams, is $\tau_D = 25\,\mathrm{fs}$. The MPC sample under study is schematically shown in figure 3.12a illustrating one specific geometry for the incident beam directions and polarizations. In this geometry, the pump and probe beams are both incident on the same spot under the angle of $\theta_1 = \theta_2 = 17°$ with an aperture angle around 6°. While the former is p-polarized with non-zero wavevector projection on the direction of the grating vector Λ ($\equiv x$-direction), the latter is s-polarized with $k_x = 0$. Hence, as discussed in section 3.1.3, SPP excitation is in general allowed if the sample provides the corresponding resonance for the angle of incidence.

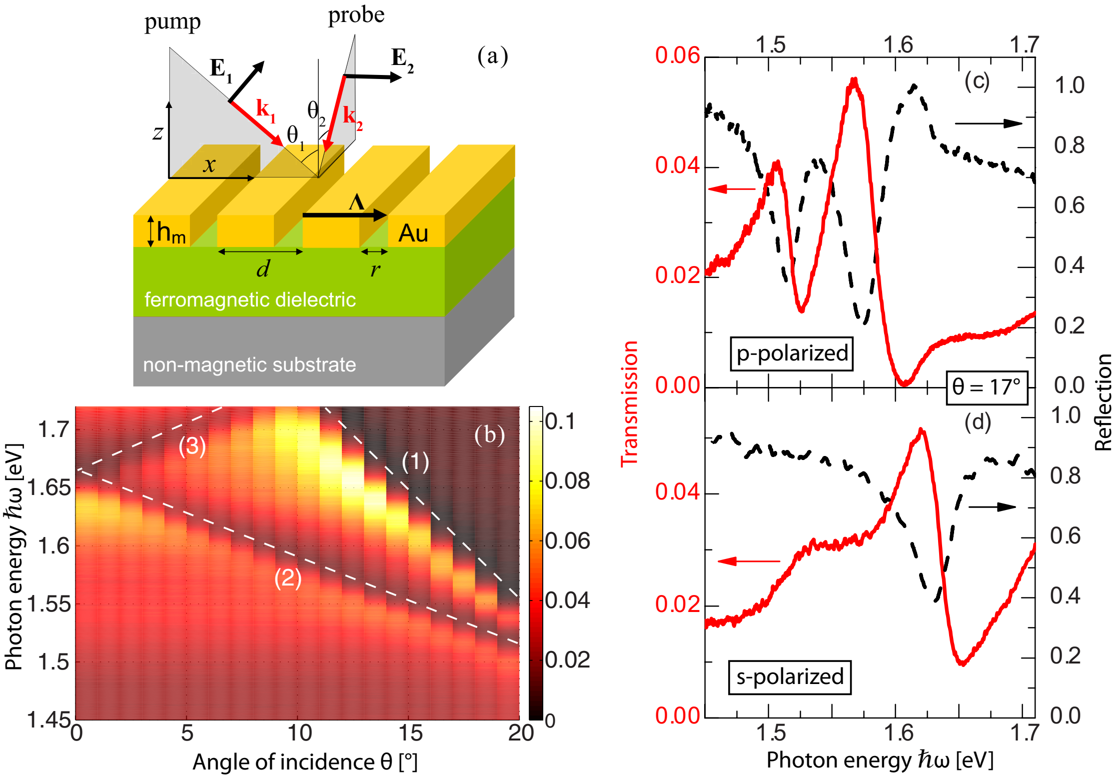

Figure 3.12: (a) Schematic illustration of the wavevector orientations and polarizations of the pump and probe beams incident on the MPC structure for active control experiments. (b) Contour plot of the zero-order transmission spectra for different angles of incidence. The dashed lines are guides to the eyes representing the Au/BIG (curves (2) and (3)) and Au/air plasmon dispersions (curve (1)) calculated earlier (see figure 3.4b) (c)+(d) Zero-order transmission spectra for beams incident under $\theta = 17°$ for p- (pump) and s- (probe) polarization, respectively [Pohl et al., 2012].

Sample 1 (see table 3.1) has been designed to provide resonances in the range 1.5-1.7 eV for both polarizations. Its transmission and reflection spectra, measured using a spectrally broad white light source, are shown in figure 3.12c and 3.12d for p- and s-polarized light, respectively, corresponding to the geometries of figure 3.12a, i.e., for

17° incidence. In p-polarized light, Fano resonances show up around energies of 1.53 eV and 1.60 eV. The complete angle dependence of the transmission resonances of sample 1 is shown in figure 3.12b up to angles of 20°. The dashed lines are guides to the eye representing the fourth (2) and fifth (3) branch of the Au/BIG plasmon and the second branch (1) of the Au/air plasmon dispersion as obtained by an empty lattice calculation (see figure 3.4b). Since for s-polarized light directed along the grating slits the light transfers zero momentum to the SPP, the resonance around 1.63 eV observed in figure 3.12d corresponds to $k_x = 0$, which is equivalent to $\theta = 0°$ in p-polarization and is also well reproduced by the measured dispersion. Consequently, the resonances can be identified as Wood anomalies and it can be stated that in the configuration of figure 3.12a the pump beam (p-polarized) will excite SPPs in the fourth band of the Au/BIG dispersion (curve (2)) and the second band of the Au/air dispersion (curve (1)), while the probe beam will excite Au/BIG SPPs at the center of the 1.BZ (intersection of curves (2) and (3)). Although it is possible to excite localized SPPs in plasmonic crystals, here, we deal with propagating SPP modes, which can be seen from the non-zero slope of the SPP dispersion in figure 3.12b.

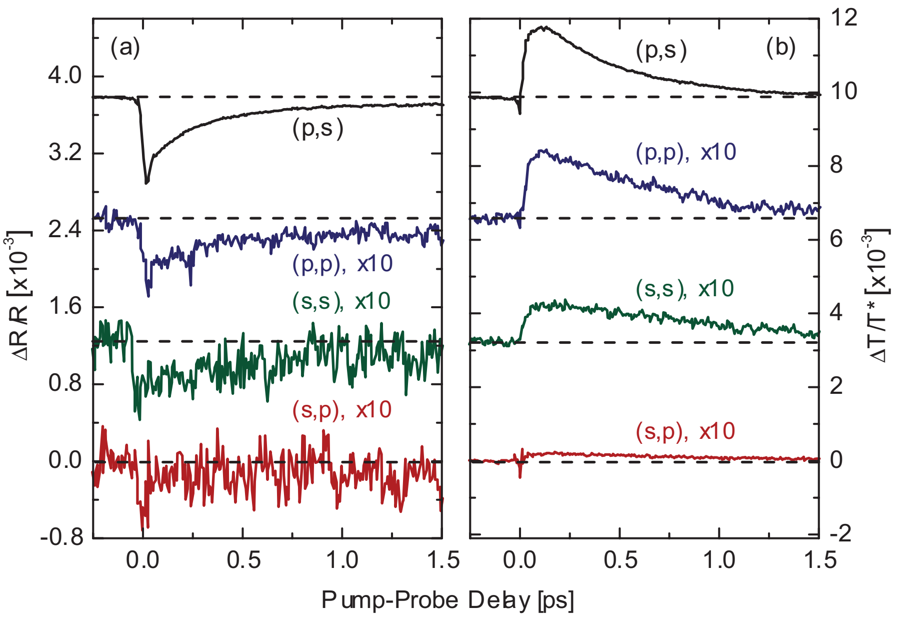

Figure 3.13: Time resolved differential (a) reflectivity and (b) transmissivity signals for different polarizations (p- or s-polarized) of the pump and probe beams (pump,probe) at a pump fluence of 120 μJ/cm^2. Apart from the (p,s) configuration, in which both beams excite SPP modes, the signals of the remaining configurations are multiplied by a factor of 10 since their amplitudes are significantly smaller. The signals are shifted for clarity. Dashed lines correspond to zero levels. T^* is the effective transmission of the probe light (see text).

In order to analyze an influence of SPP excitations on the induced and detected changes of the sample's optical properties, polarization dependent measurements of the differential reflectivity and transmissivity have been performed (see figure 3.13a and 3.13b, respectively). The observed signals have a non-trivial shape exhibiting multiple contributions on different time scales. However, the overall dynamics relaxes on the order of 1 ps or faster. The phase of the (spectrally integrated) main signal contribution is opposite for the differential transmission and reflection, i.e., the former is increased, while the latter decreases as a result of the pump induced changes.[11]

In order to interpret the signal amplitudes correctly, it is important to take into account the influence of the gold grating on the transmitted probe intensity T, for which the grating acts similar to a "wire-grid" polarizer (see Hecht and Zajac [2003]). The electric field of a p-polarized probe beam drives the conducting electrons to oscillate along the slits of the grating, which in turn causes the electrons to re-radiate an electromagnetic wave in forward as well as backward direction. Due to a phase shift of π the forward re-radiated wave partly cancels the incident wave via destructive interference resulting in strongly diminished transmission. In the direction perpendicular to the slits, the oscillations of the electrons are limited to small length scales so that for an s-polarized probe beam the transmitted wave is mostly unchanged by the grating. This effect enhances the values for the differential transmissivity $\Delta T/T$ by roughly a factor of 5 for s-polarized probe beams. Since we are interested in the SPP influence on the signals and not in the influence of the grating as a polarizer, effective transmission values T^*, which are scaled accordingly, have been used in order to be able to compare the pure SPP mediated contributions to the signals.

Obviously, for the configuration depicted in figure 3.12a, which corresponds to (p,s) for the pump and probe polarizations, the signal amplitudes are increased by a factor of 10 at least compared to all other configurations. In this specific geometry, both, pump and probe beams excite SPP modes according to figure 3.12b. The pump plasmon strongly increases the energy absorption into the sample with absorption ratios of 70 % and more (see, e.g., figure 1.5). On the other hand, the Fano feature resulting from the probe SPP shifts according to equation 1.14 with the pump induced, wavelength dependent changes of the material's dielectric permittivities. This way, the sensitivity to the changes of the optical properties experienced by the probe beam, such as transmissivity or reflectivity, are largely enhanced.[12] If either one or the other SPP is switched off by changing the respective polarization (see curves (p,p) and (s,s), respectively), the signal amplitude is significantly decreased. The relative reduction in the amplitudes suggests that the influence of pump and probe SPPs for the signal amplitude, i.e., energy absorption and resonance shift, is comparable. Finally, if both SPP modes are extinguished at once, the signal amplitude experiences another reduction by about an order of magnitude. The results demonstrate the importance of the presence of surface plasmon modes for the excitation and detection of ultrafast all-optical modulation with an overall enhancement to the non-plasmonic configuration of two orders of magnitude.

3.2.2 Interpretation within the Non-Thermal Electron Model

Since the energy of the plasmon that was previously excited by the pump pulse is smaller than the interband transition energy of gold $\Omega_{ib} \approx 2.4\,\mathrm{eV}$ (see figure 1.3), it loses its energy due to intraband absorption while propagating along the surface (internal damping). In our case the SPP has mainly photon character, since the central energy of both, pump and probe pulses, of $\hbar\omega_{pp} = \hbar\omega_{pr} = 1.55\,\mathrm{eV}$ are significantly lower than the surface plasmon energy in gold $\hbar\omega_{sp} \approx 3.61\,\mathrm{eV}$.[13] The internal damping creates a hot electron distribution of the conduction band electrons in the energy range from the Fermi energy

---

[11] The correct signal phase has been determined by direct detection of the strongly attenuated (modulated) pump beam in transmission. The so obtained phase has been kept constant for all subsequent measurements including reflection measurements.

[12] It should be noted that a maximum sensitivity and thus enhancement is expected for a spectrally narrow probe pulse initially positioned on a point of maximum spectral slope of the SPP resonance.

[13] $\omega_{sp} = \omega_p/\sqrt{1+\epsilon_d}$, with plasmon frequency $\omega_p = 13.4 \cdot 10^{15}\,\mathrm{Hz}$ and $\epsilon_d = 4.97$

E_F to $E_F + \hbar\omega_{pp}$, which modifies the dielectric constant and thus the optical properties, such as transmissivity and reflectivity, of the metal. The subsequent test pulse probes the same intraband transitions and additionally the transition from the fully occupied d-band to the depopulated electron levels from $E_F - \hbar\omega_{pp}$ to E_F. Its differential transmission and reflection therefore reproduce the dynamics of the hot electron distribution and grant a deeper insight into the intrinsic relaxation processes of the non-thermal electron distribution inside the metal (see also Del Fatti et al. [2000]). As mentioned in the previous section, the probe pulse is able to excite a second (probe) SPP. This way, the modification of ϵ_m by the pump is additionally experienced through a shift of the probe plasmon resonance through equation 1.14, which alters the (wavelength dependent) optical response significantly. This indirect plasmonic part can enhance the signal by a factor of 10 and more depending on the spectral width of the probe pulse and its position on the SPP resonance.

When modeling the electron relaxation dynamics of laser heated metals, a common approach is the two-temperature model (TTM), within which the metal is separated into two subsystems corresponding to the electron system and the ionic lattice with temperatures T_e and T_i, respectively. In the case $T_e > T_i$, the energy relaxation and thermalization processes are described by two coupled heat equations under the assumption that the individual subsystems are in a thermalized state at all times. It is known by now that this assumption fails in the case of femtosecond excitation, i.e., with pulse durations much shorter than the electron thermalization time. Here, the incompletely thermalized electron distribution can have a tremendous influence on, e.g., the electron-phonon relaxation time resulting in a need to evolve the TTM into the more general concept of the non-thermal electron model (NEM) [Groeneveld et al., 1995]. In this section, it will be shown, that the obtained results can be well incorporated into the NEM and are also in good agreement with numerical simulations based on a rigorous coupled-wave analysis (RCWA).

In order to establish a quantitative connection between the light induced change of the electron distribution and the differential transmissivity and reflectivity signals, one usually applies the following procedure (see also Del Fatti et al. [1998] and Del Fatti et al. [2000]):

1. The amplitudes C_j of the transient differential reflection and transmission signals are written as linear combinations of the changes of the real and imaginary part of the metal's dielectric function ($j = R, T$):

$$C_j = C_{1,j}\frac{\Delta\epsilon_1}{\epsilon_1} + C_{2,j}\frac{\Delta\epsilon_2}{\epsilon_2}. \tag{3.5}$$

   Since in our experiments, the photon energies of the applied laser pulses are far from the d-band transition in gold, ϵ_1 and ϵ_2 can be considered constant for the energy range of interest.

2. The expansion coefficients $C_{1,j}$ and $C_{2,j}$ can be calculated using the theoretical reflection and transmission formula for thin films [Sun et al., 1994] or by modeling T and R spectra applying a numerical rigorous coupled wave analysis (RCWA) [Pohl et al., 2012].

3. ϵ_2 can be directly related to the joint density of states (JDOS), which gives the number of allowed optical transitions in a material at a specific photon energy $\hbar\omega$ [Smith, 1971]. Entering the JDOS is the energy distribution of the joint density of states (EDJDOS) $D(E, \hbar\omega)$, which can be calculated assuming a parabolic band

structure for the 5d-, 6p- and 6s- bands in the vicinity of the L-Point of the Brillouin zone for gold [Rosei, 1974]. Finally, the expression for the change of the imaginary part of the dielectric function is found to be

$$\Delta\epsilon_2(\hbar\omega, T) = \frac{8\pi^2 e^2 \hbar^4}{3m^2(\hbar\omega)^2} \int D(E, \hbar\omega)\Delta f(E, T)dE, \tag{3.6}$$

where f is the electron distribution. The different contributions of the transitions to the JDOS should be weighted with the respective transition matrix elements, which has been omitted here (constant matrix element approximation).

4. $\Delta\epsilon_1$ is calculated via the Kramers-Kronig relation, since $\Delta\epsilon_2$ is only nonzero in a narrow range around the interband transition energy:

$$\Delta\epsilon_1(\omega) = \frac{2}{\pi} CHW \int_0^\infty \frac{\omega' \Delta\epsilon_2(\omega')}{\omega'^2 - \omega^2} d\omega', \tag{3.7}$$

where CHW is the Cauchy principal value of the integration [Groeneveld et al., 1995].

5. The electron distribution kinetics $\Delta f(t)|_{E=const,T=const}$ can be determined from the Boltzmann transport equation with electron-electron and electron-phonon collision integrals C [Groeneveld et al., 1995; Pitaevskii and Lifshitz, 1981]:

$$\frac{df}{dt} = C_{e-e} + C_{e-ph}. \tag{3.8}$$

6. The result for the electron distribution kinetics is introduced in equation 3.6. In combination with equation 3.5, the time resolved differential transmissivity and reflectivity signals can be modeled with an arbitrary thermal or non-thermal initial electron distribution $f(E)$. The latter case will be referred to as the NEM throughout the rest of the text.

From a qualitative point of view, according to the NEM, the shape of the transient signals due to a modification of ϵ (originating from a change of the electron distribution according to equation 3.5) is supposed to be determined by the following two contributions. It should be noted here that the dielectric constant of the metal can be split in an interband and an intraband part as follows:

$$\epsilon_m = \epsilon_1^{ib} + i\epsilon_2^{ib} - \frac{\omega_p^2}{\omega(\omega + i\gamma)}, \tag{3.9}$$

where $\gamma = \gamma_{e-e} + \gamma_{e-ph}$ is the complete electron scattering rate. While $\Delta\epsilon_2^{ib}$ is peaked in a narrow spectral range around the electron d-band transition in gold, it is the broad spectral distribution of $\Delta\epsilon_1^{ib}$ that gives rise to the significant contributions to the transient signals even far from this intrinsic resonance.

1. After energy injection, the electron distribution is peaked in a narrow range between E_F and $E_F + \hbar\omega_{pp}$. At this point, the electron-electron scattering rate γ_{e-e} is not only weakened by the Pauli exclusion principle (see "electron-electron interaction" in Kittel [2004]), but is in general also reduced due to electrostatic (Coulomb) screening by the d-band electrons in gold. Additionally, the initial small amount of non-thermal electrons quenches the electron-phonon relaxation rate γ_{e-ph}. Only

when the excess energy is distributed among a large number of electrons via electron-electron scattering, γ_{e-ph} increases, accelerating the relaxation process. Consequently, the short time behavior of the signal should be non-exponential due to the initially non-thermalized electron gas. (The increasing energy loss rate of the electrons to the lattice should be reflected by $\Delta\epsilon_1$, which is sensitive to the integrated absorption spectrum [Del Fatti et al., 1998]. For the off-resonant case it can be shown (see Groeneveld et al. [1995]) that $\Delta\epsilon_1 \approx \Delta\epsilon_1^{ib} \propto \Delta E_e$, with the electron-gas excess energy E_e.)

2. Since in our experiments $\hbar\omega_{pp} + \hbar\omega_{pr} > \hbar\Omega_{ib}$, $\Delta\epsilon_2$ is dominated by its interband part $\Delta\epsilon_2^{ib}$ on a short time scale due to the transitions from the d-band to the empty electron states in the conduction band. These holes are short lived, since they lie significantly below the Fermi energy (about 1 eV). They behave in the same way as the corresponding electrons, namely that their scattering probability increases the further their energy is away from the Fermi level [Kittel, 2004]. Consequently, a fast peak of $\Delta\epsilon_2$ is expected below 100 fs (see also Del Fatti et al. [2000]).

   The subsequent behavior of $\Delta\epsilon_2$ is dominated by intraband absorption, which enters via a change in the scattering rate $\Delta\gamma$ (equation 3.9). Here, at earlier stages, the efficiency of the electron-phonon part of the scattering rate increases as the lattice temperature T_i rises, increasing the phonon occupation numbers. Subsequently, $\Delta\epsilon_2$ reaches a plateau (just as T_i does) and relaxes over time scales longer than the experimentally covered delays [Groeneveld et al., 1995]. The contribution of the electron scattering rate to $\Delta\epsilon_1$ is negligible [Del Fatti et al., 1998].

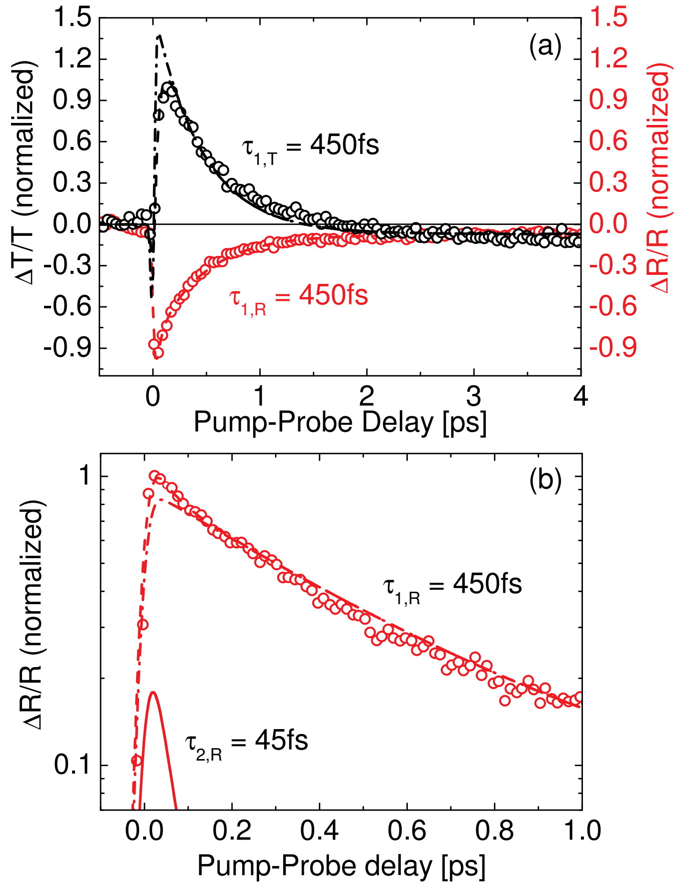

Figure 3.14: Top: Exemplary (normalized) time resolved differential transmissivity (black circles) and reflectivity (red circles) data at $T = 300\,\mathrm{K}$. Also plotted are fits to the data with equation 3.10 for $A_{2,T} = 0$ (dash-dotted black line) and for $A_{2,j} \neq 0$ (red and black dashed lines). Both curves show a relaxation time of $\tau_{1,j} = 450\,\mathrm{fs}$ ($j = R, T$). Bottom: In reflection, the contribution of the $A_{2,R}$ term of equation 3.10 is shown on a logarithmic scale (solid line) as the difference of two fits to the data. Its relaxation time is determined to be $\tau_{2,R} = 45 fs$ (also see figure 3.15).

Using equations 2.6, 2.7 and 2.8, these qualitative predictions of the NEM can be well reproduced by the linear response fit-function ($j = R, T$)

$$\begin{aligned}\frac{\Delta I}{I}(t) =& D_j e^{-\left[\frac{t}{\sigma}\right]^2} + \\ &+\frac{A_{1,j}}{2}\left[1+\operatorname{erf}\left(\frac{t}{\sigma}-\frac{\sigma}{2\tau_{1,j}}\right)\right] e^{\left[\frac{\sigma}{2\tau_{1,j}}\right]^2-\frac{t}{\tau_{1,j}}} + \\ &+\frac{A_{2,j}}{2}\left[1+\operatorname{erf}\left(\frac{t}{\sigma}-\frac{\sigma}{2\tau_{2,j}}\right)\right] e^{\left[\frac{\sigma}{2\tau_{2,j}}\right]^2-\frac{t}{\tau_{2,j}}} + \\ &+\frac{B_j}{2}\left[1+\operatorname{erf}\left(\frac{t}{\sigma}\right)\right],\end{aligned} \tag{3.10}$$

whose summands will be explained in the following. Each of them corresponds to one of the features described above except for the first term. This term corresponds to an instantaneous response, which follows the cross-correlation function of the laser pulses. This component can be also seen in the differential reflection from flat gold when the beams are incident from the magnetic film side. Since the response from flat gold in the differential reflection without the support of SPPs is smaller than our experimental sensitivity of $5 \cdot 10^{-5}$ in this case, we attribute this signal to the nonlinear optical response from the magnetic film related with optical transitions in octahedrally coordinated Fe^{3+} ions [Grishin and Khartsev, 2009; Pohl et al., 2012]. The second and third terms are connected to the optically induced excitation of electrons and their energy relaxation in gold, i.e., to the changes of the imaginary and real part of the interband dielectric function $\Delta\epsilon_2^{ib}$ and $\Delta\epsilon_1^{ib}$, respectively, as will be shown below. The last term is related to the change of the electron scattering rate $\Delta\gamma$, whose dynamics are close to that of the lattice temperature T_i, i.e., in the nanosecond regime and show up as a plateau on the time scales accessible to our experiments.

The corresponding ultrafast dynamics of the transient signals can be seen in figures 3.14a and 3.14b at room temperature. The applied pump fluence in these measurements was $120\,\mu\mathrm{J/cm}^2$. The corresponding maximum deposited laser energy density is $U_l = 6.8\,\mathrm{J/cm}^3$, which is equivalent to an electron temperature rise of $\Delta T_e = 245\,\mathrm{K}$.[14] Considering that the calculation of this quantity has a rather large uncertainty in the spot size of the laser pulse, we give a value here that rather overestimates U_l and ΔT_e, respectively. Still, at least at room temperature, the experiments can be claimed to be performed in the low perturbation limit, i.e., $\Delta T_e < T_e$.

While the reflectivity (red circles) shows a fast rise followed by a decay to a plateau, the transmissivity signal (black circles), which is opposite in sign, has an additional instantaneous response related to a nonlinear optical excitation in the dielectric [Pohl et al., 2012]. Furthermore, the subsequent peak is significantly delayed on the order of 150 fs, which is considerably longer than the width of the pump-probe autocorrelation.

For the transmissivity, two fits to the data using equation 3.10 are shown. One of them ($A_{2,T} = 0$) corresponds to the previously applied data analysis (see Pohl et al. [2012]). In contrast to the fit with $A_{2,T} = 0$ (dashed-dotted black line in figure 3.14a), the fit with $A_{2,T} \neq 0$ (dashed black line) reproduces the signal quite good, especially in the short time region below 100 fs. The same goes for the fit of the reflectivity data with $A_{2,R} \neq 0$ (dashed red line). Here, a difference can only be seen on a logarithmic scale

---

[14] Since the energy dissipating into the electron gas is determined by the Poynting vector $\vec{S} = \frac{1}{2}\vec{E} \times \vec{H}^*$, whose magnitude is the optical intensity $I \propto |\vec{E}|^2$, the intensity is taken to be the relevant quantity for the determination of the skin depth into the metal [Saleh and Teich, 2007].

(dashed and dashed-dotted red lines in figure 3.14b). The solid red line is the difference of the two fits, revealing the typical relaxation time of $\tau_{2,R} = \tau_{2,T} = 45\,\text{fs}$ in contrast to the $A_{1,j}$ term, which relaxes with the time $\tau_{1,T} = \tau_{1,R} = 450\,\text{fs}$. Both relaxation times are determined from statistics that have been performed and will be discussed in the context of figure 3.15.

With respect to the above discussion, we believe that the fast $A_{2,j}$ component describes the interband contribution of the imaginary part of the dielectric function $\Delta\epsilon_2^{ib}$. Although it is small, this feature cannot be omitted (as has been done by Pohl et al. [2012]), especially in the transmissivity, since here, the $A_{1,T}$ and $A_{2,T}$ amplitudes have different signs, which results in the delayed maximum of the main peak.[15] It has been argued however, that a genuine signal rise time can occur for off-resonant conditions due to the non-instantaneous increase of the scattering efficiency γ, which contributes to the intraband part of $\Delta\epsilon_2$ [Del Fatti et al., 1998]. This is usually expected for the reflectivity, where the coefficient for $\Delta\epsilon_2$ in equation 3.5 is several times higher than in transmission. In our case, the off-resonant condition $\hbar\omega_{pp} + \hbar\omega_{pr} < \hbar\Omega_{ib}$ is not strictly fulfilled so that $\Delta\epsilon_2$ is dominated by its interband part instead, as described above. Secondly, the rise time is known to decrease with the excitation power due to a weakening of the Pauli exclusion [Del Fatti et al., 2000], which could also explain its absence, considering a rather high electron temperature rise in our experiments ($\Delta T_e = 245K$, see text above).

3.2.3 Dependence on the Deposited Laser Energy U_l

It is known, that the two-temperature model (TTM) fails to predict the kinetics of a laser heated electron gas if the latter is non-thermalized on timescales significantly larger than the laser pulse duration. This becomes especially important for the case of low excitation powers and low temperatures due to the Pauli-exclusion principle. Among other things, the TTM predicts a relaxation time τ_e of the energy U_e of the electron gas that depends on the deposited laser energy U_l as $\tau_e \propto U_l^{1/2}$ for the low perturbation limit (for temperatures higher than the Debye temperature) [Groeneveld et al., 1995]. Thus, a deviation of the experimentally observed dependence of the relaxation times from the prediction of the otherwise well established TTM would be a clear indication that effects of a non-thermalized electron gas have to be considered.

Figure 3.15a and 3.15b show the fit results of measurements of the transient signals on U_l as represented by the laser pump fluence in the range from $12\,\mu\text{J/cm}^2$ ($\Delta T_e = 33\,\text{K}$) to $300\,\mu\text{J/cm}^2$ ($\Delta T_e = 390\,\text{K}$). Although the latter value clearly cannot be considered in the low perturbation limit, figure 3.15b reveals the absence of any dependence of the relaxation times on the pump fluence within error bars, neither for $\tau_{1,j}$ (black), nor for $\tau_{2,j}$ (red). Instead, the fits give the identical constant values in transmission (empty squares) and reflection (solid circles), which have been already used in the previous section.

The insensitivity of the relaxation times to the deposited laser energy is in accordance with the results of other groups, e.g., Groeneveld et al. [1995], although their maximum induced electron temperature rise was well in the low perturbative regime ($\Delta T_e = 61\,\text{K}$). In contrast to this, Del Fatti et al. [2000] performed experiments on thin gold and silver films, showing not only a decrease in the rise time (see discussion above), but also an increase in the relaxation times if ΔT_e exceeds $300\,\text{K}$ (for silver). The latter was attributed to a temperature dependence of the electron heat capacity. Both phenomena are not observed in our signals (see figure 3.15b), although our maximum temperature

---

[15] This phenomenon must not be confused with a rise time.

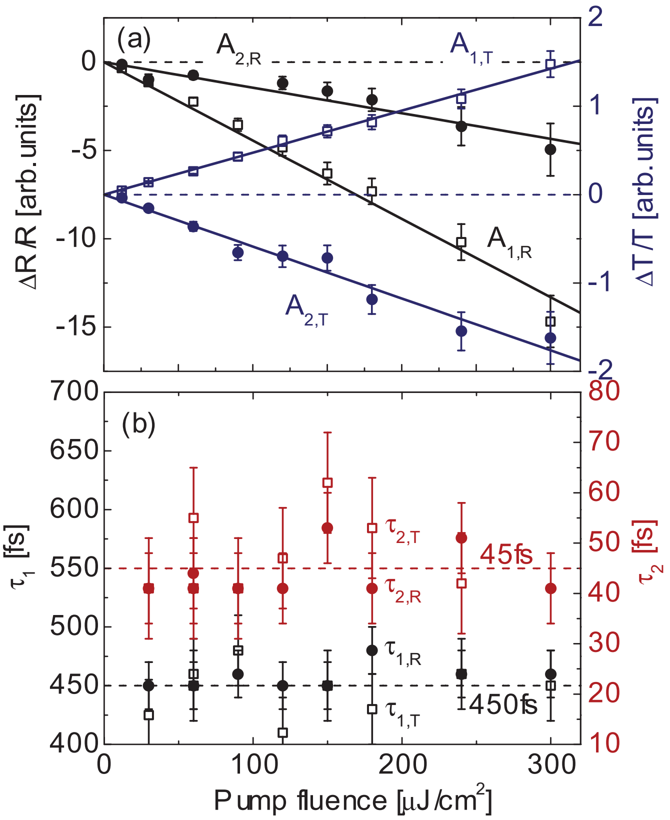

Figure 3.15: Dependence of the amplitudes $A_{1,j}$ and $A_{2,j}$ (top) and the relaxation times $\tau_{1,j}$ and $\tau_{2,j}$ (bottom) of the transient signals on the pump fluence in transmission ($j = T$) and reflection ($j = R$) evaluated from fits of the experimental data (see equation 3.10). The corresponding minimum and maximum induced rise of the electron temperature ΔT_e amounts to 25 and 390 K. Top: The signal amplitudes show a linear dependence on the excitation power. Bottom: The relaxation times can be assumed constant and identical for both, transmission and reflection data, with $\tau_{1,j} = 450fs$ and $\tau_{2,j} = 45fs$ ($j = R, T$).

rise should be above the mentioned threshold. Additionally, the corresponding $A_{1,j}$ and $A_{2,j}$ amplitudes (figure 3.15a) for the reflectivity (black) and transmissivity (red) show a linear dependence on the pump fluence. Thus, our results indicate that we are still in the linear regime, probably overestimating the induced electron temperature rise as mentioned above. Secondly, an exact value for the threshold electron temperature rise ΔT_e separating the weak- from the strong perturbation regime in gold is not available from Del Fatti et al. [2000] and remains to be determined, e.g., by calculations based on the NEM.

3.2.4 Spectral Dependence

The polarization dependence shown earlier demonstrated the importance of SPP modes for the enhancement of the measured differential signals. Consequently, the latter should inherit a strong dependence on the probe photon energy $\hbar\omega_{pr}$ close to the SPP resonance energy, i.e., a resonant behavior of the signal amplitudes. However, previous results not only indicated a dependence of the amplitudes of the transients on the probe photon energy but they also showed a wavelength dependence of their relaxation times [Pohl et al., 2012]. This was attributed to different relative contributions of the wavelength dependent amplitudes $C_{1,j}$ and $C_{2,j}$ in equation 3.5, which both were described with the same relaxation time (the corresponding real and imaginary parts $\Delta\epsilon_1$ and $\Delta\epsilon_2$ are considered frequency independent in the narrow spectral range of our laser pulses, whose energy is far from the interband resonance). However, following the above discussion, we can now identify the amplitude $A_{1,j}$ to the relaxation of the electron gas excess energy, whose relaxation is essentially that of $\Delta\epsilon_1^{ib}$. Additionally, $A_{2,j}$ can be connected to the interband part of the dielectric permittivity $\Delta\epsilon_2^{ib}$, while its intraband part is represented by the coefficient B_j. With this separation, the corresponding relaxation times are separated as well. Considering that these times are connected to characteristic material properties such as the electron-electron and electron-phonon scattering times as described in section 3.2.2, it is only reasonable to assume that they should be equal both, in transmission and reflection, and not show a significant wavelength dependence in the considerably narrow spectral range of the probe pulse (about 0.3 eV).

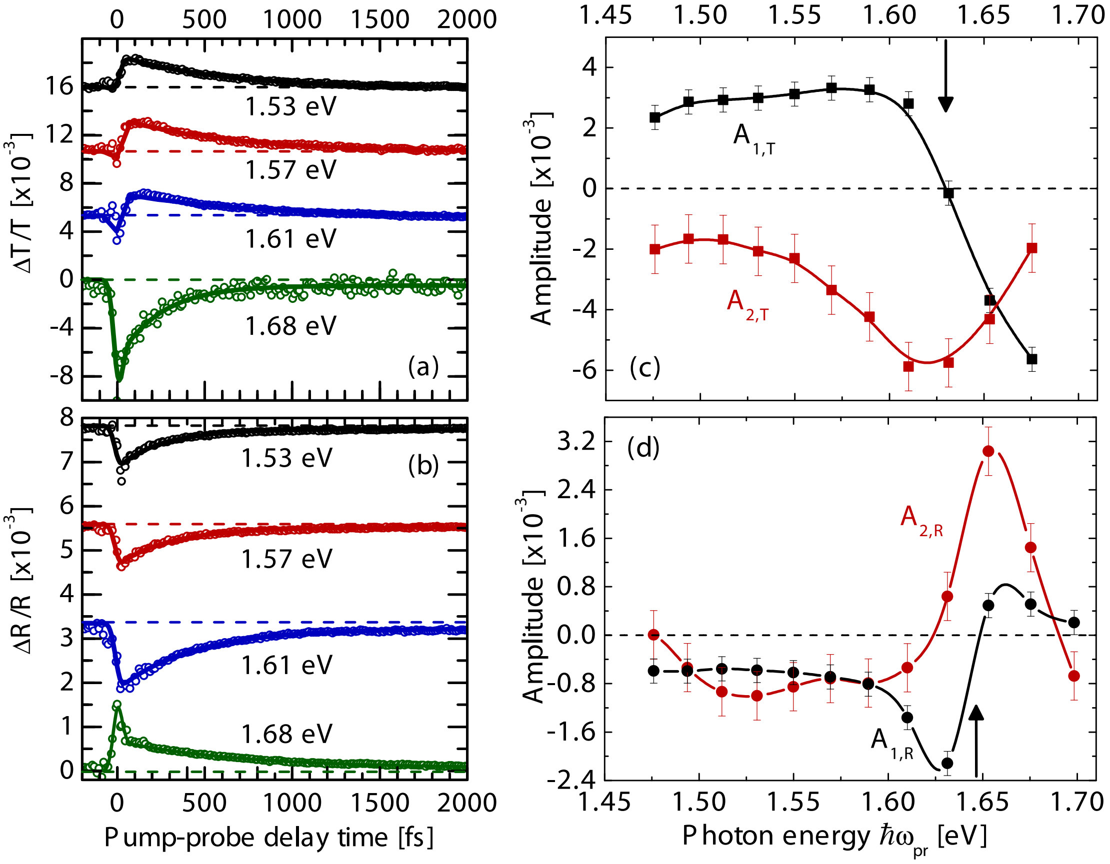

Figure 3.16: Spectral dependencies of the amplitudes $A_{1,j}$ and $A_{2,j}$ of the transient signal in transmission (top: $j = T$) and reflection (bottom: $j = R$) evaluated from fits of the experimental data (see equation 3.10). The solid lines are guides for the eyes.

Measurements of the transient signals in dependence of the probe photon energy have been performed using an electrically tunable color filter with a bandwidth of 20 meV in front of the detector unit (see figures 3.16a and 3.16b). Indeed, applying the full fit function 3.10 to the data, the results show no variation of the relaxation times within experimental errors (see figure 3.15b). The dependence of the amplitudes on the probe photon energy $\hbar\omega_{pr}$ are given in figures 3.16c and 3.16d for the transmissivity (solid squares) and the reflectivity (solid circles), respectively, with $\tau_{1,j}$ and $\tau_{2,j}$ as given in the context of figure 3.14. The amplitudes $A_{1,j}$ and $A_{2,j}$, which can now be connected to $\Delta\epsilon_1^{ib}$ and $\Delta\epsilon_2^{ib}$ (see text above), respectively, show the expected resonant spectral behavior with a sign change of $A_{1,j}$ and a corresponding extremum of $A_{2,j}$ at the probe SPP resonance energy. This result is also in accordance with the Kramers-Kronig relations between the real and imaginary part of the dielectric permittivity in the vicinity of a resonance. Due to the large thickness of the gold layer (120 nm), the response from the magnetic dielectric is negligible in reflection. The respective coefficient has thus been set to $D_R = 0$, which provides a more reliable fitting procedure, since the contributions of

D_R and $A_{2,R}$ would be less distinguishable than in transmission otherwise (considering that they eventually have the same amplitude and similar response times).

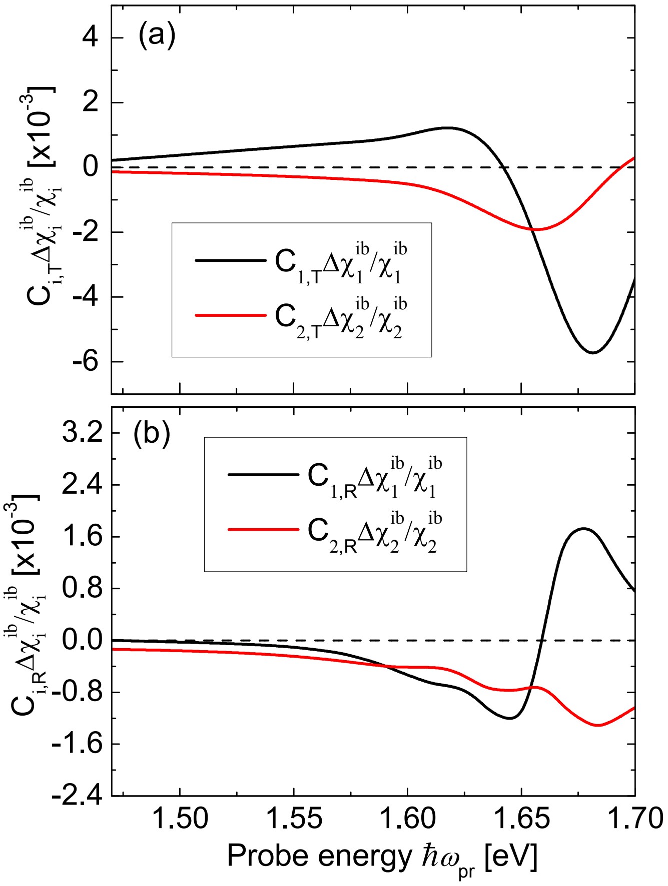

Figure 3.17: Spectral dependencies of different signal contributions related to $\Delta\chi_1^{ib}$ (black) and $\Delta\chi_2^{ib}$ (red) according to equation 3.11 with only the interband parts of the dielectric susceptibility considered as discussed in the text. The transient changes for (a) the differential transmission and (b) the differential reflection are obtained by RCWA modeling to have the best correspondence with the experimental data of figures 3.16c and 3.16d. [Pohl et al., 2012].

With the previous discussion, equation 3.5 can be altered to include only the interband contributions of ϵ, respectively the dielectric susceptibility $\chi = \epsilon - 1$ in order to account for the second and third term of equation 3.10, i.e., ($j = R, T$)

$$A_{1,j}(\omega) = C_{1,j}(\omega)\frac{\Delta\chi_1^{ib}}{\chi_1^{ib}}$$
$$A_{2,j}(\omega) = C_{2,j}(\omega)\frac{\Delta\chi_2^{ib}}{\chi_2^{ib}}. \tag{3.11}$$

The results of a RCWA simulation in order to model the spectral behavior of these coefficients are given in figure 3.17.[16] The experimental results of figures 3.16c and 3.16d are in good agreement with the calculations. Especially in transmission, the resonant behavior is well reproduced both, qualitatively and quantitatively. The theoretical results in reflection also show the expected resonant behavior with a sign change of $A_{1,R}$ close to the SPP resonance. However, there is a significant difference to the experiment with respect to the $A_{2,R}$ coefficient. This might originate from the numerous simplifications and approximations considered while deriving the expressions 3.11 but is more likely related to the close proximity, i.e., indistinguishability of the values for $A_{1,R}$ and $A_{2,R}$ over a broad spectral range, especially at higher photon energies, which complicates the

---

[16] The theoretical modeling has been performed by V. I. Belotelov from the Moscow State University, Russia.

modeling process (see figure 3.16). However, the previous identification of the coefficients $A_{1,j}$ and $A_{2,j}$ with $\Delta\epsilon_1^{ib}$ and $\Delta\epsilon_2^{ib}$, respectively, and hence the microscopic picture of the electron relaxation processes given above is further supported by the theoretical calculations.

3.2.5 Temperature Dependence

In contrast to the above measurements, which have all been performed at room temperature, we also measured the temperature dependence of the transmissivity signals in the range from $T = 10\,\mathrm{K}$ to $T = 300\,\mathrm{K}$. This has been done by means of a liquid helium flow cryostat at a pump fluence of $46\,\mu\mathrm{J/cm}^2$, which corresponds to $\Delta T_e = 270\,\mathrm{K}$ and $110\,\mathrm{K}$ at $T = 10\,\mathrm{K}$ and $T = 300\,\mathrm{K}$, respectively. Again, the signals have been fitted with equation 3.10. The results for the relaxation times and the amplitudes are shown in figures 3.18a and 3.18b, respectively. It follows that the coefficients are not temperature dependent within experimental errors. In contrast to this, the $\tau_{1,T}$ time (black empty squares in figure 3.18a) decreases from its room temperature value to a value of $\tau_{1,T} \approx 315\,\mathrm{K}$ with decreasing temperature and remains approximately constant below $T \approx 175\,\mathrm{K}$, which is close to the Debye temperature of gold ($\Theta_D = 160\,\mathrm{K}$ [Ma et al., 2010]).

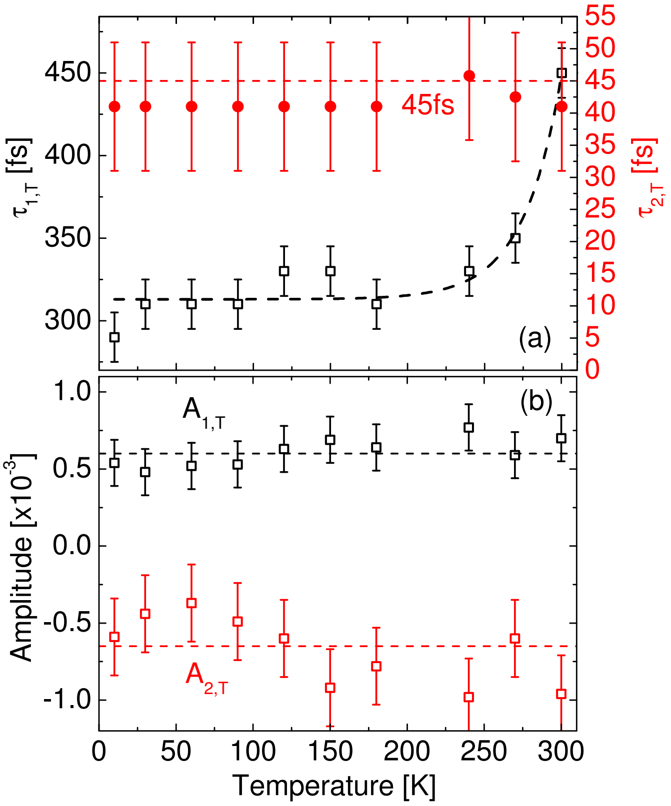

Figure 3.18: Temperature dependence of the relaxation times $\tau_{1,T}$ and $\tau_{2,T}$ (top) and the amplitudes (bottom) of the differential transmissivity data measured with a pump fluence of $46\,\mu\mathrm{J/cm}^2$. Top: The $\tau_{1,T}$-times (black squares) significantly decrease from its initial room-temperature value of $\tau_{1,T} = 450\,\mathrm{fs}$ (see figure 3.15) to a value of $\tau_{1,T} = 315\,\mathrm{fs}$ at low temperatures. The dashed line is a single exponential fit to the data points. Fitting the data with the appropriate $\tau_{1,T}$-times shows that the $\tau_{2,T}$-times (red dots) remain approximately constant at $\tau_{2,T} = 45 fs$. Bottom: Within error bars, a temperature dependence of the coefficients is not observed.

According to the TTM, $\tau_{1,T}$, which is connected to the relaxation of the electron gas excess energy, is supposed to be linearly dependent on the lattice temperature[17] for $T \gg \Theta_D$, while a $\propto 1/T_i^3$ increase is expected for $T \ll \Theta_D$ [Groeneveld et al., 1995]. However, for $T < \Delta T_e = 110\,\mathrm{K}$, this weak perturbation approximation loses its validity. Moreover, and more importantly, deviations from the TTM prediction have

---

[17] In the weak-perturbation regime, the pump induced rise of the lattice temperature can be neglected, so that it is approximately identical to the measured (external) temperature.

to be considered since the combination of low pump fluences and low temperatures strongly slows down the electron thermalization due to the Pauli exclusion.[18] Hence, the measured results must be explained in the picture of the NEM at low temperatures.

$\tau_{1,T}$ decreases linearly with the lattice temperature down to $T = \Theta_D = 160\,\mathrm{K}$ [Ma et al., 2010], which is still in accordance with the predictions of the TTM and can be explained by the decreased heat capacity of gold. Below this value however, the influence of the non-thermalized electron distribution and the low phonon occupation numbers become ever stronger increasing the electron-phonon relaxation times. This effect is superposed on the linear dependence at low temperatures so that $\tau_{1,T}$ reaches a plateau. The latter result contradicts the predictions of the TTM but is in accordance with experimental results of other groups, e.g., Groeneveld et al. [1995]. Since $\tau_{2,T}$ (red solid circles in figure 3.18a) is determined by the relaxation of short living holes far from E_F (see text above), the scattering probability is also expected to decrease with decreasing temperature, but cannot be measured with sufficient accuracy due to the limited temporal resolution of the setup of $\sim 40\,\mathrm{fs}$.

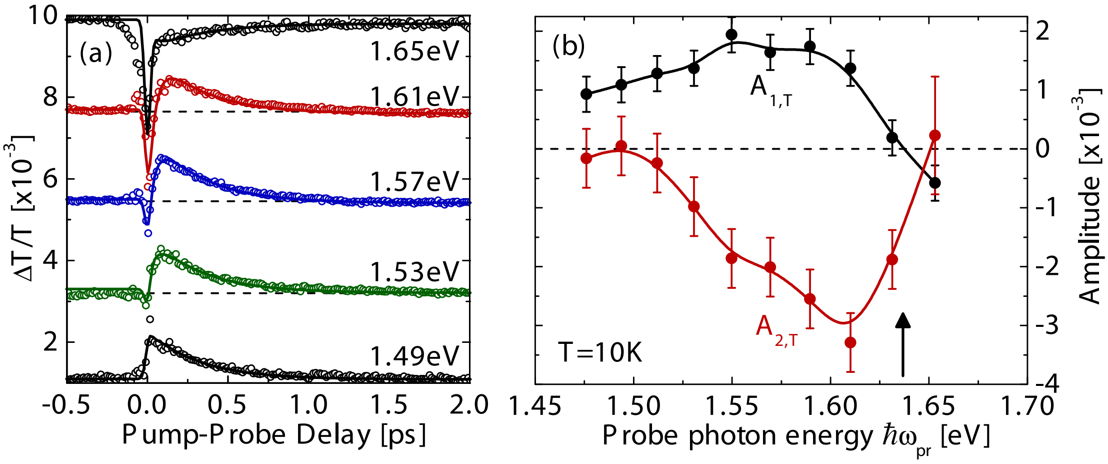

Figure 3.19: (a) Time resolved differential transmission signals for different probe photon energies $\hbar\omega_{pr}$ at $T = 10\,\mathrm{K}$. (b) The corresponding spectral dependence of the amplitudes $A_{1,T}$ and $A_{2,T}$ as obtained by fitting the signals with equation 3.10 (compare figures 3.16a and 3.16c).

Finally, in figure 3.19, the low temperature spectral dependence of the signal contributions ($T = 10\,\mathrm{K}$) are presented. The measurements have been performed with half the pump fluence of figure 3.16 ($60\,\mu\mathrm{J/cm}^2 \equiv \Delta T_e = 310\,\mathrm{K}$) by means of individual bandpass filters (spectral width: 20 meV) instead of the electrically tunable color filter that has been used before. Also the spectral width of the probe pulse was slightly decreased with a loss of intensity on the high energy side, which increases the experimental error (especially for $A_{2,T}$ at 1.65 eV, red solid circles in figure 3.19b) and limits the measurement range with respect to figure 3.16. The evolution of the signals with the probe photon energy $\hbar\omega_{pr}$ is given in figures 3.19a. The signals clearly show a change in sign, which is typical for a resonant behavior. $\tau_{1,T} = 315\,\mathrm{fs}$ has been used according to the results discussed in the context of figure 3.18. Figure 3.19b gives the corresponding fit results by means of equation 3.10.

Considering that the applied pump fluences of figures 3.19 and 3.16 are both in the low perturbation, i.e., the linear regime (at least for $T = 300\,\mathrm{K}$, see figure 3.15), the data for $T = 300\,\mathrm{K}$ is in agreement with figure 3.19b within experimental errors

---

[18] for "Pauli exclusion principle" see "electron-electron interaction" in Kittel [2004]

with respect to the magnitudes of the coefficients. This insensitivity of the amplitudes on the temperature is consistent with the results shown in figure 3.18. Except for small deviations, the general spectral behavior of the signal coefficients is maintained at $T = 10\,\mathrm{K}$ as well. Especially the position of sign change of $A_{1,T}$, which marks the probe SPP resonance energy ($\hbar\omega_{pr} \approx 1.64\,\mathrm{eV}$), and the corresponding minimum of $A_{2,T}$ ($\hbar\omega_{pr} \approx 1.62\,\mathrm{eV}$) are almost identical.

3.2.6 SPP Influence on the $\Delta\epsilon_1^{ib}$ Relaxation

In the context of figure 3.13 we have discussed the importance of SPPs for the amplitudes of the transient signals. Subsequently, the different components of these signals have been described and identified. Especially the second, exponential A_1-term of the phenomenological fit function 3.10 has been attributed to the changes of the real part of the interband dielectric permittivity $\Delta\epsilon_1^{ib}$. Remarkably, not only the amplitude but also the time constant of the relaxation of $\Delta\epsilon_1^{ib}$ depends on the presence of both, pump and probe, SPPs. Figure 3.20 is a semi-logarithmic view on figure 3.13b with the corresponding color code and labels for the polarization of pump and probe beams. The curves have been fitted with equation 3.10 considering only the respective coefficient $A_{1,T}$ and setting all other coefficients to zero in order to determine the correct relaxation times.

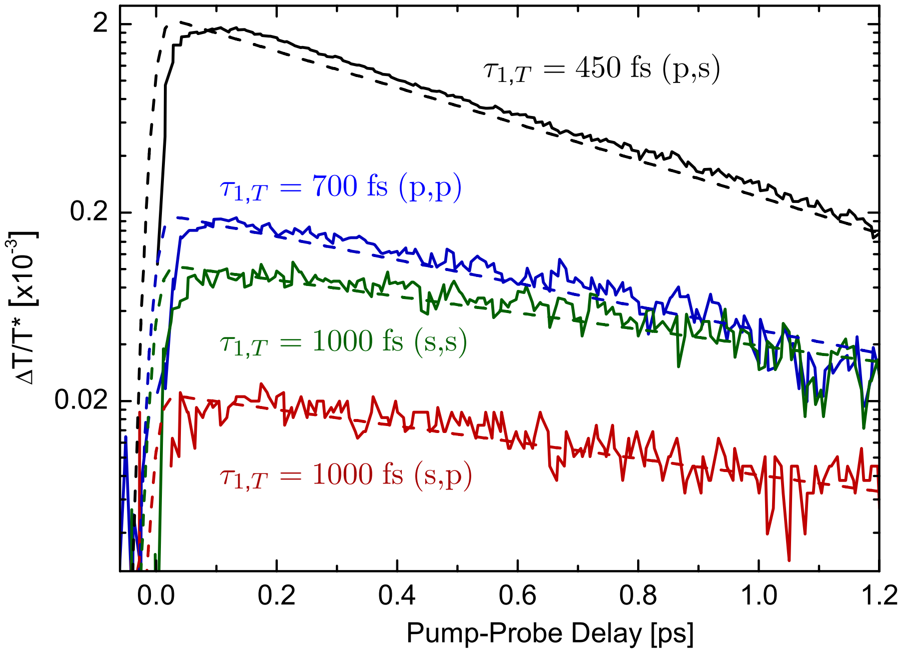

Figure 3.20: The dependence of the $\tau_{1,T}$ time on the (pump,probe) polarization on a semi-logarithmic scale at $T = 300\,\mathrm{K}$ (for colors and labels compare figure 3.13). The curves have been fitted with equation 3.10 but with only the coefficient $A_{1,T} \neq 0$, i.e., a single exponential. In the fully plasmonic case (p,s), the signal relaxes with the usual very fast time $\tau_{1,T} = 450\,\mathrm{fs}$. However, turning off either pump or probe SPPs by rotating the respective pulse polarization not only decreases the signal amplitude but significantly increases the relaxation time.

If both (linear) beam polarizations are aligned for the excitation of SPPs, the time constant takes the usual value of $\tau_{1,T} = 450\,\mathrm{fs}$ at room temperature. Rotating the probe polarization about 90° switches off the probe plasmon and the time constant increases to $\sim \tau_{1,T} = 700\,\mathrm{fs}$ (p,p). The absence of the pump plasmon instead increases the relaxation time even more drastically to $\sim \tau_{1,T} = 1000\,\mathrm{fs}$ (s,s). In the latter case, the additional absence or presence of the probe plasmon does not influence the relaxation time any further but only affects the signal amplitude (s,p).

In the measurements described above, the orientation of the grating, and wavevectors corresponds to that illustrated in figure 3.12. Rotating the sample about 90° effectively exchanges pump and probe orientations so that the projections of the pump and probe wavevectors on the SPP propagation direction, i.e., k_{SPP}, are now $k_{1\mathrm{x}} = 0$ and $k_{2\mathrm{x}} = k_0 \sin(\theta)$, respectively. For both polarizations set to SPP excitation (s,p), we again find $\tau_{1,T} = 450\,\mathrm{fs}$ (not shown here).

Obviously, there is a difference in the heat dissipation of the electron system for plasmonic excitation and/or detection. As can be seen in figure 3.10c, in contrast to the uniform heating in the case of non-resonant excitation, the plasmon field inherits so called “hot-spots” at the Au-BIG interface, whose distribution depends on the plasmon wavevector k_{SPP} and the order of the dispersion branch it belongs to. Most likely, the hot-spots can dissipate heat in the lateral direction, i.e., along the interface, more efficiently, which makes this thermalization process faster with respect to the dissipation of a uniform pump induced heat distribution (see figure 3.21a and 3.21b). This would explain the difference between p- and s- polarized pump configuration in figure 3.20.[19]

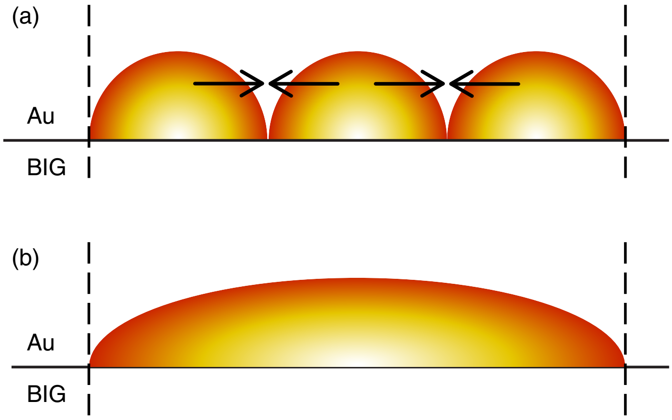

Figure 3.21: Schematical illustration of the optically induced heat distribution at the surface of the gold film in the case of (a) SPP excitation and (b) non-resonant excitation. The vertical dashed lines mark the laser spot area. The arrows in figure 3.21a represent the additional, lateral degree of freedom for the heat redistribution in the case of plasmonic excitation.

In section 3.2.2, the difference between conventional and SPP mediated detection during pump-probe experiments has already been discussed. Apart from the changes of the dielectric permittivity due to pump-induced inter- and intraband transitions, which determine the probed response of the material in conventional pump-probe methods, the probed response in SPP mediated detection is additionally sensitive to a pump-induced shift of the SPP resonance energy (see section 3.1.2). Clearly, both signal contributions reproduce the intrinsic redistribution and thermalization processes of the electron system. However, the difference between SPP mediated and conventional detection, i.e., between (p,s) and (p,p), might originate from the different processes contributing to the transient signals as explained in the following.

In the case of plasmonic excitation and non-plasmonic detection (p,p), the conventional detection feels the non-uniform heat distribution of figure 3.21a as a spatial average over the laser spot area. The lateral heat dissipation between the hot-spots thus contributes to the probed response in two different ways, i.e., a cooling of the hot spots and a heating of the gap in between. On average this corresponds to a slower overall cooling process and the probed signal reveals the averaged relaxation time. In case of plasmonic detection, the probe SPP is additionally modified by the change of the di-

---

[19] This mechanism was kindly proposed by B. A. Glavin from the Lashkaryov Institute of Semiconductor Physics, Ukraine

electric permittivity via the changes of the resonance condition 1.14. Here, similar to the case of conventional detection, the optical excitation leads to a non-thermal electron distribution, which leads to heat dissipation and a change of ϵ_m, which again produces an SPP energy shift and hence a transient signal. The changes of ϵ_m are largest at the positions of the pump hot-spots and weakest in between, i.e., for each value $\Delta\epsilon_m$, there is a different resonance condition and consequently a different energy shift of the probe plasmon resonance (the distribution of these shifts over the energy scale can be assumed rather narrow since they reflect only small deviations from the unperturbed plasmon dispersion). In the case of plasmonic detection, there is no reason to assume that the contributions of $\Delta\epsilon_m$ to the probed response, namely the relaxation of the excited electron distribution and the relaxation of the SPP shift, are described by the same relaxation time. On the contrary, the latter seems to relax significantly faster and gives a higher signal amplitude (compare curves (p,s) and (p,p) in figure 3.20).

At longer delays, the pump-induced distribution of heat and thus also of $\Delta\epsilon_m$ approach the uniform heat distribution of figure 3.21b and the relaxation time is expected to approach that of the (s,s) and (s,p) curves in figure 3.20, which both represent a non-plasmonic pump excitation, i.e., $\tau_{1,T} = 1000\,\mathrm{fs}$. Since the two times are close to each other, they are hard to distinguish at long delays in the measured signals. Moreover, the closer the signal amplitude approaches the background due to the increased lattice temperature, the stronger grows the influence of the background on the fit results.

3.3 Conclusions

We have presented a detailed description of a new magneto-plasmonic crystal, whose magneto-optical properties have been confirmed to combine a high magneto-optical response with simultaneously low optical absorption. By analyzing the transverse magneto-optical Kerr effect, we could show the influence of SPP excitation on the MPC's optical properties. Due to the enhanced optical transmission close to the Fano resonances, the effect could be measured in transmission geometry, which is advantageous with respect to the reflection geometry in view of device applications. Compared to numerically calculated values for the bare magnetic film,[20] SPP enhancements of the TMOKE amplitudes of at least three orders of magnitude could be achieved in sample 1. Even compared to calculations for an MPC sample under non-resonant excitation conditions, the enhancement still amounts to one order of magnitude.

In accordance with the literature, our results show that the bismuth concentration strongly influences the material's optical response through the gyration g. Since the δ value and the specific Faraday rotation are both proportional to g, the former could theoretically reach values above 0.2 by choosing an appropriate bismuth substitution level. Much larger bismuth concentrations than in sample 1 are found in compositions of $\mathrm{Bi_3Fe_5O_{12}}$, which show a specific Faraday rotation of 6° at $\lambda = 630\,\mathrm{nm}$ (compare table 3.1). By analyzing samples with the appropriate high amount of bismuth content, we could observe amplitudes of more than $10\,\%$.

The TMOKE has been demonstrated to be highly selective, with enhancements of the effect only occurring close to the excited SPP modes of the structure. Since the optical energy is stored in sub-wavelength volumes via SPP excitations and the effect has been shown to originate solely from the surface of the magnetic films and not from the bulk material, the design has the prospect of miniaturization down to the nanometer

---

[20] The theoretical modeling has been performed by V. I. Belotelov from the Moscow State University, Russia.

regime to be incorporated into modern on-chip solutions. The sensitivity of the TMOKE to properties of the magneto-plasmons, e.g., their direction of propagation, might be exploited, e.g., as a tool for probing surface plasmons and the complete characterization of plasmonic nanostructures.

Our results illustrate the importance for applications in both, reflection and transmission geometry. With respect to power consumption, it is advantageous that the observed TMOKE signals can be achieved with low magnetic fields $\leq 100\,\mathrm{mT}$ due to small saturation fields of the magnetic films. By means of altering the angle of light incidence onto the film or by adjusting the grating parameters, the effect can be shifted nearly arbitrarily into energy ranges accessible to the currently available light source.

In the second part of this chapter, the MPC structures have been exploited to analyze ultrafast electronic processes in the gold layer that turn out to be strongly enhanced by SPP excitations. The optical properties of the MPC can be manipulated by femtosecond lasers on time scales well below one picosecond by creating a transient non-thermal electron distribution in the vicinity of the Fermi energy. In differential transmission and reflection experiments, changes on the order of $6 \cdot 10^{-3}$ could be achieved with pump fluences $\leq 120\,\mu\mathrm{J/cm}^2$. The transients relax with a characteristic time constant of 450 fs.

An extensive study of the signals at different excitation power densities, temperatures and photon energies led to a detailed understanding of the relaxation processes inside the electron system. The results have been compared to the predictions of the well established two-temperature model. The obvious contradictions to this model show up the need of corrections in the case of non-thermalized electron distributions, which are addressed in the context of the non-thermal electron model (NEM). The essential importance of SPPs in the origin of the observed signals could be unambiguously verified by means of polarization resolved measurement and by the Kramers-Kronig behavior of the transients around the SPP resonance energy in the spectral domain, which is far off the intrinsic d-band to Fermi transition in gold. The obtained results have been evaluated by a phenomenological fit function based on linear response theory derived for the case of pump-probe experiments. This function and its different components are justified within a comprehensive microscopic picture of the relaxation processes described in the text.

A close evaluation of the obtained signals revealed a dependence of the relaxation of the interband contribution to the real part of the dielectric constant, $\Delta\epsilon_1^{ib}$, on the presence of surface plasmons in the excitation and/or detection by the pump and probe beam, respectively. This effect has been suggested to originate from the difference of the pump-induced heat distribution and different contributions to the transient response in the case of present or absent SPP resonances. Although the underlying mechanism is still under debate, an understanding could provide ways to further speed up the relaxation.

The presented method has been shown to be straight forward and intrinsically ultrafast. Since magnetic order is not required it is also independent of exotic materials, such as rare-earth elements, which are used in magnetic films in order to enhance their magneto-optical response. Further, the method is vastly adjustable to a broad range of wavelength regions by choice of the respective dielectric/metal combination and experimental conditions.

The device dimensions of both presented approaches are basically limited by the spot size of the laser sources that drive the processes. The latter could be reduced by means of the previously mentioned achievements in on-chip sub-wavelength lasing.[21] Hence, our results have a high potential for ultra-compact, femtosecond applications, such as all-optical switches and modulators. In this respect, recent results on magneto-optical effects, such as the inverse Faraday effect, show that the TMOKE could be transfered into the ultrafast regime with possible all-optical applications in the THz range (see section 5.1.4). The concept of MPCs can be used for plasmonic biosensors, magnetic field sensors and magnetic read heads. Moreover, the enhancement of magneto-optical phenomena by SPP excitation is not limited to the TMOKE but can most likely be used for other magneto-optical effects, such as the Faraday effect, the polar or the longitudinal Kerr effect.

---

[21] For nanoscale sources of coherent light, the device dimension would be limited by grating parameters, such as the minimum number of illuminated grating periods. The more grating periods are illuminated, the smaller are the uncertainties in the grating vector Λ and thus in the resonance condition for the angle of the incident light...

Chapter 4

Strongly Correlated Systems: The Mott Insulator $YMnO_3$

In this chapter, we focus on optically induced ultrafast dynamics in the Mott insulator $YMnO_3$. The material exhibits a multiferroic character, i.e., it has simultaneously ferroelectric and antiferromagnetic properties at sufficiently low temperatures (below the Curie temperature $T_C = 913\,\mathrm{K}$ and below the Néel temperature $T_N = 75\,\mathrm{K}$, respectively [Lee et al., 2008; Smolenskiĭ and Chupis, 1982]). While ferroelectric substances possess a stable, spontaneous polarization that can be controlled by means of an external electric field, antiferromagnets have ordered magnetic moments but no spontaneous magnetization since the former cancel within each unit cell due to their opposite orientations [Eerenstein et al., 2006]. Above T_N, $YMnO_3$ is ferrimagnetic with incomplete cancellation of the magnetic moment within each unit cell. In that case, the net magnetization can be controlled, e.g., via external magnetic fields. Besides the multiferroic properties, $YMnO_3$ also shows large second and third order optical nonlinearities [Fiebig et al., 2000; Fröhlich et al., 1998; Kimel et al., 2001b; Wang et al., 2013].

In the presented experimental results, we examine the interaction of thin slabs of $YMnO_3$ with laser pulses of femtosecond duration with a view to ultrafast electronic processes and their usefulness in optical modulators and switches. Especially the charge-transfer electronic transition $\Gamma_1 \rightarrow \Gamma_5$ will be shown to exhibit not only a sub-picosecond charge carrier relaxation but an even faster relaxation of the optically induced angular momentum on the order of 10 fs between the doubly degenerate states of Γ_5 symmetry.

4.1 Ultrafast Electron Momentum Relaxation and Dephasing

The following measurements have been performed by means of the femtosecond pump-probe technique described in section 2.1. The experiments focus on the signals of photo-induced rotation and ellipticity angles of the initially linear probe beam polarization in order to gain information about the transient response of the material. The corresponding methods have been elucidated in section 2.1.5. For polarization sensitive and differential reflection measurements, a PEM modulation at 50 kHz and a chopper modulation at 2 kHz have been used, respectively. Due to the pulse shaping units in the setup, the pulse could be compressed to a duration of 17 fs at the position of the sample. Spectrally resolved signals have been obtained by cutting out spectral regions of the original pulse by means of bandpass filters. In that case, the pulse duration increases to 34 fs. Otherwise, the pulse photon energy is centered around 1.55 eV. The pump fluence amounts to 60 μJ/cm^2. The pump and probe beams are focused on the sample to spots of 20 μm and 15 μm, respectively. Low temperature measurements have been performed by means of a liquid helium continuous-flow cryostat. The samples are polished plane-parallel crystals of the hexagonal manganite YMnO$_3$ with their surface normal along the symmetry c-axis ($\equiv z$-axis) prepared from flux-grown single crystals.

4.1.1 Charge Carrier Versus Momentum Relaxation

As discussed in section 1.2.1, the optical excitation of YMnO$_3$ with a photon energy close to the resonance around 1.6 eV induces an electronic charge transfer transition from the hybridized oxygen-manganese O$^{2-}(2p)$-Mn$^{3+}(3d)$ states to the manganese Mn$^{3+}(3d_{3z^2-r^2})$ states. This transition is illustrated schematically in figure 4.1a, where $|g\rangle$ is the Γ_1 ground state and $|x,y\rangle$ is the doubly degenerate Γ_5 excited state. The population relaxation time t_1 describing the charge carrier relaxation from the excited states to the ground state can be obtained from the differential reflectivity. The population of the excited states by the pump pulse modifies the probe absorption and thus its reflectivity due to a depopulation of the ground state. Consequently, the relaxation of the probe's differential reflectivity images the re-population of the ground state yielding the characteristic charge carrier relaxation time t_1. The latter has been determined by fitting the differential reflectivity shown in figure 4.1b with equation 3.10 taking into account only one single exponential contribution. At $T = 10$ K this time amounts to $t_1 = 500$ fs, which will be shown to be much longer and well distinguishable with respect to the coherent electron dynamics. The coherent oscillations at 31 GHz due to acoustic phonon modes, which was recently found by Jang et al. [2010] in the differential reflectivity of hexagonal YMnO$_3$, is not related to the signals discussed here, since the former occur on much longer time scales.

When measuring such signals as the rotation and ellipticity of the probe polarization, transient contributions from the charge carrier relaxation $|x,y\rangle \rightarrow |g\rangle$, which affect the intensity of the reflected probe beam, are equally divided onto both channels of the balanced photo-receiver and hence cancel each other (see section 2.1.5). Instead of the intensity, these signals reflect purely changes of the polarization induced by perturbations of ϵ_1 and ϵ_2, respectively, as elucidated in sections 1.2.2 and 1.2.3. The corresponding relaxation processes are connected to a momentum redistribution and dephasing among the excited sub-levels, which are pump-induced coherent superpositions of $|x\rangle$ and $|y\rangle$ ($|+\rangle$ and $|-\rangle$). The transitions $|x\rangle \leftrightarrows |y\rangle$ ($|+\rangle \leftrightarrows |-\rangle$) are hence determined by a coherence time τ_R. The latter is commonly referred to as the Raman coherence time due to the similarity to the optically induced coherence as known from coherent Raman spectroscopy [Ferrio and Steel, 1998].

Experimental data showing these polarization sensitive signals obtained with linear and circular excitation of hexagonal YMnO$_3$ samples are given in figure 4.2. The curves have been measured at different temperatures from $T = 10$ to 300 K with optical pulses of 17 fs duration centered around 1.55 eV photon energy. The observed dynamical response is at least one order of magnitude faster than the previously shown carrier relaxation dynamics in figure 4.1b. The rotation of the polarization axis due to excitation with linearly polarized light ("linear rotation") and the transient change of the ellipticity angle due to excitation with circularly polarized light ("circular ellipticity") have almost symmetric Gaussian shapes closely following the pump-probe cross-correlation function. The two remaining signals, on the other hand, are strongly asymmetric with a sign change within the temporal range of the pulses' cross-correlation, which suggests electronic

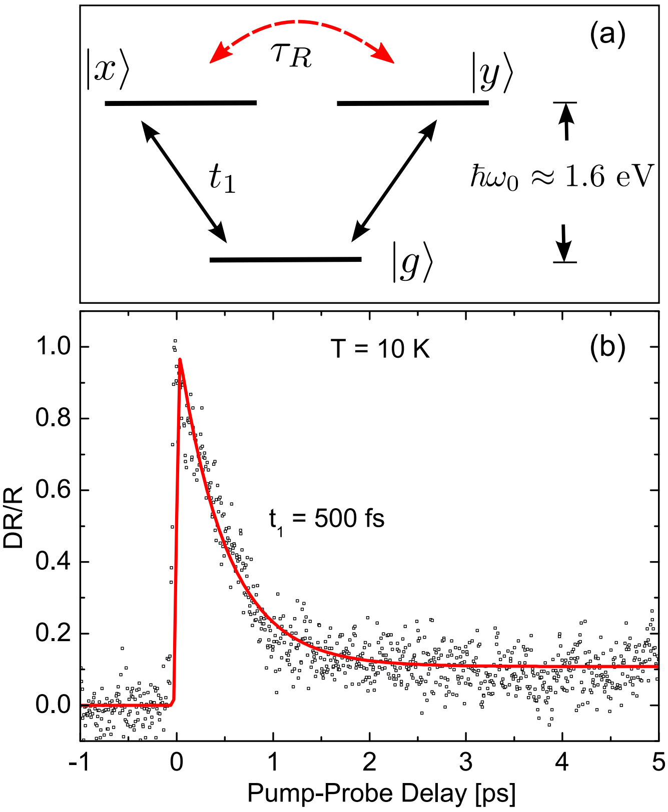

Figure 4.1: (a) Schematical energy-level diagram for the dipole-allowed optical transition $\Gamma_1 \rightarrow \Gamma_5$ (solid arrows) between the hybridized $O^{2-}(2p)$-$Mn^{3+}(3d)$ states ($|g\rangle$ is the ground state) and the $Mn^{3+}(3d_{3z^2-r^2})$ states ($|x\rangle$ and $|y\rangle$ are the degenerate excited states). The $|x\rangle \leftrightarrows |y\rangle$ ($|+\rangle \leftrightarrows |-\rangle$) transitions are characterized by the Raman coherence time τ_R. The $|g\rangle \leftrightarrows |x,y\rangle$ transitions are characterized by the population relaxation time t_1. (b) Dynamics of the photo-induced differential reflectivity in $YMnO_3$. The points are experimental data, the solid line is a fit to the data with the single exponential part of equation 3.10 [Pohl et al., 2013b].

processes on time scales significantly shorter than the latter, i.e., shorter than $17\,\text{fs} \cdot \sqrt{2} = 24\,\text{fs}$.

Changes with respect to the temperature are negligibly small and originate from the temperature shift of the 1.6 eV absorption band [Choi et al., 2008b]. Especially around the Néel temperature $T_N = 75\,\text{K}$, no anomalous effects could be observed although, e.g., Shih et al. [2009] report on a significant influence of the ferri- to antiferromagnetic phase transition on the differential reflectivity in the similar hexagonal compound $HoMnO_3$. The absence of temperature effects further supports the proposed model described in the context of figure 4.1a stating that the relaxation of the polarization is exclusively related to a redistribution between the excited states and not to the $|g\rangle \leftrightarrows |x,y\rangle$ transitions. The former are quite insensitive to the ground electronic states responsible for the magnetic ordering and consequently do not “feel” the phase transition around the Néel temperature.

The amplitudes of the transient signals are well in the milliradian regime, which is remarkably high considering the low pump fluence of $60\,\mu\text{J/cm}^2$. Especially since the observation of comparable photo-induced phenomena in other magnetically ordered materials typically requires the use of amplified pulses from Ti:sapphire lasers with several orders of magnitude higher pump fluences [Kirilyuk et al., 2010]. We attribute both, the short time scale of the relaxation processes and the high amplitudes, to the large on-site Coulomb forces acting on the charge carriers. The strong correlation of the spin, charge and orbital degrees of freedom in hexagonal $YMnO_3$ results in unusually large perturbations of the crystal’s optical properties by optical excitation of the electron system with only moderate pump fluences. Furthermore, the electron-electron interactions lead to efficient dephasing channels for the electron momenta resulting in the femtosecond relaxation times.

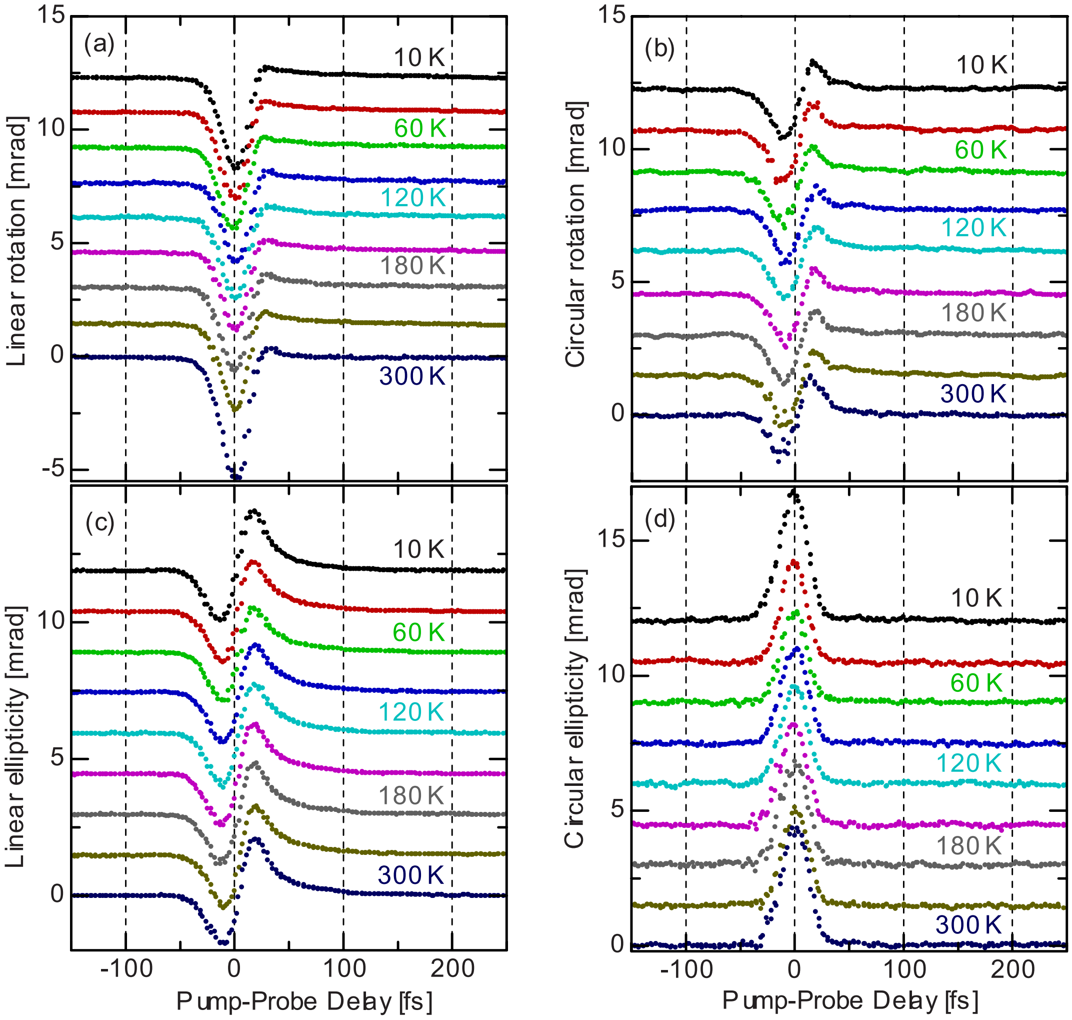

Figure 4.2: Temporal behavior of the photo-induced rotation and ellipticity for linearly and circularly polarized pump excitation at different temperatures from $T = 10$ to 300 K. The rotation θ of the polarization ellipse due to linearly polarized excitation is denoted as "linear rotation". The change of the ellipticity angle Ψ induced by circularly polarized excitation is denoted by "circular ellipticity", and so on... [Pohl et al., 2013b]

4.1.2 Determination of the Raman Coherence Time τ_R

In the experimental results discussed here, the laser pulses are incident along the 6-fold symmetry axis ($\equiv z$-axis) of the hexagonal YMnO$_3$. Since the light is necessarily polarized perpendicular to the latter, this situation is characterized by optical isotropy for rotations of the polarization about the z-axis with a uniform (equilibrium) refractive index $n_\perp^2 = \epsilon_\perp$ (see equation 1.26). A probe beam polarized linearly along $\boldsymbol{x}$ will thus not experience any rotation θ of its plane of polarization upon reflection in the absence of pumping, since θ is defined by [Gridnev, 2011]

$$\theta = \frac{1}{I_{pr}^{(r)}} \Re \left(\int_{-\infty}^{\infty} dt E_x^{(r)}(t) E_y^{(r)}(t) \right), \tag{4.1}$$

where $I_{pr}^{(r)}$ is the integral intensity of the reflected probe pulse. Only if a second (pump) pulse, having a non-vanishing y-component, interacts with the material, a rotation can be measured. The interplay of both, pump and probe pulses, accounts for the y-component $E_y^{(r)}$ of the reflected probe polarization via the mutually induced third-order polarization $P_y^{(3)}(t)$ according to

$$\theta = \frac{2\pi\omega_{pr}}{cI_{pr}} \Im \left(R_0^{-1} \int_0^\infty dz \int dt E_0^*(t) f(z) P_y^{(3)}(z,t) \right), \tag{4.2}$$

where R_0 is the equilibrium reflection coefficient at the probe photon energy $\hbar\omega_{pr}$ and $f(z)$ is a function describing the damping of the amplitude of the probe electric field $E_{pr}(t,z) = E_0(t) f(z) \exp(-i\omega_{pr}t)\boldsymbol{x}$ inside the sample. With equation 1.43, the nonlinear macroscopic polarization $P_y^{(3)}(t)$ can be expressed via the microscopic electric dipole moment μ induced by the $\Gamma_1 \to \Gamma_5$ charge-transfer interband transition from the ground state $|g\rangle$ to the excited state $|y\rangle$ due to the y-component of the pump polarization:

$$P_y^{(3)}(t) = \sum_{gy} \rho_{gy}(t) \mu_{yg}^{(3)}. \tag{4.3}$$

The temporal dynamics are entirely determined by the time dependence of the density matrix $\hat{\rho}(t)$, which must be calculated via the Liouville-van Neumann equation 1.45 with the full Hamiltonian of the system. For a material system as sophisticated as the strongly correlated Mott insulator YMnO$_3$, it is not sufficient to truncate the terms of the Hamilton operator as has been done in section 1.2.4 for exemplary reasons. Hence, finding analytical equations similar to 1.46 in order to find a solution to the problem is far from trivial (if possible at all) and beyond the scope of this work.

However, for the case of circular optical anisotropy, Linder and Sham [1998] performed a respective calculation for the complex Faraday rotation in magnetic semiconductor quantum wells, which can be modified to describe the complex rotation $\Theta = \theta + i\Psi$ in reflection geometry as is the case in our experiments [Kimel et al., 2001a]. The calculation yields an expression for the complex rotation of the two circular normal modes $E_{\sigma=+1}$ and $E_{\sigma=-1}$ of the linearly polarized probe beam in dependence of the diagonal elements of the density matrix $n_{ff'}$, i.e., the populations of electrons ($f = s$) and holes ($f = j$) created by a pump induced interband transition, where f is the z-projection of the total angular momentum:

$$\begin{aligned} \theta + i\Psi \propto \sum_{s,j} \sigma \int_{-\infty}^{\infty} dt \Big\{ & E_\sigma(t) |\mu_{js}|^2 |\Psi(0)|^2 \\ & \times \int_{-\infty}^{t} dt' E_\sigma^*(t') \left(e^{i\Delta_{js}(t-t')} [n_{ss}(t') + n_{jj}(t')] \right) \Big\}. \end{aligned} \tag{4.4}$$

Here, $\sigma = s - j = \pm 1$ is the angular momentum of the photons involved in the transition with electric dipole moment μ_{js},[1] $\Psi(0)$ is the exciton wave function at zero relative distance and $\Delta_{js} = (1/\hbar)(E_{js} - \hbar\omega_{pr})$. From equation 4.4 one can see that Θ originates purely from an asymmetric optical orientation of the coherent carrier densities $n_{ss}(t) + n_{jj}(t)$ with different angular momentum projection f. Although we still lack the explicit form of these carrier densities, it is reasonable to approximate their temporal behavior by a linear combination of two main contributions, one being instantaneous with the pulsed excitation while the other relaxes single exponentially with time τ_R.

$$n_{ss}(t') + n_{jj}(t') = a\delta(t - t') + be^{-(t-t')/\tau_R}, \tag{4.5}$$

---

[1] For $s - j \neq \pm 1$, μ will be zero, due to the selection rules for optical transitions.

$\delta(t-t')$ is the Dirac Delta function. Since the electric field can be assumed to have a Gaussian shape $\propto \exp[-t^2/(w/\sqrt{2})^2]$ with pulse duration $\tau_D = \sqrt{2\ln 2}w$,[2] substituting expression 4.5 into equation 4.4 and performing the integration leads to terms equivalent to equations 2.6 and 2.7, respectively. Consequently, we arrive at the analytical expression for the rotation θ and ellipticity Ψ

$$\theta + i\Psi = A_\sigma \exp\left(-\frac{t^2}{w^2}\right) + B_\sigma \exp\left(\frac{w^2}{4\tau_R^2} - \frac{t}{\tau_R}\right)\left[1 - \mathrm{erf}\left(\frac{w}{2\tau_R} - \frac{t}{w}\right)\right] \tag{4.6}$$

with the complex coefficients $A_\sigma = A'_\sigma + iA''_\sigma$ and $B_\sigma = B'_\sigma + iB''_\sigma$. The first term on the right hand side closely follows the pump-probe cross-correlation function. The second term gives a single exponential contribution whose relaxation is determined by the Raman coherence time τ_R.

Although equation 4.4 has been derived for the case of circular optical anisotropy, it is straightforward to transfer the results to the case of linear anisotropy. For the latter, population densities do not represent states with different angular momentum projection J_z but rather with different alignment of their angular momentum distribution in the xy-plane (see section 1.2.3). Hence, the approximation 4.5 is equally reasonable for the carrier densities of the $|x\rangle$ and $|y\rangle$ states, respectively, leading to an expression for Θ, which is formally identical to 4.6 except for different amplitudes $A_\|$ and $B_\|$.

Since $w = 1/\sqrt{2\ln 2}\tau_D$ is determined by the pulse duration, which can be measured and modified during the experiments, the only fitting parameters in expression 4.6 are the amplitudes $A_\|$ and $B_\|$ (A_σ and B_σ) and the Raman coherence time τ_R describing the relaxation between the degenerate excited states $|x\rangle$ and $|y\rangle$ ($|+\rangle$ and $|-\rangle$). As has already been mentioned before, the relaxation processes are faster than the shortest pulse durations in our experiments. This reduces the accuracy, with which the time τ_R can be determined and is in fact only possible due to different signs in the amplitudes A_σ and B_σ ($A_\|$ and $B_\|$) of the linear ellipticity and the circular rotation signals. However, τ_R should be independent on τ_D since the pulse duration does not influence the momentum relaxation mechanisms of the material. This circumstance has been exploited for a more accurate determination of τ_R by performing fits to the linear and circular signals under excitation with pulses of different temporal widths of 17 fs and 34 fs, respectively. Exemplary results and the corresponding fit curves are shown in figures 4.3a-4.3d.

It should be noted that the rotation and ellipticity signal pairs have each been measured simultaneously, e.g., linear and circular rotation or linear and circular ellipticity, respectively. Either one of the signals closely follows the pump-probe cross-correlation function and is thus symmetrically centered around the position of zero pump-probe delay while the other has a strongly asymmetric shape. Hence, the symmetric signal determines the position on the time delay ($\equiv x$-) axis for both signals of a respective pair with high precision.[3] The exact knowledge of the x-axis data is of absolute importance for the accuracy of τ_R since already offsets of few femtoseconds strongly influence the fit results.

The accordingly prepared signals in figures 4.3a-4.3d have been fitted with equation 4.6 yielding a Raman coherence time of $\tau_R = 10 \pm 4$ fs for both, circular and linear,

---

[2] w belongs to the pump-probe cross-correlation, which is proportional to $\exp(-t^2/w^2)$.

[3] Further information on the pump-probe delay data of the signals has been obtained by observation of the "coherent artifact", i.e., interference patterns originating from the inevitable constructive and destructive interference of pump scattered light with the probe light entering the detector. Since the envelope of this interference pattern is proportional to the pump-probe cross-correlation function, it is symmetrically centered around zero delay and can be used to calculate the time axis values from the length units of the delay line.

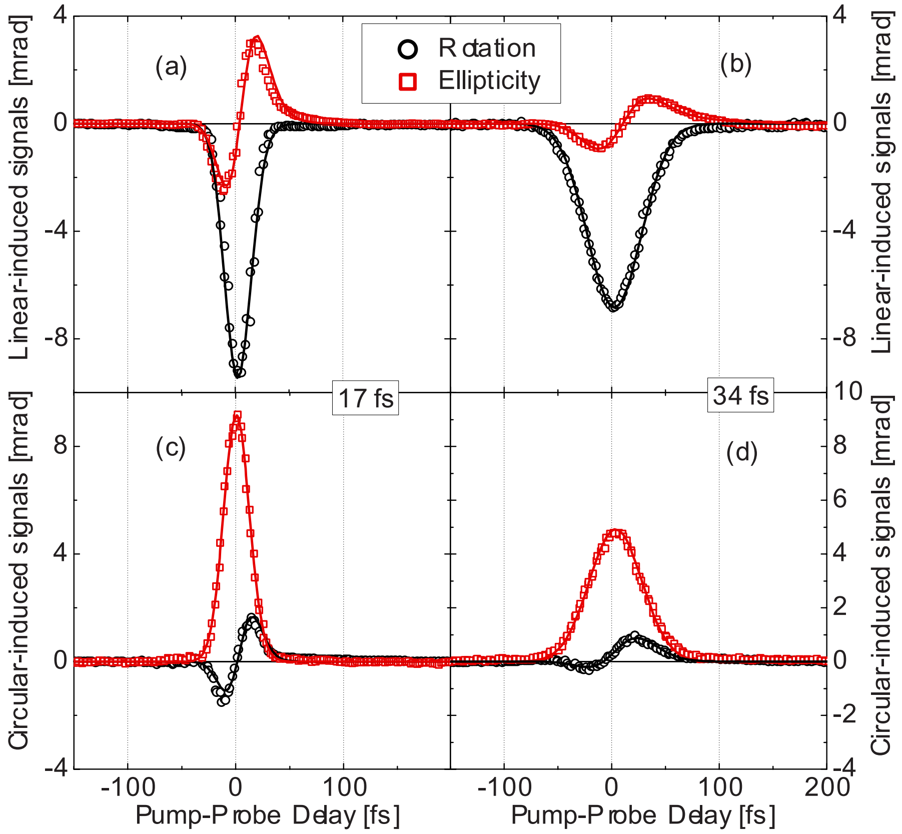

Figure 4.3: Linear and circular rotation (circles) and ellipticity (squares) data obtained with pulse durations of (a)+(c) 17 fs and (b)+(d) 34 fs. The solid lines are fits to the data with equation 4.6. The best fit is obtained with a uniform Raman coherence time $\tau_R = 10 \pm 4$ fs [Pohl et al., 2013b].

anisotropies and consistently for both pulse durations. The fits are in good quantitative agreement with the measured data. Strikingly, the linear rotation and ellipticity exhibit a dissipative and dispersive lineshape, respectively, while the situation is reversed with the circular signals. Since the former signals derive from changes in ϵ_2 and the latter from changes in ϵ_1 of the tensor 1.26, the opposite behavior of the lineshapes is a direct consequence of the form of equation 1.31, where real and imaginary parts of the two contributions of ϵ_1 and ϵ_2 are reversed as well.

4.1.3 Spectrally Resolved Signals

In order to gain a more detailed understanding of the physical mechanisms that lead to the observed complex rotation signals, we have to study the material under the influence of an external perturbation different from the ones applied until now. In our case, this is done by exciting the sample with femtosecond pulses of narrow spectral width with different photon energies by means of the liquid crystal pulse shaper unit (see figure 2.1 and section 2.1.2). The latter is not only able to alter the spectral phase of the pulse's frequency components, but also their intensity. That way, a transmission "mask" can be superposed on the initially broad pulse spectrum cutting out spectral ranges with well defined widths and central photon energies. The masks applied in the following experiments are shown in figure 4.4. Due to the Fourier relation between the spectral and the time domain, the pulse duration increases to 34 fs after applying the transmission masks while the spectral width decreases to ∼ 50 meV.

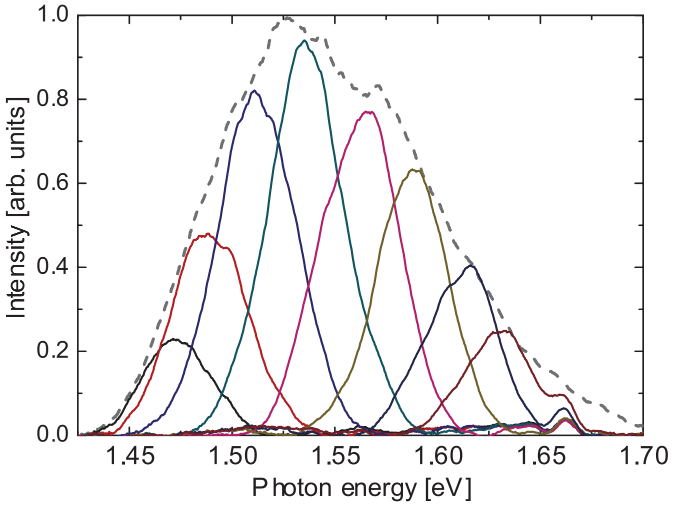

Figure 4.4: Spectral shapes of the pulse intensities after application of transmission filters (solid lines) on the original pulse spectrum (dashed line) by a liquid crystal pulse shaper. While the spectral width of the masks decreases to ∼ 50 meV with respect to the original pulse, the temporal width increases to ∼ 34 fs.

The so obtained spectral dependence of the linear and circular rotation and ellipticity are presented in figure 4.5. Since the temperature has only negligible influence on the signal shape as shown previously, the signals have been measured exclusively at room temperature. The transmission masks cover the energy range from 1.460 eV to 1.636 eV. Obviously, the resulting changes in the temporal dynamics of the linear rotation and circular ellipticity concern only the amplitude of the Gaussian shaped signals showing a maximum around ∼ 1.554 eV and ∼ 1.540 eV, respectively. At the same photon energies, the corresponding signals of linear ellipticity and circular rotation both exhibit a sign change of their amplitude, which is characteristic for a resonant behavior.

The understanding of the origin of the underlying resonances requires a detailed knowledge of the band structure of hexagonal YMnO$_3$, which is in general more complicated than the discussed O($2p$)-Mn($3d$) → Mn($3d$) transition. However, it is possible to connect the experiment with the microscopic theory by means of the dielectric permittivity tensor. Following the discussion in section 1.2.1, only electric dipole transitions need to be considered. For materials with N saturated spin systems per unit volume in orbital singlet ground states $|g\rangle$, whose dielectric permittivity tensor has the form 1.26, the pump (pp) induced contribution to the diagonal elements reads [Kahn et al., 1969]

$$\begin{aligned}\epsilon_\perp &= 1 + \sum_{e,\nu} \epsilon_{\perp,e(\nu)} \\ &= 1 + \frac{4\pi N e^2}{m} \sum_{e,\nu} f_{ge(\nu)} \frac{\omega^2_{ge(\nu)} - \omega^2_{pp} + \Gamma^2_{ge(\nu)} - 2i\omega_{pp}\Gamma_{ge(\nu)}}{(\omega^2_{ge(\nu)} - \omega^2_{pp} + \Gamma^2_{ge(\nu)})^2 + 4\omega^2_{pp}\Gamma^2_{ge(\nu)}}, \end{aligned} \tag{4.7}$$

where the summation is performed over all excited states $|e\rangle$ with degeneracy ν. m is the electron mass, $\omega_{ge(\nu)}$ is the resonance frequency of the respective transition from the ground state, $\Gamma_{ge(\nu)}$ is the spectral width of the transition and

$$f_{ge(\nu)} = (2m\omega_{ge(\nu)}/\hbar)|\langle g| x |e(\nu)\rangle|^2 \tag{4.8}$$

is the respective oscillator strength with the pump beam polarized in the x direction. In this case, the only non-vanishing transition matrix element occurs for $|e\rangle \equiv |x\rangle$ and since the pump photon energy is almost in resonance with the $\Gamma_1 \to \Gamma_5$ transition from the ground state we need only consider this transition's doubly degenerate excited states

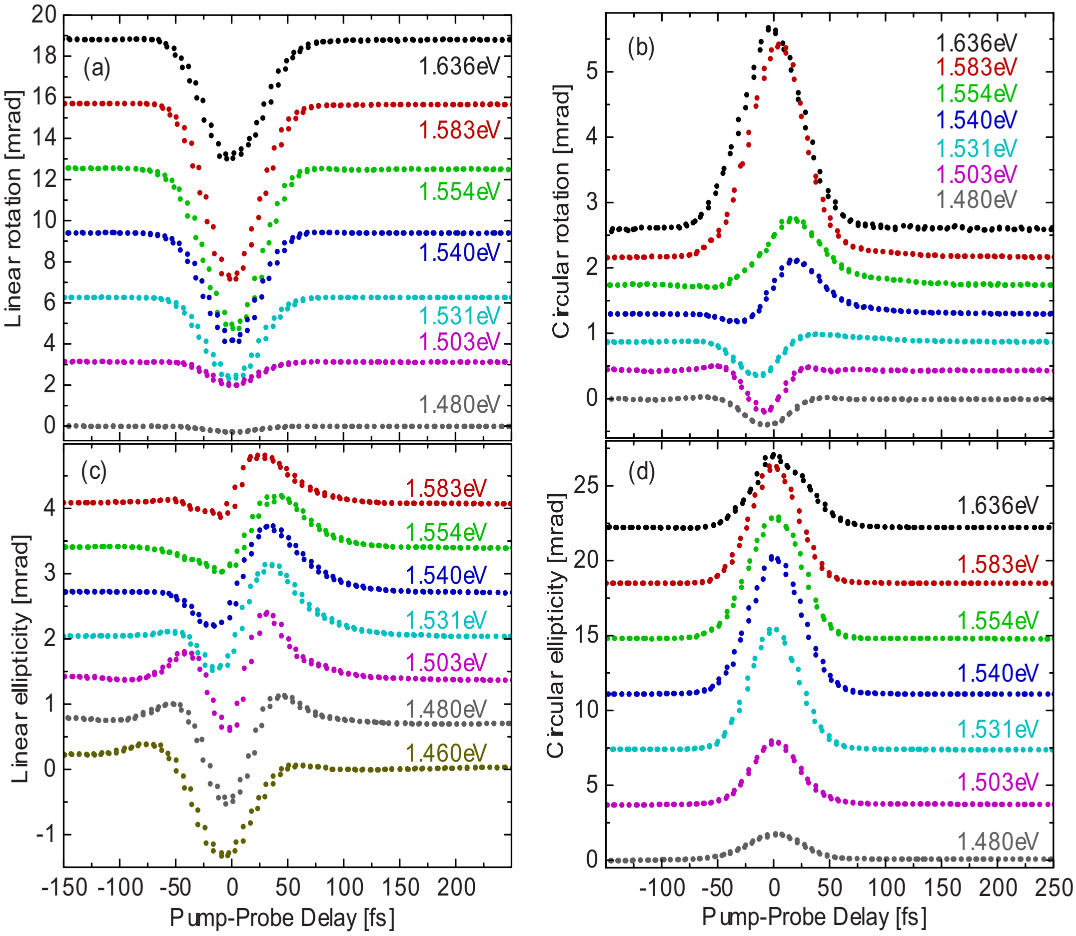

Figure 4.5: Spectral dependence of the (a)+(c) linear and (b)+(d) circular anisotropies at $T = 300\,\mathrm{K}$ in the energy range between 1.460 eV and 1.636 eV. Spectral resolution has been established by modification of the spectral pulse shape via a liquid crystal pulse shaper [Pohl et al., 2013b].

and can drop the subscript g in the following. For materials, such as $\mathrm{YMnO_3}$, for which $|\epsilon_\perp - 1| \ll 1$ is not valid at optical frequencies, equation 4.7 requires corrections due to local-field effects. However, it still reproduces the microscopic picture in a qualitative sense.

Similarly, for a circular polarization of the pump pulses, the contributions to the non-diagonal elements of the permittivity tensor read

$$\begin{aligned}\epsilon_1 &= \sum_\nu \epsilon_{1,e(\nu)} \\ &= \frac{2\pi N e^2}{m} \sum_\nu \frac{f_{-e(\nu)} - f_{+e(\nu)}}{\omega_{pp}^2 - \omega_{e(\nu)}^2 - \Gamma_{e(\nu)}^2 - 2i\omega_{pp}\Gamma_{e(\nu)}} \frac{\omega_{pp} - i\Gamma_{e(\nu)}}{\omega_{e(\nu)}}. \end{aligned} \tag{4.9}$$

Here,

$$f_{\pm e(\nu)} = (m\omega_{e(\nu)}/\hbar) |\langle g| (x \pm iy) |e(\nu)\rangle|^2 \tag{4.10}$$

is the oscillator strength between the ground state and the circular eigenstates $|e\rangle \equiv |\pm\rangle$, respectively. Without the spin-orbit interaction, the electron system is not able to distinguish between the two senses of circular polarization. It is only the alignment of the spin of the electrons that breaks the time-inversion symmetry in the system. In the absence of this coupling mechanism both, the resonance frequencies $\omega_{e(\nu)}$ and the oscillator strengths $f_{\pm e(\nu)}$, are independent of ν and $\sum_\nu (f_{-e(\nu)} - f_{+e(\nu)}) = 0$. Hence, spin-orbit interaction is the source of the dominant contribution to ϵ_1.[4]

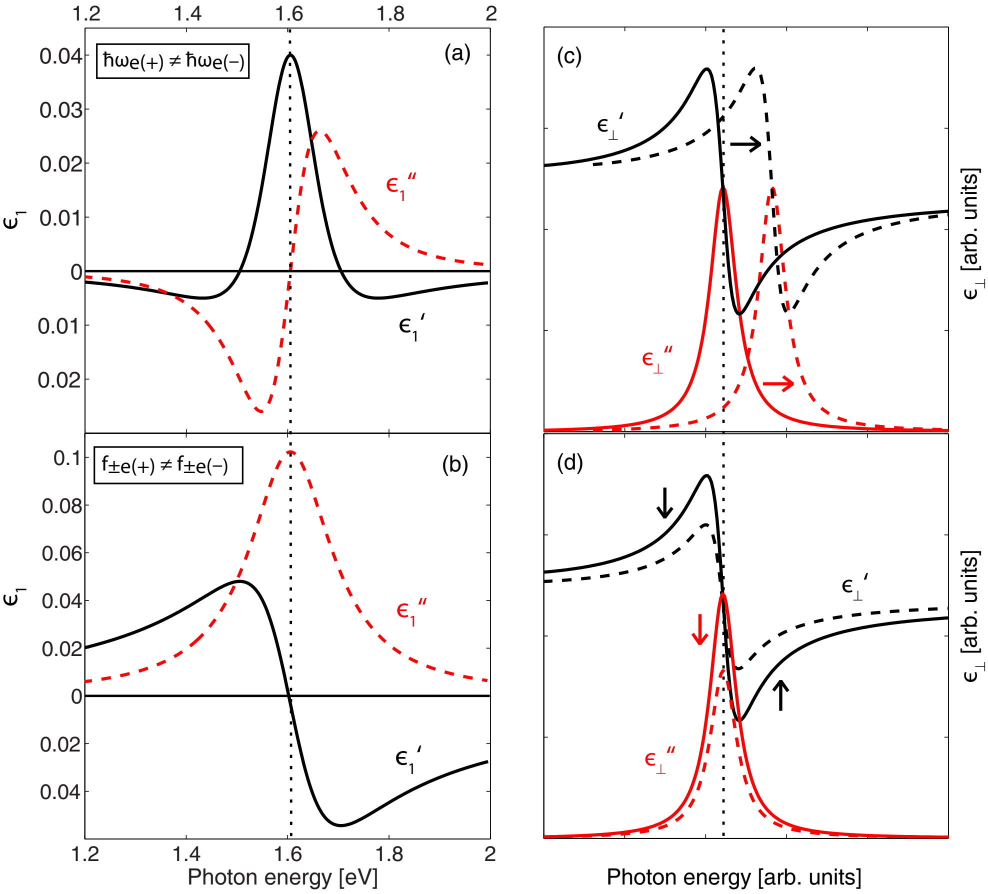

Figure 4.6: Plots of (a) equation 4.12 for the splitting of the degeneracy and (b) equation 4.13 describing the contribution of a splitting of the oscillator strengths to the non-diagonal elements of the permittivity tensor induced by spin-orbit coupling. The energy level splitting, spectral width of the resonance and the splitting in the oscillator strengths have been assumed to be $\Delta E = 1\,\text{meV}$, $\Gamma_e = 0.1\,\text{eV}$ and $\Delta\xi_e = 0.01$, respectively. The dotted vertical line represents the energy of the charge-transfer interband transition in YMnO$_3$ around 1.6 eV. Figures 4.6c and 4.6d illustrate the two contributions to ϵ_1 as the difference in the equilibrium permittivity $\epsilon_\perp$, whose real and imaginary parts are related by the Kramers-Kronig relation around the respective resonances of the sub-levels.

There are, however, two cases, which need to be differentiated. In the first case,[5] the spin-orbit interaction may split the degeneracy in the excited states by the energy

$$\Delta E = 2\hbar\Delta\omega_e 2\hbar(\omega_{e(+)} - \omega_{e(-)}) \tag{4.11}$$

but does not modify the oscillator strengths $f_{\pm e(\pm)}$, which are still identical. Evaluating the sum in equation 4.9 for different resonance frequencies $\omega_{e(\nu)}$ leads to [Kahn et al.,

---

[4] ... although there exist spin-independent contributions as well, which are, however, several orders of magnitude smaller.

[5] to first order in $\boldsymbol{M}$

1969]

$$\epsilon_1 = -\Gamma_e \Delta\omega_e \epsilon''_{\perp,\max} \frac{(\omega_{pp} - \omega_e)^2 - (\Gamma_e^2 + \Delta\omega_e^2) + 2i\Gamma_e(\omega_{pp} - \omega_e)}{[(\omega_{pp} - \omega_e)^2 - (\Gamma_e^2 + \Delta\omega_e^2)]^2 + 4\Gamma_e^2(\omega_{pp} - \omega_e)^2}, \tag{4.12}$$

where $\epsilon''_{\perp,\max}$ is the maximum of the imaginary part of the diagonal permittivity and $\omega_e = 1/2(\omega_{e(+)} - \omega_{e(-)})$. This expression is plotted for the parameters corresponding to our material in figure 4.6a resulting in reasonable magnitudes of the non-diagonal permittivity. The dispersive and dissipative lineshapes obtained for ϵ''_1 and ϵ'_1, respectively, can be understood qualitatively from the difference of the real and imaginary parts of $\epsilon_\perp(\omega_{e,(+)}) - \epsilon_\perp(\omega_{e,(-)})$ due to the frequency shift of the resonances of the previously degenerate excited states $|\pm\rangle$ as illustrated in figure 4.6c, where $\epsilon'_\perp(\omega)$ and $\epsilon''_\perp(\omega)$ have the typical shapes connected by the Kramers-Kronig relations (see, e.g., Kalashnikova and Pisarev [2003]).

In the second case, the degeneracy of the excited states remains unchanged but instead the spin-orbit interaction splits the oscillator strengths of $|\pm\rangle$. An according evaluation of the sum in equation 4.9 for $f_{-e} \neq f_{+e}$ gives the expression

$$\epsilon_1 = -2\xi_e \Gamma_e \epsilon''_{\perp,\max} \frac{\omega_{pp}(\omega_{pp}^2 - \omega_e^2 + \Gamma_e^2) - i\Gamma_e(\omega_{pp}^2 + \omega_e^2 - \Gamma_e^2)}{(\omega_{pp}^2 - \omega_e^2 - \Gamma_e^2)^2 + 4\Gamma_e^2\omega_{pp}^2}, \tag{4.13}$$

where $\xi_e = (f_{-e} - f_{+e})/(f_{-e} + f_{+e})$ is the normalized difference between the oscillator strengths. This situation corresponds to circular dichroism with different absorptions and hence $\epsilon''_\perp$ for the two excited sub-levels of identical energy. The corresponding lineshapes of the real and imaginary part of ϵ_1 are shown in figure 4.6b. Instead of a shift of the resonance as in the previous case, the difference of the diagonal permittivities $\epsilon_\perp(\omega, f_{-e}) - \epsilon_\perp(\omega, f_{+e})$ originates from a difference in the populations of the sub-levels as illustrated in figure 4.6d. The dissipative and dispersive parts are reversed for the two cases, which enables us to attribute the contributions of equation 4.6 to the different physical mechanisms via their lineshape in the spectrally resolved complex rotation signals. However, the complex rotation is not to be confused with the curves shown in figures 4.6a and 4.6b, since the former is defined by equation 1.31. From the latter expression, one can see, e.g., that the real and imaginary part of ϵ_1 enters the imaginary and real part of Θ, respectively, and vice versa, which has to be kept in mind when interpreting the results.

The experimental curves of figure 4.5 have been evaluated by means of equation 4.6 and the results on the spectral dependence of the amplitudes $A_\parallel$ and $B_\parallel$ (A_σ and B_σ) to the linear (circular) anisotropy are shown in figures 4.7b (4.7a) for the corresponding energy range. The real and imaginary parts of the anisotropy signals are not identical with ϵ_1 but also include terms influenced by $\epsilon'_\perp$ and $\epsilon''_\perp$. Consequently, the complex rotations do not directly obey the Kramers-Kronig relations in the general form but are related to each other in a similar way, i.e., the typical Kramers-Kronig behavior of figures 4.7a and 4.7b is distorted by the influence of $\epsilon_\perp$. Anyways, based on the discussion above and keeping in mind how ϵ_1 enters into equation 1.31, the Gaussian contributions A'_σ and A''_σ can be attributed to the splitting of the resonance energies due to their characteristic shapes. Although the exponential B''_σ contribution could not be resolved during the fitting, B'_σ clearly reveals a dissipative lineshape close to the 1.6 eV transition, which marks this contribution to originate from circular dichroism, i.e., a splitting of the oscillator strengths.

The linear contributions $A'_\parallel$ and $A''_\parallel$ also show lineshapes similar to the expected Kramers-Kronig behavior, while $B''_\parallel$ has its maximum far off the resonance and tends to

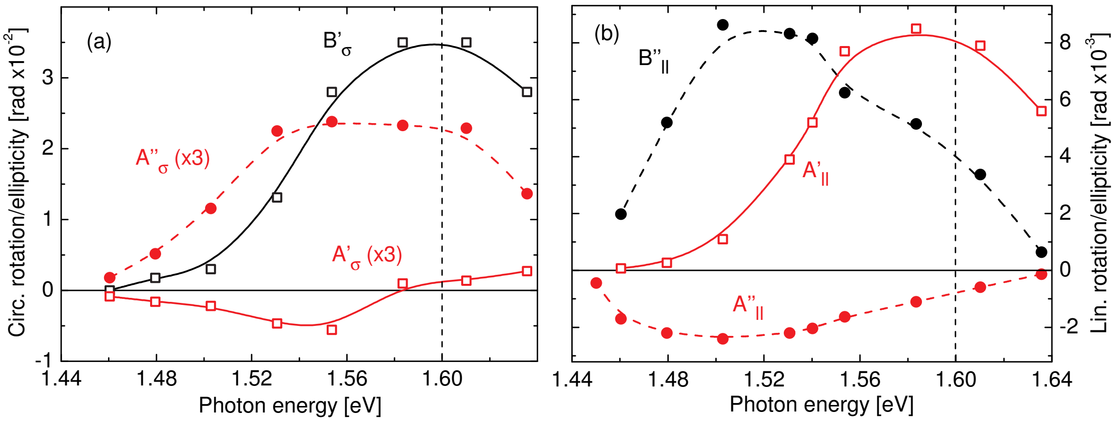

Figure 4.7: Fit results of the data in figure 4.5 evaluated with equation 4.6 for the case of (a) circularly and (b) linearly polarized pump excitation. Both, rotation (squares) and ellipticity (circles) amplitudes, show either a dissipative or a dispersive, i.e., Kramers-Kronig-like, behavior close to the 1.6 eV transition (dashed vertical line). The lines are guides for the eye.

zero when approaching the latter, which suggests a dispersive lineshape. Although the quantitative form of ϵ_2 is not explicitly shown, the physical mechanisms can be described in analogy to ϵ_1 with just a different basis of the eigenstates. Moreover, we can say from a qualitative comparison with ϵ_1, that the lineshapes either originate from a splitting of the resonance energies or the oscillator strengths of the $|xy\rangle$ sub-levels. Hence, the Gaussian coefficients as well as the exponential coefficient show lineshapes that suggest to originate from an energy splitting of the $|x,y\rangle$ states,[6] even though the interpretation of $B''_{\|}$ is not unambiguous.

Both contributions to the coherent electron response occur on timescales smaller than the pump-probe cross-correlation width. The instantaneous Gaussian contribution is interpreted as an optical Stark effect, splitting the degenerate exciton states as described and existing only as long as pump and probe beams overlap, thereby closely following the Gaussian cross-correlation function. The splitting of the exciton states has been described by Joffre et al. [1989] as a sub-level dependent shift of the resonance energies due to a proportionality of the Stark effect to the square of the optical matrix elements. The shift itself is known to result from a renormalization of the eigenstates due to the interaction of the light field with the system resulting in so-called “dressed” states, which can be considered as the stationary states of the coupled system [Boyd, 2008]. The exponential contribution, on the other hand, is determined by the Raman coherence time τ_R and is interpreted as the relaxation of an optically induced difference in the oscillator strengths of the excited sub-levels, i.e., circular or linear dichroism, due to the strong correlations inside the Mott insulator.

4.1.4 Dependence on the Pump Fluence

In general, equation 4.2 shows that the changes in the polarization of a probe beam, which is reflected from the sample surface, are determined by the third-order polarization $P^{(3)}(z,t)$ created by the combined influence of pump and probe beams inside the sample. This polarization is a linear function of the probe electric field and a quadratic function

---

[6] The real and imaginary parts of ϵ_2 enter oppositely into equation 1.31 with respect to ϵ_1.

of the pump electric field:

$$P^{(3)}(z,t) \propto E_{pp}E_{pp}^{*}E_{pr}. \tag{4.14}$$

Hence, the amplitudes of the polarization changes are expected to depend linearly on the pump intensity. Even in the case of a shift of the resonance energies as, e.g., by the optical Stark effect, a linear dependence on the intensity is valid as long as the Rabi frequency Ω is significantly smaller than the detuning Δ of the laser frequency ω_{pp} from the resonance frequency ω_e. The Stark shift depends on the electric field of the pump pulse via the detuned Rabi frequency [Boyd, 2008]

$$\Omega' = (|\Omega|^2 + \Delta^2)^{1/2}, \tag{4.15}$$

where $\Omega = 2|\mu|E/\hbar$ with the electric dipole moment μ. Obviously, the Stark shift goes linearly with the electric field in case of exact resonance ($\Delta = 0$). However, for $\Omega \ll \Delta$, the detuned Rabi frequency can be written as $\Omega' = \Delta\sqrt{1+x^2}$, where $x^2 = |\Omega|^2/\Delta^2$. In this case, the square root may be expanded by a Taylor series around $x = 0$ so that

$$\Omega' \approx \Delta + \frac{1}{2}\frac{|\Omega|^2}{\Delta}. \tag{4.16}$$

Consequently, the Stark shift and the corresponding changes of the polarization will depend quadratically on the electric field, i.e., linearly on the pump intensity.

The electric dipole moment is assumed to be on the order of 10 Debye $\approx 3 \cdot 10^{-29}$ Cm. The maximum pump fluence applied in the experiments amounts to 60 μJ/cm^2 = 0.6 J/m^2. With the relation $I = c\epsilon_0 E^2$ and taking the vacuum permittivity to be $\epsilon_0 \approx 8.85 \cdot 10^{-12}$ C^2/N, we arrive at an electric field strength of $E \approx 226$ N/C. Hence, the Rabi frequency amounts to

$$\Omega \approx 3.3 \cdot 10^8\,1/\mathrm{s} = 0.33\,\mathrm{GHz}. \tag{4.17}$$

The detuning, on the other hand, can be calculated to yield

$$\Delta \approx \frac{(1.60 - 1.55)\,\mathrm{eV}}{\hbar} = 76\,\mathrm{THz}, \tag{4.18}$$

which is orders of magnitude larger than Ω and the previous application of the Taylor expansion represents a good approximation.

Intensity I is measured as the average optical power P_{average} per unit area by means of optical power meters, thus the following relation holds [Hitz et al., 2012]:

$$I = \frac{P_{\mathrm{average}}}{\mathrm{area}} = \frac{\mathrm{energy/pulse}}{\mathrm{area} \times \mathrm{period}} = \frac{\mathrm{pump\ fluence}}{\mathrm{period}}, \tag{4.19}$$

where the period is the time between two pulses, which is determined by the repetition rate of the laser. Since the latter is constant, the pump intensity can be represented by its pump fluence, which is the pulse energy per unit area. Results of corresponding pump fluence dependent measurements are shown in figures 4.8a and 4.8b. The data represents fit results for the coefficients of equation 4.6 of the respective spectrally integrated signals measured with varying pump fluences in the range between 5 and 300 μJ/cm^2. The solid and dashed lines represent linear fits, which are in good agreement with the data with regard to the experimental errors. Consequently, the linear dependence of the polarization signals on the pump fluence is well reproduced by the experimental results

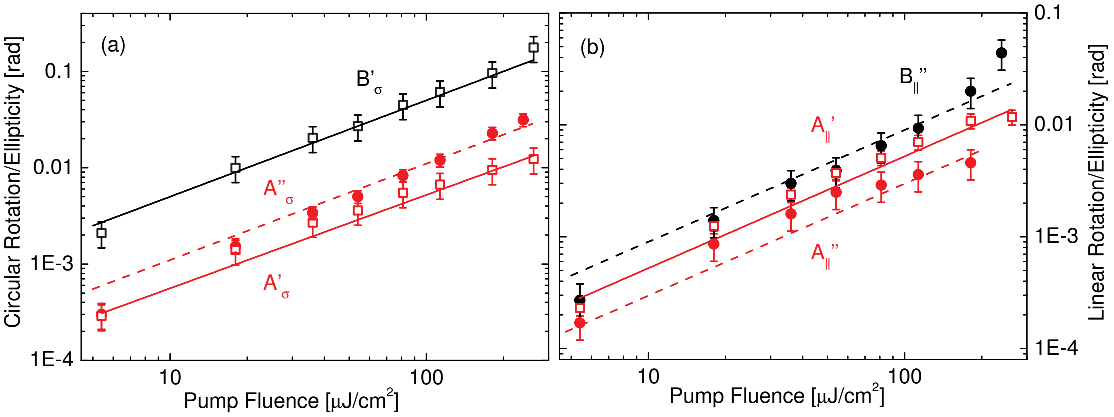

Figure 4.8: Fit results of the time integrated signals obtained by varying the pump fluence between 5 and 300 μJ/cm^2. The results are shown on a double logarithmic scale. The real and imaginary parts of the coefficients of equation 4.6 represent the transient rotation (empty squares) and ellipticity (full circles), respectively. The solid and dashed lines represent linear fits to the data points.

4.2 Conclusions

Ultrafast optically induced electronic processes in $YMnO_3$ have been studied on a subpicosecond timescale by direct pump-probe experiments at room temperature as well as at cryogenic temperatures around photon energies of 1.55 eV. Based on experimental data in the literature and on symmetry considerations, a model for the electronic transitions has been proposed. This model claims the $\Gamma_1 \rightarrow \Gamma_5$ charge-transfer transition from the hybridized O^{2-}(2p)-Mn^{3+}(3d) ground state to the doubly degenerate $Mn^{3+}(3d_{3z^2-r^2})$ states responsible for the observed phenomena. By means of differential reflection and polarization sensitive measurements, two kinds of relaxation processes could be distinguished. The charge-carriers were shown to relax within a characteristic time of 500 fs, while the relaxation of the coherent electronic processes, i.e., the optically induced linear and circular anisotropies, is determined by the Raman coherence time $\tau_R = 10 \pm 4$ fs. The latter were attributed to the optical alignment of the angular momentum distribution in the xy-plane and along the z-direction, respectively.

By spectrally resolving the signals, we could distinguish between two contributions of the respective anisotropies, which each show a different and characteristic spectral dependence around the charge-transfer resonance energy. Herewith, the Raman coherence time could be linked to the circular dichroism, while the instantaneous contribution has been identified as the optical Stark effect. These results were both supported by their expected and verified linear dependence on the pump fluence of the laser. The exceptional speed of the equilibration of the coherent electronic processes, i.e., the angular momentum anisotropies, has been attributed to the strong Coulomb forces present in the Mott insulator $YMnO_3$, which lead to efficient scattering and dephasing channels.

The presented phenomena prove $YMnO_3$ to be an interesting material for femtosecond laser manipulation of electron states in all-optical device technologies [Wada, 2004]. Moreover, $YMnO_3$ is known to be multiferroic. Magneto-electric coupling is forbidden in hexagonal $YMnO_3$ due to its crystallographic structure and magnetic symmetry [Eerenstein et al., 2006]. However, the strong correlation of spin, charge and orbital degrees of freedom holds the potential to influence both, structure and symmetry, by sufficiently strong optical excitation in the femtosecond time domain. Magneto-electric coupling in principle holds the possibility to store information electrically as in ferroelectric random access memory (FeRAM) [Scott and Araujo, 1989], while reading magnetically as is common standard in magnetic hard disk drives. In future data storage devices, this could circumvent the problematic electric read-out of FeRAMs and the high local magnetic fields necessary to write data magnetically.

Chapter 5

Optically Induced Dynamics in Magnetic Iron Garnets

In this chapter, we concentrate on the optical magnetization control in magnetic iron garnets. Magnetic iron garnets are known since roughly the middle of the 20th century. Until then, they have developed into an important material class for magneto-optics and can be synthesized with high perfection as mono- or polycrystalline bulk or epitaxial film samples. They exhibit a large magneto-optical response due to a strong spin-orbit interaction while the damping of magnetic excitations can be very low (see Hansteen et al. [2006] and references herein). Their extraordinary low optical absorption in the near-infrared and microwave frequency range is advantageous for the propagation of electromagnetic waves and respective magneto-optical applications. Most importantly, a multitude of rare-earths, transition metals and other ions can be incorporated into the crystal lattice among the different sublattices (see section 5.1.1). This results in either paramagnetic, antiferromagnetic or ferrimagnetic compounds, which allow to study certain aspects of magnetism and its interaction with light in a controlled way (see Hansen et al. [1978] and references herein).

The samples are either excited by circularly or linearly polarized light, which will be shown to trigger different mechanisms for the magnetization precession. The most important of these is the inverse Faraday effect (IFE) (see section 1.3.1). Sections 5.1.2 and 5.1.3 deal with the fundamental understanding of the underlying physics of the optically induced phenomena in bare films as well as magneto-plasmonic crystals based on magnetic garnets. Section 5.1.4 then tries to establish the connection of ultrafast magnetization control to the transverse magneto-optical Kerr effect (TMOKE), which has been the subject of section 3.1 and which has proven to be a very versatile tool for magneto-optical device technologies.

5.1 Ultrafast Optically Induced Precession of the Magnetization

5.1.1 Rare-Earth Substituted Bismuth Iron Garnets

Nearly all of the iron garnets tend to form crystals of cubic symmetry. The chemical formula of garnet compounds is complex and the lattice constants of the unit cells frequently exceed 10 Å. The general formula of garnets is $\{C_3^{3+}\}[A_2^{3+}](D_3^{3+})O_{12}^{2-}$, where C, A and D are the ions with eightfold, sixfold and fourfold oxygen coordination on the dodecahedrally c-sites, the octahedrally a-sites and the tetrahedrally d-sites of the crystal lattice, respectively. The occupation of the different sublattices is dependent on the sizes of the respective ions with the larger ions like bismuth and yttrium preferring the c-sites, while the small ions like iron, gallium and germanium prefer the d-sites. The valency of the ions is predominantly 3+. Deviations from this value are only allowed under certain conditions (see Hansen et al. [1978]; Huber [1970] and references herein).

The magnetic ordering is determined by the interaction of the magnetic sublattices. For example, in yttrium iron garnet ($Y_3Fe_5O_{12}$, also referred to as YIG), the non-magnetic yttrium ions occupy the c-sublattice, while the iron a- and d- sublattices are dominated by a strong antiferromagnetic coupling. Consequently, there is one ion per unit formula on the d-sites, whose spin is not compensated and determines the small net magnetization of YIG. The incorporation of magnetic ions like bismuth on the other hand can strongly increase the magnetic response of the iron garnet compounds. The overall magnetization is then the sum of the magnetic moment of the iron sublattice and that of bismuth.

The chemical formula of the iron garnet film, which has been used in the following experiments, is $(BiSmTm)_3(FeGa)_5O_{12}$ (see sample 2 in table 3.1), i.e., the c-sites are occupied by the rare earth ions Sm^{3+} and Tm^{3+} as well as the heavy metal ion Bi^{3+}, while the iron a- and d-sublattices are substituted with Ga^{3+} ions to equal amount. The overall magnetization of the sample depends on the interaction of the c-sublattice with the iron sublattices. Although there is an expected antiferromagnetic alignment between the latter for the substitution with thulium, this is not the case for bismuth and samarium so that there is a net uniaxial magnetic anisotropy, which is oriented perpendicular to the film surface, i.e., in the z-direction (see section 3.1.2).

5.1.2 Direct Perturbation of the Magnetization

The sample has been excited by pulses of $\sim 20\,\mathrm{fs}$ duration at photon energies around 1.55 eV by means of the ultrafast pump-probe setup described in section 2.1. In figure 5.1, the rotation of the linearly polarized probe pulse has been detected as a function of the pump-probe delay under left- and right-circularly polarized pump excitation with an external applied field of $B = 205\,\mathrm{mT}$ in Voigt geometry (along $\boldsymbol{x}$). The signals show oscillations around 5 GHz with a 180° phase shift with respect to each other.

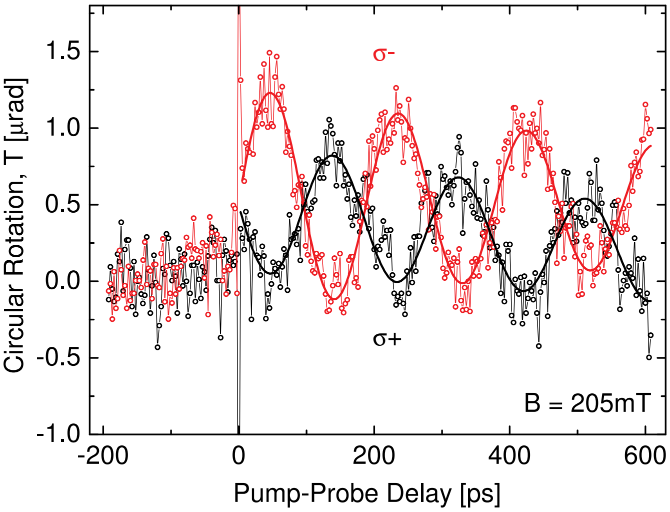

Figure 5.1: Time-resolved optically induced rotation of the linear polarization of the transmitted probe beam, which oscillates with a frequency around 5.4 GHz. The sample has been excited with left- ($\sigma-$) and right-circularly ($\sigma+$) polarized light, respectively, and the signals have been fitted with equation 5.1 (solid curves), revealing a relaxation time of the amplitude A of $\tau = 730\,\mathrm{ps}$. The oscillation represents a precession of the magnetization inside a magnetic garnet film around an equilibrium direction, which depends on the strength of an externally applied magnetic field in Voigt geometry.

The amplitudes of the two oscillations are different for the two senses of polarization. They are both in the microradians regime and disappear for zero external field as will be shown later. In the experimental geometry, the rotation of the probe polarization originates from the Faraday effect, which requires a magnetization in $\pm\boldsymbol{k}$, where $\boldsymbol{k}$ is the wavevector of the light propagating in the z-direction. Within this picture, the observed signals represent an oscillation of the z-component of the magnetization. The distinct polarization dependence of the signals suggests a non-thermal effect since a heating of the sample by laser pulses should be independent on a left- or right circular polarization of the light. On the contrary, a thermal effect requires absorption, which can be neglected at the applied photon energies. Hence, we can assume that the magnetization in these measurements is manipulated by a non-thermal mechanism.

Since the sample is excited by circularly polarized light, it is reasonable to assume that the oscillation corresponds to a photo-induced precession around some equilibrium direction and that the non-thermal mechanism is the IFE. The equilibrium direction must not necessarily lie in the film plane as discussed above but depends on the external field and is parallel to $\boldsymbol{H}_{\text{ext}}$ under saturation, i.e., in the film plane. If the equilibrium direction is not exactly perpendicular to $\boldsymbol{k}$ but instead tilted in $\pm\boldsymbol{k}$ direction, the inflection point of the oscillation will deviate from zero and instead have a positive or negative offset as is the case in figure 5.1. This observation is in accordance with the moderate external field, which does not saturate the film but rather aligns the magnetization in the xz-plane at some angle with the sample surface.

The signals can be well fitted with the function

$$y = A\exp(-t/\tau)\sin(\omega t) + B, \tag{5.1}$$

where t is the pump-probe delay, τ is the relaxation time of the oscillation amplitude A and B is the offset of the inflection point. From the sinusoidal shape of the signals follows that shortly after the optical excitation, $\boldsymbol{M}$ and $\boldsymbol{H}_{\text{eff}}$ (see equation 1.52) must be parallel according to equation 1.54. Subsequently and depending on the physical mechanism of the perturbation, either the magnetization or $\boldsymbol{H}_{\text{eff}}$ responds to the perturbation and changes direction. The angle between the two quantities leads to a torque [Blundell, 2001]

$$\boldsymbol{G} = \boldsymbol{r} \times \boldsymbol{F} = \boldsymbol{M} \times \boldsymbol{B} \tag{5.2}$$

acting on the magnetization via the Lorentz force $\boldsymbol{F}$, where $\boldsymbol{r}$ is a coordinate vector pointing to the electron. Hence, the Lorentz force is the source of the precession described by equation 1.54.

We know already, that circularly polarized light induces a magnetization directed along $\pm\boldsymbol{k}$ due to the IFE in transparent media. Hence, we assume that $\boldsymbol{H}_{\text{eff}}$ in equation 1.51 is unaffected by the optical excitation and instead the magnetization $\boldsymbol{M}$ is shifted accordingly. In this case, for the different helicities, the torque $\boldsymbol{G}$ points in opposite directions according to equation 5.2, which accounts for the phase difference of the two signals in figure 5.1.

In order to gain further insight into the underlying physics, the dependence of the signals on the external field up to 375 mT has been measured (see figure 5.2). Again, the signals have been fitted with equation 5.1 from which the oscillation frequency has been extracted. The latter increases linearly with the magnetic field (figure 5.3). The slope of this linear dependence can be used to calculate the g-factor by formally solving the Landau-Lifshitz-Gilbert equation 1.54 for the z-component of the magnetization. One

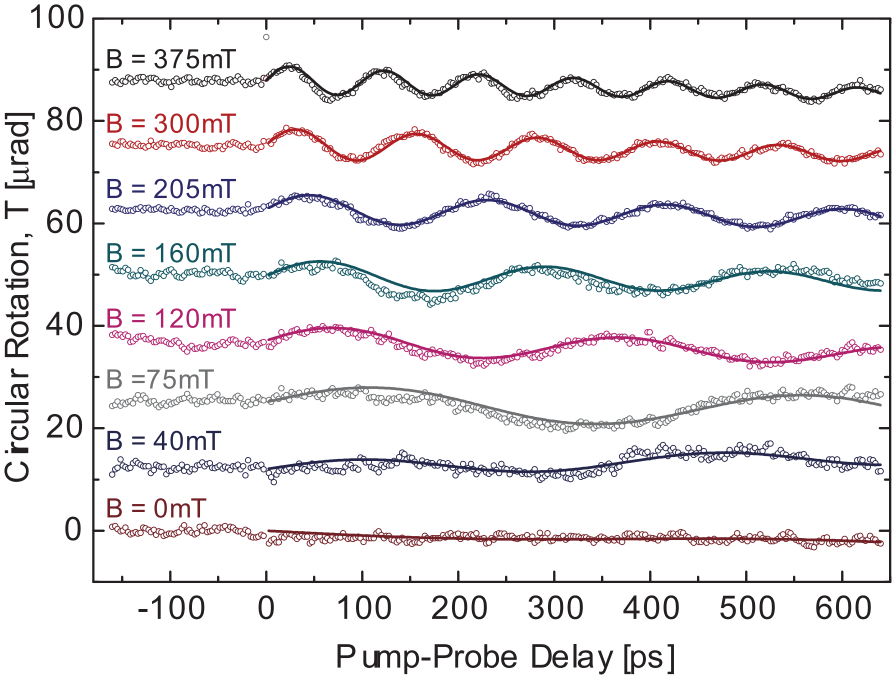

Figure 5.2: Dependence of the signals of figure 5.1 on the strength of the external magnetic field showing the change of the precession amplitude. The data has been fitted with equation 5.1 (solid curves). The obtained fit parameters are presented in figure 5.3. Due to the limited range of pump-probe delays, the extraction of the frequency and amplitude for the curves showing only one or few oscillation periods is governed by a larger experimental error.

can immediately find the solution ($\boldsymbol{B} = (B, 0, 0)$)

$$M_z = -M_y \exp(\gamma B t), \tag{5.3}$$

where $\omega = \gamma B$ is the precession frequency. Hence, we can write

$$W = \hbar\omega = g\mu_B B, \tag{5.4}$$

which reveals the slope of the magnetic field dependence to be identical to $g\mu_B$. Since $\mu_B = 5.788 \cdot 10^{-5}\,\mathrm{eV/T}$ and the slope has been determined to be $1.137 \cdot 10^{-4}\,\mathrm{eV/T}$ from a linear fit to the data shown in figure 5.3, we get a g-factor of

$$g = 1.964 \approx 2, \tag{5.5}$$

which is very close to the value expected for the electron spin. Consequently, we can conclude that the observed precession is predominantly a spin precession.

Moreover, figure 5.3 gives the amplitude extracted from the signals of figure 5.2 in dependence of the magnetic field. Error bars reflect the fact that the amplitudes of the low field oscillations have a higher uncertainty due to the low number of observed oscillation periods (resulting from a finite value of the maximum pump-probe delay). Within these experimental errors, the amplitude of the oscillation remains constant with the external field, which supports the previous assumption that the circularly polarized excitation induces a shift of the magnetization instead of the effective field $\boldsymbol{H}_{\mathrm{eff}}$. In this case, the signal amplitude is exclusively determined by the strength of the optically induced magnetization via the IFE, which is responsible for the displacement.

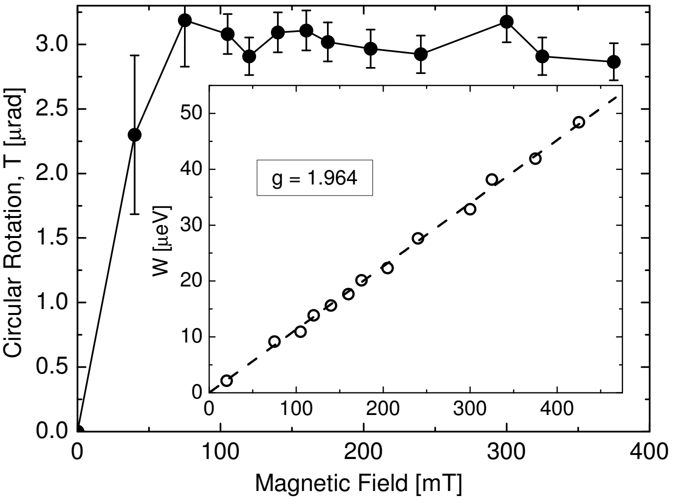

Figure 5.3: Visualization of the fit parameters A (full circles) and W (inset, see equation 5.4) extracted from the signals of figure 5.2 with equation 5.1. Within the experimental error, A is independent on the field strength over the observed measurement range. From the slope of a linear fit (dashed line) of the precession energy W, a g-factor of 1.964 can be calculated (see text for details), which suggests a pure spin precession.

However, upon close inspection of figure 5.1, one can see that the amplitudes for the $\sigma-$ and $\sigma+$ signals are not identical. Hansteen et al. [2006] argued that, although the shift of the magnetization is the dominant mechanism under circularly polarized excitation, $\boldsymbol{H}_{\text{eff}}$ is also shifted due to a change in the anisotropy field $\boldsymbol{H}_{\text{a}}$, which is independent on the light helicity. The shift occurs either towards or away from the magnetization displacement for $\sigma+$ or $\sigma-$ excitation, respectively. Consequently, the latter signal ($\sigma-$) has the larger precession amplitude. The change of the anisotropy field is attributed to an optically induced electron transfer between ions on nonequivalent sublattices in the garnet, which leads to a redistribution of the ions and hence a change in the magneto-crystalline anisotropy.

5.1.3 Indirect Perturbation of the Magnetization

As derived in section 1.3.1, the IFE and consequently the source of the optically induced precession discussed in the previous section is expected to vanish for excitation with linearly polarized light. Surprisingly, when repeating the measurements of section 5.1.2 with the corresponding linear polarization, the signals also show oscillatory behavior, whose amplitude is again in the micro radian regime. The so obtained "linear rotation" signals have been measured for different angles α of the pump polarization plane about the z-axis. Pump- and probe polarizations were perpendicular with respect to each other at all times in order to minimize pump scattered light in the detection path. As before, the external magnetic field is directed along $\boldsymbol{x}$ so the orientation of the crystal axes with respect to $\boldsymbol{H}_{\text{ext}}$ is unchanged (see inset of figure 5.5). Apart from that, the experiment is equivalent to a rotation of the sample by the rotation angle α.

The results are given in figure 5.4 with the according sinusoidal fit curves. Although the oscillation amplitude is expected to decrease with increasing pump-probe delay, there is instead a monotonous rise of the former, which could be due to a misalignment of the delay line. As a consequence, the overlap of the pump and probe beams on the sample depends on the delay. Another explanation could be an initially (fixed) imperfect overlap of the pump and probe beams, while the alignment of the delay line is in impeccable. In this case, the optically induced spin-wave at the position of the pump spot propagates

---

[1] Signal modulation has been established with a PEM. However, an additional Glan-Thompson prism and a $\lambda/2$-plate have been placed in the pump beam, i.e., not the difference between H- and V-polarizations is measured but only the difference between pump on and off, which implies a factor 2 difference in the amplitude.

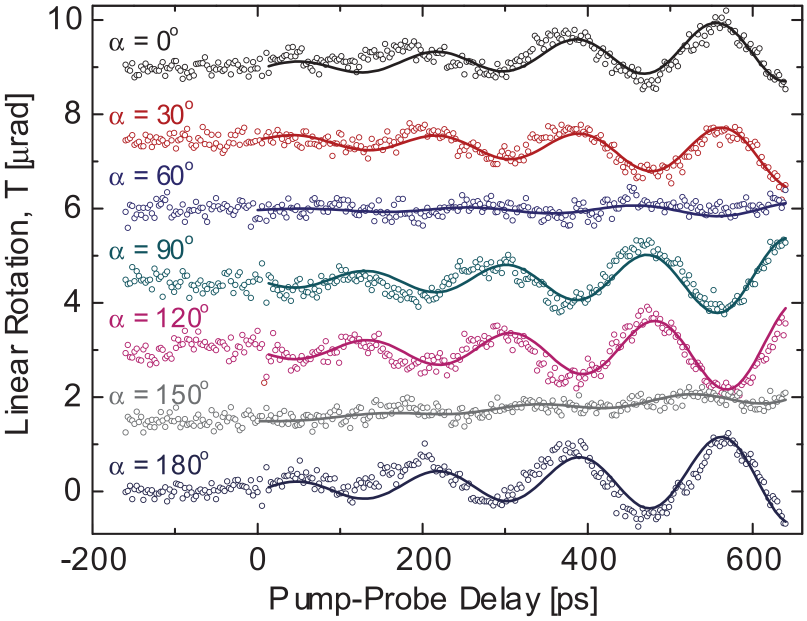

Figure 5.4: Time resolved pump-probe signals for the optically induced magnetization precession with linearly polarized light. The different curves represent different rotation angles of the sample about z. The curves have been fitted with equation 5.1 (solid curves). However, τ has no physically reasonable meaning here (see text for explanation).[1]

across the sample and reaches the probe spot only after a certain delay. More important than the relaxation time, however, is the dependence of the signal phase on the rotation angle with a periodically vanishing and reappearing oscillation amplitude.

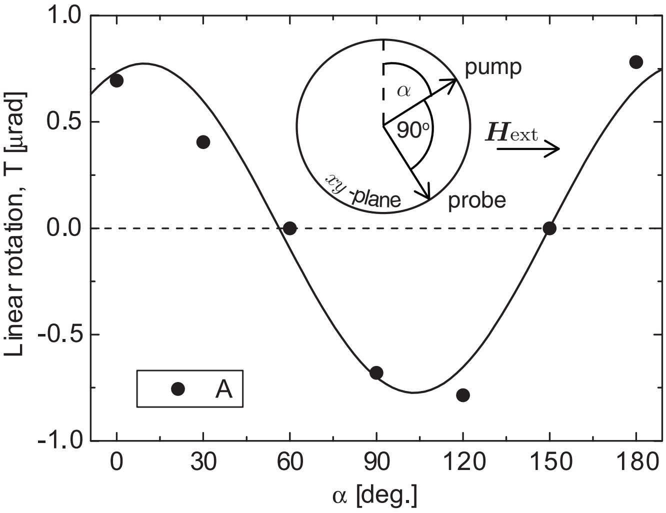

Figure 5.5: The amplitude A (full circles) extracted from the curves of figure 5.4 is a π-periodic function (solid curve) of the rotation angle α. The signals at 90° difference have opposite phase but identical amplitude. The polarization dependence is triggered by a transient optically induced change of the anisotropy field (see text).

The angle dependence of the amplitude A is shown in figure 5.5. A sine fit reveals a π-periodical behavior, i.e., the precession amplitude reaches two extrema (with opposite phase) at two angles, which are perpendicular to each other, and vanishes for two angles in between. As in the case of circular precession, the polarization dependence eliminates the possibility of a thermal mechanism. However, since this effect was not of prime importance to us, the reader is referred to the literature for more details on the underlying mechanism of these phenomena. For example, Hansteen et al. [2005] argued that the optical excitation induces transient changes to the anisotropy field $\boldsymbol{H}_\mathrm{a}$ in the film plane.

Upon rotation of the sample by an angle α, the anisotropy field rotates by 2α, which leads to vanishing precession whenever the condition $\boldsymbol{H}_\mathrm{a} \parallel \boldsymbol{H}_\mathrm{eff}(0)$ is fulfilled.

5.1.4 All-Optical TMOKE

In section 3.1, we discussed the transverse magneto-optical Kerr effect as a versatile tool for the control of optical properties in magneto-plasmonic crystals. Although this effect holds potentially useful properties, such as the possibility of plasmonic enhancement (section 3.1.2) and a large spectral tunability (section 3.1.5), the presented method had the drawback of slow modulation speed of the sample magnetization since this was established by external magnetic fields. Especially with regard to ultrafast device technologies, this disadvantage must be overcome.

In this respect, all-optical manipulation by means of femtosecond pulsed lasers seems most promising. In order to establish the TMOKE geometry as depicted in figure 3.2c, the optically induced circular rotation of the magnetization inside garnet films, which was the subject of the previous sections, can be exploited. Therefore, the magnetic garnet film of sections 5.1.2 and 5.1.3, is used to fabricate an MPC sample, which was referred to as “sample 2” in the previous text and whose properties and general design can be found in table 3.1 and figure 3.1, respectively. This sample is now excited with circularly polarized pump pulses from the magnetic film side thereby exciting a magnetization precession about a predefined effective magnetic field, which is controlled by an external field. A probe beam incident from the gold side onto a sub-wavelength grating excites a surface plasmon polariton traveling in the direction of the grating vector Λ. Whenever the precessing magnetization has a component perpendicular to Λ in the film plane, the TMOKE geometry is established and we expect to see periodic variations in the transmitted or reflected probe intensity with the precession frequency ω as already demonstrated in section 3.1.

Since the observed signals originating from the optically induced magnetization precession are known to be in the micro radians regime, a high pump fluence is required in order to observe the all-optical TMOKE as discussed above. Therefore, the following measurements have been performed with a regenerative amplifier (REGA) laser system for pump fluences of several $\mathrm{mJ/cm^2}$. The corresponding magnetization precession for a pump fluence of $1.7\,\mathrm{mJ/cm^2}$ and an external field of $\sim 100\,\mathrm{mT}$ is shown in figure 5.6a for right- and left-circularly polarized excitation, respectively (compare figure 5.1). In these measurements, both, pump and probe beams, are incident from the GGG side and reflected from flat gold. The flat gold response has already been discussed in the context of equation 3.10. The B contribution to the response, which on a femtosecond time scale appears as a constant plateau, was attributed to the relaxation of the lattice temperature due to phonon-phonon scattering. On the picosecond timescale of figure 5.6a, however, this component can be temporally resolved revealing a characteristic relaxation time of $\sim 10\,\mathrm{ns}$, where the fit is indicated by the dashed line. The amplitude of the gold response is orders of magnitude reduced compared to the signals shown in section 3.2 and ideally should not appear at all in the polarization sensitive measurement of figure 5.6a. It does appear, however, since the higher pump fluence causes an increased heating of the gold electron temperature with respect to section 3.2. Hence, also the lattice temperature is increased, which is proportional to B. This in combination with an omnipresent imperfect balancing of the two diodes of the balanced photo-detector results in the appearance of B as a background artifact in the polarization measurements. The A_1 and A_2 components of the gold response are not resolved in this experiment and only visible as a sharp spike close to zero delay.

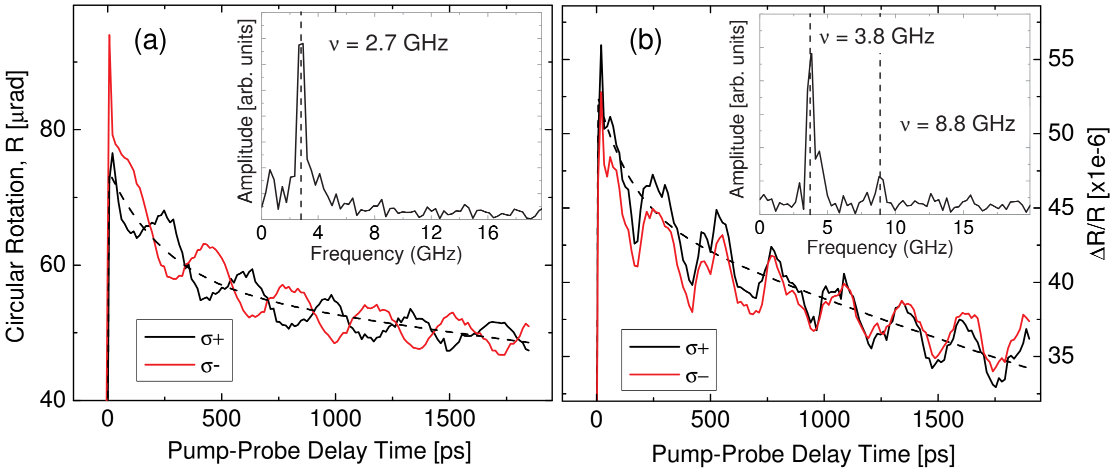

Figure 5.6: Pump-probe signals of the circular rotation and differential reflectivity of sample 2 under excitation with left- (red curves) and right-circularly (black curves) polarized pump light at room temperature. The sample is excited from the GGG side with a pump fluence of 1.7 mJ/cm^2. The external field is $B = 100\,\mathrm{mT}$. The dashed lines are fits to the signals with equation 3.10 visualizing the contribution of the optical response of the gold film (see text). (a) Rotation of the plane of polarization of the linearly polarized probe beam after reflection from flat gold (incident from the garnet side, compare figure 5.1). The inset shows the amplitude of the corresponding fast Fourier transformation (FFT). (b) Differential reflectivity of the probe beam after reflection from the sub-wavelength gold grating (incident from the gold side). The observed oscillations are SPP mediated and insensitive to the excitation polarization. A FFT analysis (inset) reveals frequency components at 3.8 GHz and 8.8 GHz, respectively.

Superposed on the gold response are oscillations with opposite phase for the two excitation polarizations. The inset of figure 5.6a shows the characteristic spectrum of a fast Fourier transformation (FFT). The spectral amplitude has a pronounced peak at the oscillation frequency of $2.7\,\mathrm{GHz} \equiv 11\,\mu\mathrm{eV}$. This corresponds well with the magnetic field dependence of figure 5.3, which identifies the oscillations as an optically induced spin precession.

From these results, the expected TMOKE amplitude can be roughly estimated as follows: The amplitude of the magnetization precession excited with 1.7 mJ/cm^2 is on the order of $6\,\mu\mathrm{rad}/(2\cdot 5\,\mu\mathrm{m}) \approx 34°/\mathrm{m}$ since the measurements were performed in reflection and the magnetic film thickness amounts to $5\,\mu\mathrm{m}$. As discussed before, this amplitude is exclusively determined by the magnitude of the optically induced magnetization by means of the inverse Faraday effect. According to Hansen and Krumme [1984], comparable garnet films show Faraday rotation angles of 50000°/m for a fully aligned (saturation) magnetization M_s. The magnetic field dependence of figure 3.6 tells us that we can align this saturation magnetization M_s in Voigt geometry by applying an external field of roughly 80 mT independent of the exact value of M_s. In order to estimate the TMOKE corresponding to a Faraday rotation of 34°/m instead, we have to look at the respective curve of figure 3.6 for the value

$$B = \frac{34°/\mathrm{m}}{50000°/\mathrm{m}} \cdot 80\,\mathrm{mT} \approx 5\cdot 10^{-4}\,\mathrm{T}. \qquad (5.6)$$

By means of an interpolation of the data points, figure 3.6 can be used to reveal a TMOKE amplitude on the order of $1\cdot 10^{-5}$.

Given a sensitivity of the setup of $1\cdot 10^{-6}$, the optically induced TMOKE should be observable in the differential reflectivity $\Delta R/R$ measured under comparable conditions, which is shown in figure 5.6b. Here, the probe beam is incident from the gold side onto the sub-wavelength grating under an angle of 30° now (in accordance with the experimentally obtained resonance angles of figure 3.11b). The signals indeed show oscillations similar to the ones observed for the magnetization precession. They are, however, independent on the pump polarization and a FFT analysis (inset of figure 5.6b) reveals also a difference in the frequency components. The amplitude of the FFT shows a strong and a minor peak at 3.8 GHz and 8.8 GHz, respectively. A variation of the probe incidence angle (not shown here) suggest that the oscillations are connected to the excitation of the SPP mode of the grating structure and disappear if the incidence angle deviates from the SPP resonance condition.

Also with higher pump fluences, variations of the incidence angle and/or linearly polarized excitation, polarization sensitive features could not be found in the differential reflectivity or transmissivity. Instead, a comparison with the literature leads to the conclusion that the $\Delta R/R$ oscillations are most likely due to displacements of the gold grating elements due to the excitation of surface acoustic waves at the gold/garnet interface. These periodic displacements modulate the geometric parameters of the grating and thereby induce an oscillation of the SPP resonance energy [Brüggemann et al., 2012a], which in turn modulates the optical properties, such as the reflectivity of the structure, in the GHz regime. The exact frequency of these modes depends on the interaction of the surface modes of the gold grating with bulk phonon modes of the garnet film. Similar phenomena have been observed in various nanostructures, e.g., by Antonelli et al. [2002]; Chen et al. [2010]; Guyader et al. [2008] yielding oscillation frequencies comparable to the ones observed in figure 5.6b. Since the physics of surface acoustic modes is not the subject of this work, the reader is referred to the literature for details. It should also be noted that Brillouin scattering from the nanostructure, as discussed, e.g., by Brüggemann et al. [2012b] can be excluded as a physical mechanism since the calculated frequencies of the existing diffraction orders ($m = -1, 0, 1$) deviate from the measured ones by roughly one order of magnitude.

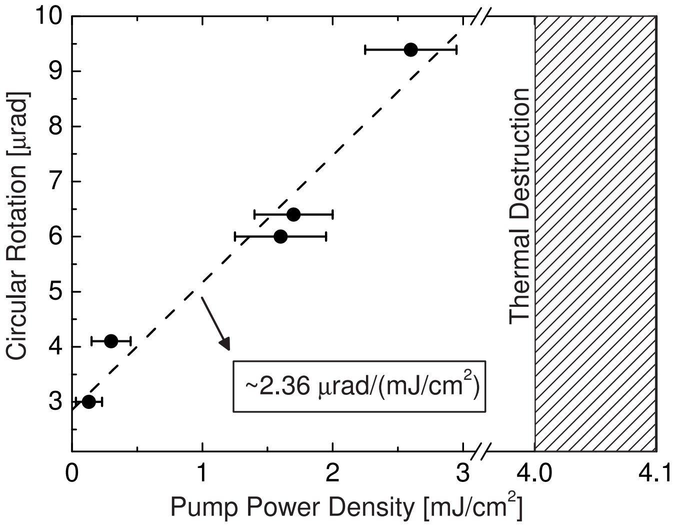

Figure 5.7: Power density dependence of the magnetization precession amplitude of the garnet film upon reflection from the smooth gold film. Error bars represent the uncertainty in the determination of the laser spot diameter on the sample. The dashed line is a linear fit to the data points. The patterned area marks the region of power densities leading to an irreversible thermal destruction of the gold film.

The dependence of the amplitude of the magnetization precession induced in the magneto-plasmonic crystal sample as a function of the pump fluence is given in figure 5.7. During these measurements, the destruction threshold of the sample could be determined to be 4 mJ/cm^2 for non-plasmonic excitation, which originates from an optically induced heating of the gold electron system above the melting point ($\sim$ 1060 K under standard conditions, see Decker and Vanfleet [1965]), i.e., irreversible thermal destruction. The heating of the electron system has already been discussed extensively in section 3.2. It is straightforward to assume that the amount of heat produced close to the gold/garnet interface during the experiments performed in the mJ/cm^2 regime is already considerably high. It is also known that heat counteracts the alignment of magnetic moment as demonstrated, e.g., in photo-induced demagnetization experiments [Beaurepaire et al., 1996]. Taking this into account, the amplitude of the optically induced TMOKE could be significantly lower than the value estimated from equation 5.6.

The results reveal a severe limit for the usefulness of the TMOKE in ultrafast applications. An obvious thought would be to cool down the sample but since we are dealing with an optically induced temperature rise of the electron system on the order of 1000 K, a reduction of the initial electron temperature to cryogenic temperatures, i.e., by $\sim 300\,\mathrm{K}$, brings only little improvement. The main drawback here seems to be the inefficiency of the IFE with respect to the induced strength of the magnetization. Certainly there can be found more suitable materials (possibly garnets with different composition) to be used as the magneto-optically active component of the MPC sample while the plasmon resonance can always be tuned accordingly by means of the gold grating parameters (see section 3.1.5).[2]

5.2 Conclusions

Optically induced magnetization dynamics have been examined in magneto-plasmonic crystals and bare films of rare-earth substituted iron garnets by means of pump-probe spectroscopy. The experiments have been performed with femtosecond laser pulses as well as amplified (picosecond) pulses by means of a regenerative amplifier exhibiting pump fluences per unit area in the micro- and millijoule regime, respectively. Since the applied photon energies were in the near-infrared spectral range, absorption in the garnet films could be neglected and all light induced excitations could be treated in the transparent regime.

Our experimental results demonstrate that circularly as well as linearly polarized light excitation of magnetic garnets leads to a precession of the magnetization $\boldsymbol{M}$ about an effective magnetic field $\boldsymbol{H}_{\mathrm{eff}}$, which is determined by the external, demagnetization and anisotropy fields. The photo-induced dynamics are governed by the Landau-Lifshitz-Gilbert equation. Both phenomena are induced by non-thermal perturbation mechanisms, which are, however, slightly different for the two types of excitation polarization. The linearly induced effects most likely originate from a pump induced change of the anisotropy field due to a realignment of the ions on non-equivalent lattice sites of the garnet compound. This causes a transient displacement of $\boldsymbol{H}_{\mathrm{eff}}$, which starts the precession of $\boldsymbol{M}$. The main focus, however, was directed towards the circularly induced phenomena. Here, the circularly polarized light induces a magnetization parallel or antiparallel to its k-vector, which is known as the inverse Faraday effect (IFE). The IFE directly causes a transient displacement of the overall magnetization, which leads to the precession of the latter about $\boldsymbol{H}_{\mathrm{eff}}$ with frequencies in the gigahertz regime.

Since the amplitude of the precession does not depend on the external magnetic field, a displacement of $\boldsymbol{H}_{\mathrm{eff}}$ instead of $\boldsymbol{M}$ could be excluded as the main physical mechanism

---

[2] It should be noted that Hansteen et al. [2006] claimed to achieve photo-induced magnetizations corresponding to $\mu_0 M = 0.6\,\mathrm{T}$ with laser pulses of $20\,\mu\mathrm{J}$ energy in a different garnet sample. However, the applied pulse energy is a factor of 50 higher than the maximum applicable pulse energy for our MPC sample.

of the circular rotation signals. The frequency of the precession depends linearly on the strength of the external magnetic field, from which the electron g-factor could be extracted. That way, the observed effect could be unambiguously identified as a pure spin precession.

The main purpose of the research discussed in this chapter was the demonstration of the all-optically induced transverse magneto-optical Kerr effect, which has proven to be a versatile tool for magneto-optical applications. Optical control of the TMOKE would qualify the effect for ultrafast device technologies. Therefore, the magnetic garnet film was incorporated into an MPC crystal combining plasmonic enhancement of the TMOKE (as shown in chapter 3) and gigahertz precession of the magnetization. Unfortunately an experimental evidence could not be found, although the influence of $\boldsymbol{M}$ on the properties of the surface plasmon polariton of the MPC sample was estimated to be large enough to be seen in the experiments.

Finally, the dependence of the precession amplitude on the pump fluence was analyzed in reflection from the MPC. The results revealed a destruction threshold of the sample around $4\,\mathrm{mJ/cm^2}$. At these power densities, the heating of the electron system of the gold film increases the film temperature above the melting point, which leads to irreversible destruction. Therefore, it is reasonable to assume that the heat produced in the MPC sample diminishes the magnetization and decreases or completely erases the amplitude of the all-optical TMOKE. Since the melting point of gold amounts to over $1000\,\mathrm{K}$, a cooling of the sample does not solve the problem. Instead, the efficiency of the IFE in the garnet film and the corresponding precession amplitude have to be increased, which in the current sample does not exceed the microradians regime. This could be established by different compositions of the garnet film. More promising, however, would be to adjust the excitation photon energy more closely to the first excited state of the garnet in order to enhance the spin-flip probability of the ground state electrons, which is the source of the IFE. Once these parameters are optimized, the power densities and hence the electron temperature rise can be reduced, which holds a reasonable chance for the realization of the all-optical TMOKE for future ultrafast magneto-optical device technologies.

Bibliography

Aers, G. C. and Boardman, A. D. The theory of semiconductor magnetoplasmon-polariton surface modes: Voigt geometry. Journal of Physics C: Solid State Physics, **11**(5):945–959, Mar. 1978.

Aken, B. B. v., Meetsma, A., and Palstra, T. T. M. Hexagonal YMnO3. Acta Crystallographica Section C Crystal Structure Communications, **57**(3):230–232, Mar. 2001.

Akimov, I. A., Belotelov, V. I., Scherbakov, A. V., et al. Hybrid structures of magnetic semiconductors and plasmonic crystals: a novel concept for magneto-optical devices [invited]. Journal of the Optical Society of America B, **29**(2):A103–A118, Feb. 2012.

Antonelli, G. A., Maris, H. J., Malhotra, S. G., et al. Picosecond ultrasonics study of the vibrational modes of a nanostructure. Journal of Applied Physics, **91**(5):3261–3267, Mar. 2002.

Armelles, G., Cebollada, A., García-Martín, A., et al. Magnetoplasmonic nanostructures: systems supporting both plasmonic and magnetic properties. Journal of Optics A: Pure and Applied Optics, **11**(11):114023, Nov. 2009.

Armelles, G., Cebollada, A., García-Martín, A., et al. Magnetoplasmonics: Combining magnetic and plasmonic functionalities. Advanced Optical Materials, **1**(1):10–35, 2013.

Atwater, H. A. and Polman, A. Plasmonics for improved photovoltaic devices. Nature Materials, **9**(3):205–213, Mar. 2010.

Barnes, W. L., Dereux, A., and Ebbesen, T. W. Surface plasmon subwavelength optics. Nature, **424**(6950):824–830, Aug. 2003.

Beaurepaire, E., Merle, J.-C., Daunois, A., et al. Ultrafast spin dynamics in ferromagnetic nickel. Physical Review Letters, **76**(22):4250–4253, May 1996.

Belotelov, V. I. and Zvezdin, A. K. Magneto-optical properties of photonic crystals. Journal of the Optical Society of America B, **22**(1):286–292, Jan. 2005.

Belotelov, V. I., Doskolovich, L. L., and Zvezdin, A. K. Extraordinary magneto-optical effects and transmission through metal-dielectric plasmonic systems. Physical Review Letters, **98**(7):077401, Feb. 2007.

Belotelov, V. I., Bykov, D. A., Doskolovich, L. L., et al. Extraordinary transmission and giant magneto-optical transverse kerr effect in plasmonic nanostructured films. Journal of the Optical Society of America B, **26**(8):1594–1598, Aug. 2009.

Belotelov, V. I., Akimov, I. A., Pohl, M., et al. Enhanced magneto-optical effects in magnetoplasmonic crystals. Nature Nanotechnology, **6**(6):370–376, 2011.

Belotelov, V. I., Kalish, A. N., Zvezdin, A. K., et al. Fabry–Perot plasmonic structures for nanophotonics. Journal of the Optical Society of America B, **29**(3):294, Feb. 2012.

Blundell, S. Magnetism in condensed matter. Oxford University Press, Oxford, 2001.

Bonod, N., Reinisch, R., Popov, E., et al. Optimization of surface-plasmon-enhanced magneto-optical effects. Journal of the Optical Society of America B, **21**(4):791–797, Apr. 2004.

Bouhelier, A., Renger, J., Beversluis, M. R., et al. Plasmon-coupled tip-enhanced near-field optical microscopy. Journal of microscopy, **210**(Pt 3):220–224, June 2003. PMID: 12787088.

Boyd, R. W. Nonlinear optics. Academic Press, San Diego (California), 2008.

Brongersma, M. L. and Shalaev, V. M. The case for plasmonics. Science, **328**(5977): 440–441, Apr. 2010.

Brüggemann, C., Akimov, A. V., Glavin, B. A., et al. Modulation of a surface plasmon-polariton resonance by subterahertz diffracted coherent phonons. Physical Review B, **86**(12):121401, Sept. 2012a.

Brüggemann, C., Jäger, J., Glavin, B. A., et al. Studying periodic nanostructures by probing the in-sample optical far-field using coherent phonons. Applied Physics Letters, **101**(24):243117–243117–5, Dec. 2012b.

Buchin, É., Vaganova, E. I., Naumov, V. V., et al. Enhancement of the transversal magnetooptical kerr effect in nanoperforated cobalt films. Technical Physics Letters, **35**(7):589–593, July 2009.

Burke, J. J., Stegeman, G. I., and Tamir, T. Surface-polariton-like waves guided by thin, lossy metal films. Physical Review B, **33**(8):5186–5201, Apr. 1986.

Burstein, E., Pinczuk, A., and Mills, D. Inelastic light scattering by charge carrier excitations in two-dimensional plasmas: Theoretical considerations. Surface Science, **98**(1–3):451–468, Aug. 1980.

Chappert, C., Fert, A., and Van Dau, F. N. The emergence of spin electronics in data storage. Nature Materials, **6**(11):813–823, Nov. 2007.

Chen, G., Chen, H., Haurylau, M., et al. Predictions of CMOS compatible on-chip optical interconnect. In Proceedings of the 2005 international workshop on System level interconnect prediction, SLIP '05, page 13–20, New York, NY, USA, 2005. ACM.

Chen, H.-P., Wen, Y.-C., Chen, Y.-H., et al. Femtosecond laser-ultrasonic investigation of plasmonic fields on the metal/gallium nitride interface. Applied Physics Letters, **97**(20):201102, Nov. 2010.

Chin, J. Y., Steinle, T., Wehlus, T., et al. Nonreciprocal plasmonics enables giant enhancement of thin-film faraday rotation. Nature Communications, **4**:1599, Mar. 2013.

Choi, W. S., Kim, D. G., Seo, S. S. A., et al. Electronic structures of hexagonal RMnO_{3} (R=Gd, tb, dy, and ho) thin films: Optical spectroscopy and first-principles calculations. Physical Review B, **77**(4):045137, Jan. 2008a.

Choi, W. S., Moon, S. J., Seo, S. S. A., et al. Optical spectroscopic investigation on the coupling of electronic and magnetic structure in multiferroic hexagonal RMnO_{3} (R=Gd, tb, dy, and ho) thin films. Physical Review B, **78**(5):054440, Aug. 2008b.

Christensen, N. E. and Seraphin, B. O. Relativistic band calculation and the optical properties of gold. Physical Review B, **4**(10):3321–3344, Nov. 1971.

Clavero, C., Yang, K., Skuza, J. R., et al. Magnetic-field modulation of surface plasmon polaritons on gratings. Optics Letters, **35**(10):1557–1559, May 2010.

Cohen-Tannoudji, C. Quantenmechanik 1. 1. De Gruyter, Berlin [u.a.], 1999.

Ctistis, G., Papaioannou, E., Patoka, P., et al. Optical and magnetic properties of hexagonal arrays of subwavelength holes in optically thin cobalt films. Nano Letters, **9**(1):1–6, Jan. 2009.

Decker, D. L. and Vanfleet, H. B. Melting and high-temperature electrical resistance of gold under pressure. Physical Review, **138**(1A):A129–A133, Apr. 1965.

Del Fatti, N., Bouffanais, R., Vallée, F., et al. Nonequilibrium electron interactions in metal films. Physical Review Letters, **81**(4):922–925, July 1998.

Del Fatti, N., Voisin, C., Achermann, M., et al. Nonequilibrium electron dynamics in noble metals. Physical Review B, **61**(24):16956–16966, June 2000.

Eerenstein, W., Mathur, N. D., and Scott, J. F. Multiferroic and magnetoelectric materials. Nature, **442**(7104):759–765, Aug. 2006.

Fano, U. Effects of configuration interaction on intensities and phase shifts. Physical Review, **124**(6):1866–1878, Dec. 1961.

Ferguson, P., Stafsudd, O., and Wallis, R. Surface magnetoplasma waves in nickel. Physica B+C, **86**:1403–1405, Jan. 1977.

Ferreiro Vila, E., Bendana Sueiro, X., Gonzalez-Diaz, J., et al. Surface plasmon resonance effects in the magneto-optical activity of ag #x2013;co #x2013;ag trilayers. IEEE Transactions on Magnetics, **44**(11):3303–3306, 2008.

Ferrio, K. B. and Steel, D. G. Raman quantum beats of interacting excitons. Physical Review Letters, **80**(4):786–789, Jan. 1998.

Fiebig, M. Revival of the magnetoelectric effect. Journal of Physics D: Applied Physics, **38**(8):R123, Apr. 2005.

Fiebig, M., Fröhlich, D., Kohn, K., et al. Determination of the magnetic symmetry of hexagonal manganites by second harmonic generation. Physical Review Letters, **84** (24):5620–5623, June 2000.

Fluegel, B., Mascarenhas, A., Snoke, D. W., et al. Plasmonic all-optical tunable wavelength shifter. Nature Photonics, **1**(12):701–703, Dec. 2007.

Foiles, C. L. 4.2 drude parameters of pure metals. In Hellwege, K.-H. and Olsen, J. L., editors, Electrical Resistivity, Thermoelectrical Power and Optical Properties, number 15b in Landolt-Börnstein - Group III Condensed Matter, pages 212–222. Springer Berlin Heidelberg, Jan. 1985.

Fröhlich, D., Leute, S., Pavlov, V. V., et al. Nonlinear optical spectroscopy of the two-order-parameter compound YMnO_{3}. Physical Review Letters, **81**(15):3239–3242, Oct. 1998.

Genet, C. and Ebbesen, T. W. Light in tiny holes. Nature, **445**(7123):39–46, Jan. 2007.

Genet, C., van Exter, M., and Woerdman, J. Fano-type interpretation of red shifts and red tails in hole array transmission spectra. Optics Communications, **225**(4–6): 331–336, Oct. 2003.

Gómez-Abal, R., Ney, O., Satitkovitchai, K., et al. All-optical subpicosecond magnetic switching in NiO(001). Physical Review Letters, **92**(22):227402, June 2004.

González-Díaz, J. B., García-Martín, A., Armelles, G., et al. Surface-magnetoplasmon nonreciprocity effects in noble-metal/ferromagnetic heterostructures. Physical Review B, **76**(15):153402, Oct. 2007.

Gridnev, V. N. Optical control of the coherent dynamics of excitons in a semiconductor quantum well. JETP Letters, **93**(3):161–165, Apr. 2011.

Grishin, A. M. and Khartsev, S. I. Highly luminescent garnets for magneto-optical photonic crystals. Applied Physics Letters, **95**(10):102503–102503–3, Sept. 2009.

Groeneveld, R. H. M., Sprik, R., and Lagendijk, A. Femtosecond spectroscopy of electron-electron and electron-phonon energy relaxation in ag and au. Physical Review B, **51**(17):11433–11445, May 1995.

Guyader, L. L., Kirilyuk, A., Rasing, T., et al. Coherent control of surface plasmon polariton mediated optical transmission. Journal of Physics D: Applied Physics, **41** (19):195102, Oct. 2008.

Hansen, P. and Krumme, J. P. Magnetic and magneto-optical properties of garnet films. Thin Solid Films, **114**(1–2):69–107, Apr. 1984.

Hansen, P., Enke, K., and Winkler, G. 1.2.1.1 general remarks. In Hellwege, K.-H. and Hellwege, A. M., editors, Part A: Garnets and Perovskites, number 12a in Landolt-Börnstein - Group III Condensed Matter, pages 53–54. Springer Berlin Heidelberg, Jan. 1978.

Hansteen, F., Kimel, A., Kirilyuk, A., et al. Femtosecond photomagnetic switching of spins in ferrimagnetic garnet films. Physical Review Letters, **95**(4):047402, July 2005.

Hansteen, F., Kimel, A., Kirilyuk, A., et al. Nonthermal ultrafast optical control of the magnetization in garnet films. Physical Review B, **73**(1):014421, Jan. 2006.

Hecht, E. and Zajac, A. Optics. Addison-Wesley Longman, Amsterdam, 4th ed. international ed. edition, Feb. 2003.

Hickernell, R. K. and Sarid, D. Long-range surface magnetoplasmons in thin nickel films. Optics Letters, **12**(8):570–572, Aug. 1987.

Hill, M. T., Marell, M., Leong, E. S. P., et al. Lasing in metal-insulator-metal subwavelength plasmonic waveguides. Optics Express, **17**(13):11107–11112, June 2009.

Hitz, C. B., Ewing, J. J., and Hecht, J. Introduction to laser technology. Wiley-IEEE Press, Hoboken, N.J., 2012.

Huber, D. L. 4.0.1 general remarks. In Hellwege, K.-H. and Hellwege, A. M., editors, Part A, number 4a in Landolt-Börnstein - Group III Condensed Matter, pages 315–317. Springer Berlin Heidelberg, Jan. 1970.

Imada, M., Fujimori, A., and Tokura, Y. Metal-insulator transitions. Reviews of Modern Physics, **70**(4):1039–1263, Oct. 1998.

Ingerly, D., Agrawal, A., Ascazubi, R., et al. Low-k interconnect stack with metal-insulator-metal capacitors for 22nm high volume manufacturing. In Interconnect Technology Conference (IITC), 2012 IEEE International, pages 1–3, 2012.

Inoue, M., Arai, K., Fujii, T., et al. One-dimensional magnetophotonic crystals. Journal of Applied Physics, **85**(8):5768–5770, Apr. 1999.

Inoue, M., Khanikaev, A., and Baryshev, A. Nano-magnetophotonics. In Liu, J. P., Fullerton, E., Gutfleisch, O., et al., editors, Nanoscale Magnetic Materials and Applications, pages 627–659. Springer US, Boston, MA, 2009.

Ishi, T., Fujikata, J., Makita, K., et al. Si nano-photodiode with a surface plasmon antenna. Japanese Journal of Applied Physics, **44**(12):L364–L366, 2005.

Jang, K.-J., Lee, H.-g., Lee, S., et al. Strong spin-lattice coupling in multiferroic hexagonal manganite YMnO3 probed by ultrafast optical spectroscopy. Applied Physics Letters, **97**(3):031914–031914–3, July 2010.

Joffre, M., Hulin, D., Migus, A., et al. Laser-induced exciton splitting. Physical Review Letters, **62**(1):74–77, Jan. 1989.

Johnson, P. B. and Christy, R. W. Optical constants of the noble metals. Physical Review B, **6**(12):4370–4379, Dec. 1972.

Ju, G., Chen, L., Nurmikko, A. V., et al. Coherent magnetization rotation induced by optical modulation in ferromagnetic/antiferromagnetic exchange-coupled bilayers. Physical Review B, **62**(2):1171–1177, July 2000.

Kahn, F. J., Pershan, P. S., and Remeika, J. P. Ultraviolet magneto-optical properties of single-crystal orthoferrites, garnets, and other ferric oxide compounds. Physical Review, **186**(3):891–918, Oct. 1969.

Kalashnikova, A. M. and Pisarev, R. V. Electronic structure of hexagonal rare-earth manganites RMnO3. Journal of Experimental and Theoretical Physics Letters, **78**(3): 143–147, Aug. 2003.

Kalish, A. N., Belotelov, V. I., and Zvezdin, A. K. Optical properties of toroidal media. In Proc. SPIE 6728, pages 67283D–67283D, June 2007.

Kamiya, T. Femtosecond technology: from basic research to application prospects [...] [...]. Springer, Berlin [u.a., 1999.

Kastner, M. A., Birgeneau, R. J., Shirane, G., et al. Magnetic, transport, and optical properties of monolayer copper oxides. Reviews of Modern Physics, **70**(3):897–928, July 1998.

Khanikaev, A. B., Mousavi, S. H., Shvets, G., et al. One-way extraordinary optical transmission and nonreciprocal spoof plasmons. Physical Review Letters, **105**(12): 126804, Sept. 2010.

Kim, S., Jin, J., Kim, Y.-J., et al. High-harmonic generation by resonant plasmon field enhancement. Nature, **453**(7196):757–760, June 2008.

Kimel, A. V., Bentivegna, F., Gridnev, V. N., et al. Room-temperature ultrafast carrier and spin dynamics in GaAs probed by the photoinduced magneto-optical kerr effect. Physical Review B, **63**(23):235201, May 2001a.

Kimel, A. V., Pisarev, R. V., Bentivegna, F., et al. Time-resolved nonlinear optical spectroscopy of mn^{3+} ions in rare-earth hexagonal manganites RMnO_{3} (R=Sc, y, er). Physical Review B, **64**(20):201103, Oct. 2001b.

Kimel, A. V., Kirilyuk, A., Usachev, P. A., et al. Ultrafast non-thermal control of magnetization by instantaneous photomagnetic pulses. Nature, **435**(7042):655–657, June 2005.

Kirilyuk, A., Kimel, A. V., and Rasing, T. Ultrafast optical manipulation of magnetic order. Reviews of Modern Physics, **82**(3):2731–2784, Sept. 2010.

Kittel, C. Introduction to Solid State Physics. Wiley, Nov. 2004.

Kneipp, K. Surface-enhanced raman scattering. Physics Today, **60**(11):40–46, 2007.

Kretschmann, E. and Raether, H. Radiative decay of nonradiative surface plasmons excited by light. Z. Naturforsch. A, **23**:2135, 1968.

Krinchik, G. S. and Artem'ev, V. A. Magneto-optical properties of ni, co, and fe in the ultraviolet visible and infrared parts of the spectrum. Soviet Journal of Experimental and Theoretical Physics, **26**:1080, June 1968.

Landau, L. D., Lifshits, E. M., and Pitaevskii, L. P. Electrodynamics of continuous media. Butterworth-Heinemann, Oxford [England], 1995.

Lee, S., Pirogov, A., Kang, M., et al. Giant magneto-elastic coupling in multiferroic hexagonal manganites. Nature, **451**(7180):805–808, Feb. 2008.

Li, L. Fourier modal method for crossed anisotropic gratings with arbitrary permittivity and permeability tensors. Journal of Optics A: Pure and Applied Optics, **5**(4):345, July 2003.

Linder, N. and Sham, L. Theory of the coherent spin dynamics in magnetic semiconductor quantum wells. Physica E: Low-dimensional Systems and Nanostructures, **2** (1–4):412–416, July 1998.

Ma, W., Zhang, X., and Takahashi, K. Electrical properties and reduced debye temperature of polycrystalline thin gold films. Journal of Physics D: Applied Physics, **43** (46):465301, Nov. 2010.

MacDonald, K. F., Sámson, Z. L., Stockman, M. I., et al. Ultrafast active plasmonics. Nature Photonics, **3**(1):55–58, Jan. 2009.

Madden, R. P. and Codling, K. New autoionizing atomic energy levels in he, ne, and ar. Physical Review Letters, **10**(12):516–518, June 1963.

Maier, S. A. Plasmonics: Fundamentals and Applications. Springer, 2007.

Mansuripur, M. The Physical Principles of Magneto-optical Recording. Cambridge University Press, 0002 edition, July 1998.

Marquier, F., Greffet, J., Collin, S., et al. Resonant transmission through a metallic film due to coupled modes. Optics Express, **13**(1):70–76, Jan. 2005.

Meier, F. and Zakharchenya, B. P. Optical Orientation. Elsevier, Nov. 1984.

Meier, T., Thomas, P., and Koch, S. W. Coherent Semiconductor Optics: From Basic Concepts to Nanostructure Applications. Springer, 2007.

Michl, J. and Thulstrup, E. W. Spectroscopy with Polarized Light: Solute Alignment by Photoselection, Liquid Crystal, Polymers, and Membranes Corrected Software Edition. Wiley, Oct. 1995.

Miroshnichenko, A. E., Flach, S., and Kivshar, Y. S. Fano resonances in nanoscale structures. Reviews of Modern Physics, **82**(3):2257–2298, Aug. 2010.

Moharam, M. G., Pommet, D. A., Grann, E. B., et al. Stable implementation of the rigorous coupled-wave analysis for surface-relief gratings: enhanced transmittance matrix approach. Journal of the Optical Society of America A, **12**(5):1077–1086, May 1995.

Moskvin, A. S. and Pisarev, R. V. Optical spectroscopy of charge transfer transitions in multiferroic manganites, ferrites, and related insulators. Low Temperature Physics, **36**(6):489–510, July 2010.

Nahata, A., Linke, R. A., Ishi, T., et al. Enhanced nonlinear optical conversion from a periodically nanostructured metal film. Optics Letters, **28**(6):423–425, Mar. 2003.

Newman, D. M., Wears, M. L., and Matelon, R. J. Plasmon transport phenomena on a continuous ferromagnetic surface. EPL (Europhysics Letters), **68**(5):692, Dec. 2004.

Newman, D. M., Wears, M. L., Matelon, R. J., et al. Magneto-optic behaviour in the presence of surface plasmons. Journal of Physics: Condensed Matter, **20**(34):345230, Aug. 2008.

Noginov, M. A., Zhu, G., Belgrave, A. M., et al. Demonstration of a spaser-based nanolaser. Nature, **460**(7259):1110–1112, Aug. 2009.

Okamoto, K., Niki, I., Shvartser, A., et al. Surface-plasmon-enhanced light emitters based on InGaN quantum wells. Nature Materials, **3**(9):601–605, Sept. 2004.

Olney, R. D. and Romagnoli, R. J. Optical effects of surface plasma waves with damping in metallic thin films. Applied Optics, **26**(11):2279–2282, June 1987.

Ordal, M. A., Long, L. L., Bell, R. J., et al. Optical properties of the metals al, co, cu, au, fe, pb, ni, pd, pt, ag, ti, and w in the infrared and far infrared. Applied Optics, **22**(7):1099–1119, Apr. 1983.

Otto, A. Excitation of nonradiative surface plasma waves in silver by the method of frustrated total reflection. Zeitschrift für Physik, **216**(4):398–410, Aug. 1968.

Oulton, R. F., Sorger, V. J., Zentgraf, T., et al. Plasmon lasers at deep subwavelength scale. Nature, **461**(7264):629–632, Oct. 2009.

Pacifici, D. Plasmonics: A shifting perspective. Nature Photonics, **1**(12):689–690, Dec. 2007.

Pershan, P. S. Nonlinear optical properties of solids: Energy considerations. Physical Review, **130**(3):919–929, May 1963.

Pershan, P. S. Magneto-Optical effects. Journal of Applied Physics, **38**(3):1482–1490, Mar. 1967.

Pitaevskii, L. P. and Lifshitz, E. M. Physical Kinetics. Butterworth-Heinemann, Nov. 1981.

Pohl, M., Belotelov, V. I., Akimov, I. A., et al. Plasmonic crystals for ultrafast nanophotonics: Optical switching of surface plasmon polaritons. Physical Review B, **85**(8): 081401, Feb. 2012.

Pohl, M., Kreilkamp, L. E., Belotelov, V. I., et al. Tuning of the transverse magneto-optical kerr effect in magneto-plasmonic crystals. New Journal of Physics, **15**(7): 075024, July 2013a.

Pohl, M., Pavlov, V. V., Akimov, I. A., et al. Ultrafast photoinduced linear and circular optical anisotropy in the multiferroic hexagonal manganite YMnO_{3}. Physical Review B, **88**(19):195112, Nov. 2013b.

Porto, J. A., García-Vidal, F. J., and Pendry, J. B. Transmission resonances on metallic gratings with very narrow slits. Physical Review Letters, **83**(14):2845–2848, Oct. 1999.

Raether, H. Surface plasmons on smooth and rough surfaces and on gratings. Springer, 1988.

Ramsay, A. J. A review of the coherent optical control of the exciton and spin states of semiconductor quantum dots. Semiconductor Science and Technology, **25**(10):103001, Oct. 2010.

Raschke, M. B. High-harmonic generation with plasmonics: feasible or unphysical? Annalen der Physik, **525**(3):A40–A42, 2013.

Riedel, E. and Janiak, C. Anorganische Chemie. De Gruyter, Berlin; New York, 2011.

Ritchie, R. H., Arakawa, E. T., Cowan, J. J., et al. Surface-plasmon resonance effect in grating diffraction. Physical Review Letters, **21**(22):1530–1533, Nov. 1968.

Rosei, R. Temperature modulation of the optical transitions involving the fermi surface in ag: Theory. Physical Review B, **10**(2):474–483, July 1974.

Rotenberg, N., Caspers, J. N., and van Driel, H. M. Tunable ultrafast control of plasmonic coupling to gold films. Physical Review B, **80**(24):245420, Dec. 2009.

Sachdev, S. Colloquium: Order and quantum phase transitions in the cuprate superconductors. Reviews of Modern Physics, **75**(3):913–932, July 2003.

Salamon, M. B. and Jaime, M. The physics of manganites: Structure and transport. Reviews of Modern Physics, **73**(3):583–628, Aug. 2001.

Saleh, B. E. A. and Teich, M. C. Fundamentals of Photonics. Wiley, Mar. 2007.

Sarychev, A. K. and Shalaev, V. M. Electrodynamics of Metamaterials. World Scientific, Jan. 2007.

Schuller, J. A., Barnard, E. S., Cai, W., et al. Plasmonics for extreme light concentration and manipulation. Nature Materials, **9**(3):193–204, Mar. 2010.

Scott, J. F. and Araujo, C. A. P. d. Ferroelectric memories. Science, **246**(4936):1400–1405, Dec. 1989. PMID: 17755995.

Shih, H. C., Lin, T. H., Luo, C. W., et al. Magnetization dynamics and the mnˆ{3+} d-d excitation of hexagonal HoMnO_{3} single crystals using wavelength-tunable time-resolved femtosecond spectroscopy. Physical Review B, **80**(2):024427, July 2009.

Sibbett, W., Lagatsky, A. A., and Brown, C. T. A. The development and application of femtosecond laser systems. Optics Express, **20**(7):6989–7001, Mar. 2012.

Smith, N. V. Photoelectron energy spectra and the band structures of the noble metals. Physical Review B, **3**(6):1862–1878, Mar. 1971.

Smolenskiĭ, G. A. and Chupis, I. E. Ferroelectromagnets. Soviet Physics Uspekhi, **25** (7):475, July 1982.

Sommerfeld, A. Ueber die fortpflanzung elektrodynamischer wellen längs eines drahtes. Annalen der Physik, **303**(2):233–290, 1899.

Strelniker, Y. M. and Bergman, D. J. Transmittance and transparency of subwavelength-perforated conducting films in the presence of a magnetic field. Physical Review B, **77**(20):205113, May 2008.

Sun, C.-K., Vallée, F., Acioli, L. H., et al. Femtosecond-tunable measurement of electron thermalization in gold. Physical Review B, **50**(20):15337–15348, Nov. 1994.

Takahashi, A., Gomi, H., and Aihara, M. Ultrafast four-wave mixing in strongly correlated electron systems. Physical Review B, **69**(7):075116, Feb. 2004.

Temnov, V. V. Ultrafast acousto-magneto-plasmonics. Nature Photonics, **6**(11):728–736, 2012.

Temnov, V. V., Armelles, G., Woggon, U., et al. Active magneto-plasmonics in hybrid metal–ferromagnet structures. Nature Photonics, **4**(2):107–111, 2010.

Tinkham, M. Group theory and quantum mechanics. Dover Publications, Mineola, N.Y., 2003.

van Kampen, M., Jozsa, C., Kohlhepp, J. T., et al. All-optical probe of coherent spin waves. Physical Review Letters, **88**(22):227201, May 2002.

Wada, O. Femtosecond all-optical devices for ultrafast communication and signal processing. New Journal of Physics, **6**:183–183, Nov. 2004.

Wang, Y. T., Luo, C. W., and Kobayashi, T. Understanding multiferroic hexagonal manganites by static and ultrafast optical spectroscopy. Advances in Condensed Matter Physics, **2013**, Apr. 2013.

Wood, R. W. On a remarkable case of uneven distribution of light in a diffraction grating spectrum. Proceedings of the Physical Society of London, **18**(1):269, June 1902.

Wurtz, G. A., Hendren, W., Pollard, R., et al. Controlling optical transmission through magneto-plasmonic crystals with an external magnetic field. New Journal of Physics, **10**(10):105012, Oct. 2008.

Xu, B., Gunn, J. M., Cruz, J. M. D., et al. Quantitative investigation of the multiphoton intrapulse interference phase scan method for simultaneous phase measurement and compensation of femtosecond laser pulses. Journal of the Optical Society of America B, **23**(4):750–759, Apr. 2006.

Zhang, G. P. Origin of giant optical nonlinearity in charge-Transfer–Mott insulators: A new paradigm for nonlinear optics. Physical Review Letters, **86**(10):2086–2089, Mar. 2001.

Zhang, Y., Nie, Z., and Xiao, M. Coherent control of four-wave mixing. Higher Education Press ; Springer, Beijing; Berlin; New York, 2011.

Zhang, Z., Ahn, P., Dong, B., et al. Quantitative imaging of rapidly decaying evanescent fields using plasmonic near-field scanning optical microscopy. Scientific Reports, **3**, Sept. 2013.

Zhu, J. and Cui, Y. Photovoltaics: More solar cells for less. Nature Materials, **9**(3): 183–184, Mar. 2010.

Zia, R., Schuller, J. A., Chandran, A., et al. Plasmonics: the next chip-scale technology. Materials Today, **9**(7–8):20–27, July 2006.

Žutić, I., Fabian, J., and Das Sarma, S. Spintronics: Fundamentals and applications. Reviews of Modern Physics, **76**(2):323–410, Apr. 2004.

Zvezdin, A. K. and Kotov, V. A. Modern Magnetooptics and Magnetooptical Materials. Taylor & Francis, 1 edition, Jan. 1997.

List of Figures

List of Tables

List of Publications

1. "*Enhanced magneto-optical effects in magnetoplasmonic crystals*",
   Belotelov, V. I., Akimov, I. A., **Pohl, M.**, et al. Nature Nanotechnology, **6**(6):370-376, 2011

2. "*Plasmonic crystals for ultrafast nanophotonics: Optical switching of surface plasmon polaritons*",
   Pohl, M., Belotelov, V. I., Akimov, I. A., et al. Physical Review B, **85**(8):081401(R), 2012

3. "*Hybrid structures of magnetic semiconductors and plasmonic crystals: A novel concept for magneto-optical devices*",
   Akimov, I. A., Belotelov, V. I., Scherbakov, A. V., **Pohl, M.**, et al. J. Opt. Soc. Am. B, **29**(2):A103-A118, 2012

4. "*Tuning of the transverse magneto-optical Kerr effect in magneto-plasmonic crystals*",
   Pohl, M., Kreilkamp, L. E., Belotelov, V. I., et al. New Journal of Physics, **15**(7):075024, 2013

5. "*Ultrafast photoinduced linear and circular optical anisotropy in the multiferroic hexagonal manganite* $YMnO_3$",
   Pohl, M., Pavlov, V. V., Akimov, I. A., et al. Physical Review B, **88**(19):195112, 2013

Acknowledgments

Finally I would like to thank all the people who helped me on my way and contributed to this work with their support. Special thanks go to:

Prof. Dr. Manfred Bayer for providing me with the opportunity and the equipment to accomplish my research and for establishing an enjoyable atmosphere at this chair.

Dr. Ilya Akimov for the excellent support throughout my work and the countless discussions and brainstorming, which often gave me new ideas, crucial hints or at least taught me how much I still needed to read about.

Dr. Vladimir Belotelov for his theoretical support and for introducing me into the physics of surface plasmon polaritons during my first steps in the lab, which turned out to be not only interesting but also successful.

All of my colleagues at E2 for always falling on sympathetic ears with challenging physical issues (there are no problems, only challenges...), their unconditional willingness to help and for new points-of-view when I once again missed the forest for the trees.

Lars Kreilkamp for an inexhaustible pool of questions, which often pointed me to problems or solutions and always tested me on whether I had understood something entirely myself.

Lukas Langer for many desk-to-desk discussions, an enjoyable office atmosphere and for his talent to find useful things in the depths of the world-wide-web.

Michaela Wäscher for organizing so many parties and events and for silently managing us all from out of her office.

Klaus Wiegers and **Lars Wieschollek** for competent advice in matters of threads, seals and building holders of all sorts and for letting me use their precious tools (which I have always put back to their place. Honestly!).

My colleagues from E2b for their all-time good spirit and humor they spread in our corridor, for good company and amusing lunch times and coffee-breaks.